Engineering Analysis with Boundary Elements 180 (2025) 106480

Contents lists available at ScienceDirect

Engineering Analysis with Boundary Elements

journal homepage: www.elsevier.com/locate/enganabound

Higher-order weak formulation for vibration analysis of anisotropic doubly-curved shells with holes and discontinuities

Francesco Tornabene [*], Matteo Viscoti, Rossana Dimitri

Department of Innovation Engineering, School of Engineering, University of Salento, 73100, Lecce, Italy

ARTICLE INFO

Keywords:
Anisotropic materials
Bi-connected domains
Doubly-curved shells
Equivalent single layer
Finite elements
Generalized differential quadrature
Higher-order theories
Holes and discontinuities
Isogeometric mapping

ABSTRACT

This work focuses on the application of two-dimensional higher-order theories within the Equivalent Single Layer (ESL) approach for the free vibration analysis of anisotropic doubly-curved shells with irregular bi-connected domains, holes, and cracks. To this end, the dynamic governing equations are derived from the Hamilton principle in curvilinear principal coordinates, using a higher-order Lagrange interpolation of the unknown variables. An isogeometric mapping technique is employed to account for arbitrarily-shaped structures. A constitutive relation valid for generally anisotropic materials is considered within the theory, and a generalized kinematic model, based on power and zigzag functions, is adopted along the thickness direction. A numerical solution is derived with the Generalized Differential Quadrature (GDQ) method. Furthermore, a finite element implementation of the theory is carried out using higher-order Lagrange and Hermite shape functions to interpolate the solution within rectangular and triangular elements which discretize the parametric domain.

The model is validated against some reference solutions obtained from finite elements, and the convergence of the results from numerical method is assessed. The accuracy of the solution is investigated for structures described by bi-connected domains, including panels with one or more holes of arbitrary shape. Furthermore, doubly-curved laminated shells are studied with internal line cracks. The procedure presented in this paper represents a significative advancement in the analysis of shell structures, since it provides a comprehensive finite element formulation for anisotropic doubly-curved shells, based on unified formulations, which can be used even for curved laminated structures characterized by holes, discontinuities, cracks, and arbitrary shape.

1. Introduction

Recent applications in many engineering fields increasingly adopts structural elements with highly complex geometry, very frequently composed of advanced innovative materials [1–3]. In this context, new theoretical formulations are required to accurately predict the mechanical response of these structures [4,5], enabling their integration into efficient and sustainable design processes. However, these models must also be computationally efficient since the complexity of materials, geometry, loads, and boundary conditions can lead to a high computational demand. Indeed, analytical solutions are available only for structural problems with specific geometrical, loading, and material configurations [6,7]. For these reasons, advanced numerical techniques have been developed in literature to reduce the number of unknown variables involved in the simulations [8,9]. When classical numerical strategies are applied to advanced structural components, several issues emerge. Conventional methods fail to consider the actual geometry of the structure, because these methods are based on a local approximation using linear or at least quadratic elements of the geometrical shape. To overcome this limitation, a finer discretization of the geometric domain is required, which increases the computational cost. This approach is characteristic of the Finite Element Method (FEM), which is the most widely used numerical method in practical engineering design [10–14]. According to FEM, the physical domain is discretized into finite elements [15–18], and the unknown variables are locally interpolated using quantities associated with the nodes of the discretization. Depending on the properties of the interpolating functions, commonly named as shape functions, these quantities can represent the values of the unknown function, or their partial derivatives [19–21]. The most frequently used interpolation functions are based on Lagrange or Hermite polynomials, among others. A fundamental preliminary step in FEM-based analysis is the discretization of the physical domain, which can result in either structured or unstructured meshes. More specifically, in structured meshes each node is arranged in a regular grid, while in

---

[*] Corresponding author.
E-mail address: francesco.tornabene@unisalento.it (F. Tornabene).

https://doi.org/10.1016/j.enganabound.2025.106480
Received 3 August 2025; Received in revised form 31 August 2025; Accepted 16 September 2025

unstructured meshes the computational grid does not follow a regular pattern. Numerical models based on FEM can achieve high accuracy of the results. However, to correctly predict the response of the structure under consideration by using FEM-based approaches, the number of the unknown variables, known as Degrees of Freedom (DOFs), can be significantly large, especially for very complex structures. In contrast, isogeometric formulations [22,23] directly adopt the same functions used in Computer Aided Design (CAD) tools to describe both the geometry and the unknown variables. In this way, the computational cost can be significantly reduced while maintaining a high solution accuracy. When the isogeometric analysis is used, it is very common to use Non-Uniform-Rational-Basis-Spline (NURBS) curves, typical of CAD tools, to approximate the unknown variables [24–26].

When dealing with complex structural models, analytical solutions are not usually available, except for some specific geometric, loading, and material configurations. As a result, numerical techniques are used to derive approximate solutions. The FEM is a widely used methodology for discretizing structural problems and deriving numerical solutions. However, it does not ensure a-priori the higher-order continuity of derivatives of the solution at the interfaces between adjacent elements. Only the continuity of the solution itself is guaranteed. In the case of Hermite polynomials, some continuity conditions can be established between adjacent finite elements. To overcome these limitations, collocation numerical techniques have been introduced in literature [27,28]. These methods are based on the interpolation of the unknown variables across the entire computational domain. Among these methodologies, the Generalized Differential Quadrature (GDQ) [29–33] has extensively been applied to various engineering problems, including static analysis [34–36], vibrational analysis [37–39], fracture mechanics [40,41], time history analysis [42–44], multifield problems [45–47], and fluid analysis [48–50], among others. The GDQ method approximates the derivatives of a function within a differential equation [51]. Since it is based on a global interpolation of the function, it requires very few discrete points to achieve highly accurate results [52]. For this reason, it is computationally more efficient than classical numerical techniques. In addition, from the GDQ discretization of first-order derivatives, it is possible to compute numerically the integral of a given function, leading to the Generalized Integral Quadrature (GIQ) method [53,54]. Both GIQ and GDQ deliver excellent results with fewer grid points, especially when the computational grid is non-uniformly distributed.

Another important aspect that should be considered for efficient simulations is the assessment of the theoretical model used. Moving from the three-dimensional (3D) analysis, in case of thick or moderately thick panels, it is possible to develop two-dimensional (2D) models, because these structures are characterized by one geometric dimension smaller than the others. All 2D theories rely on an arbitrary kinematic model which describes the variation of the unknown variables along the thickness direction. For example, classical approaches like Classical Plate Theory (CPT), First-order Shear Deformation Theory (FSDT), and Third-order Shear Deformation Theory [55–57] assume a linear through-the-thickness distribution of in-plane displacement field components, while the out-of-plane deflection is considered uniform. These classical formulations belong to a broader class of structural theories known as Equivalent Single Layer (ESL) theories [58–60]. They are based on an arbitrary expansion of the unknown variables along the thickness of the laminated panel. In this way, the governing equations are derived only within the reference 2D surface, usually located at the mid thickness of the structure [61]. When dealing with ESL formulations for laminates, a special attention must be paid to describe the displacement field components at each interface as experimental tests show unconventional deflections of the structure in these regions, even including possible zigzag and sliding effects. To achieve better numerical predictions and to accurately model these phenomena, Layer-Wise (LW) formulations have been introduced in literature [62–64], which account for arbitrary kinematic expansions within each lamina of the structure. Kinematic compatibility conditions are then introduced to assemble the fundamental relations valid for the entire laminate [65]. It should be noted that in ESL theories, the number of DOFs is independent of the number of layers, whereas in LW approaches the number of laminae affects the size of the unknown vector. In addition to ESL and LW theories, the Equivalent Layer-Wise (ELW) approach combines thickness functions typical of LW within an ESL framework [66,67]. In this way, it is possible to ensure the kinematic loading conditions at both external sides of laminates [68]. Various ESL and LW theories can be found in literature which use different types of thickness functions, including polynomials and trigonometric expansions [69–72]. Furthermore, for ESL formulations, zigzag functions can be used to model interlaminar deflections. The classical Murakami's function [73,74] is widely used to predict the interlaminar zigzag effect, and it has been adopted with classical and higher-order kinematic models, known as Higher-order Shear Deformation Theories (HSDTs), to enhance the accuracy of theoretical predictions. In addition, refined zigzag theories can be used for orthotropic lamination schemes [75–77]. The thickness functions in refined zigzag models depend directly on the shear moduli of the layers. An important theoretical strategy for the development of 2D refined theories is the unified formulation [78,79], which derives the governing equations of a problem regardless of the specific kinematic field assumed along the thickness direction. Indeed, this formulation uses generalized kinematic expansions of unknown variables based on thickness functions, which can be of arbitrary order. The unified formulation was first proposed in the works by Washizu and Reddy [80,81], and has been applied to various structural theories, including classical approaches like CPT, FSDT, and the TSDT [82–84]. Furthermore, it has been used to model the multifield response of laminated panels, thus demonstrating to be a valid approach for modelling the behaviour of smart structural components under thermal, hygrometric, electric, and magnetic loads [85–88].

An important consideration related to the derivation of the solution of differential equations is the definition of the parametric domain. In many 2D structural theories, the physical domain is often assumed to be rectangular [89,90], which simplify the discretization of the computational domain. However, in the case of bi-connected domains, such those ones associated with C-shaped and U-shaped panels [91–93], it is not possible to introduce a rectangular physical domain. As a result, many theories presented in the literature cannot be directly adopted for practical engineering applications that involve features like holes and cracks [94,95]. Cut-outs and holes are usually introduced into the structure for functional reasons, but they can significantly affect the structural response due to stress concentration phenomena [96]. For this reason, it is important to generalize 2D theories based on rectangular domains to deal with more complex problems of engineering interest.

Therefore, this paper presents an efficient ESL formulation, based on higher-order kinematic models, for the free vibration analysis of doubly-curved shell structures with generally anisotropic lamination schemes. The unknown displacement field variables are expanded using higher-order theories and unified formulation along the thickness direction. A higher-order Lagrange interpolation is, then, applied to interpolate the generalized displacement components in a 2D grid [97]. The geometric shape of the structure is described using differential geometry principles in curvilinear principal coordinates, and a generally anisotropic lamination scheme is considered. The fundamental relations are derived from the Hamilton principle in the weak form, and they are solved using the GDQ and GIQ methods. In addition, a finite element implementation of the theory is carried out using the COMSOL Multiphysics, based on the computation of the total energy of the system, along with appropriate Dirichlet boundary conditions [98]. This approach allows the theory to be applied to laminated structures, described with principal coordinates, including also those ones associated with bi-connected physical domains. The refined 2D FEM discretization enables the study of the mode frequencies of structures of arbitrary shape, including those ones characterized by holes and discontinuities. The HSDT-based finite element model adopts both Lagrange and Hermite interpolating polynomials for local interpolation of the solution within rectangular and triangular elements, thus setting different compatibility conditions among adjacent elements. The accuracy of the solution is verified through various numerical investigations, comparing the results to 3D FEM analyses obtained from commercial softwares. The results demonstrate that the refined 2D FEM model is a valid tool for determining the modal response of structures with various curvatures and lamination schemes. Furthermore, a possible enhancement of the theory can be the introduction of additional fields in the unknown variables. In this way, it would be possible to deal also with the forced and free vibrational response of shell structures characterized by smart piezoelectric layers within the lamination scheme [99,100].

2. Shell higher-order weak formulation

The geometric description of an arbitrary doubly-curved shell consists on defining the position vector $\mathbf{R}$ of an arbitrary point of the solid. This vector is univocally identified by three parameters α_1, α_2, α_3. Referring to a global Cartesian coordinate system $Ox_1x_2x_3$ with unit vectors $\mathbf{e}_1, \mathbf{e}_2, \mathbf{e}_3$, the following relation is adopted to describe the geometry of a 3D solid:

$$\mathbf{R}(\alpha_1,\alpha_2,\alpha_3) = f_1(\alpha_1,\alpha_2,\alpha_3)\mathbf{e}_1 + f_2(\alpha_1,\alpha_2,\alpha_3)\mathbf{e}_2 + f_3(\alpha_1,\alpha_2,\alpha_3)\mathbf{e}_3 \tag{1}$$

Here, f_1, f_2, f_3 are continuous smooth functions. In line with the ESL approach, the position vector $\mathbf{R}$ of the doubly-curved solid is defined though the introduction of a reference surface located in the mid thickness of the structure, whose position vector is denoted by $\mathbf{r}(\alpha_1,\alpha_2)$. In this way, the relation $\alpha_3 = \zeta$ is assumed, which means that the third parameter is the thickness coordinate of the shell solid. In this way, $\mathbf{R}$ takes the following expression, being h the total thickness of the shell [69]:

$$\mathbf{R}(\alpha_1,\alpha_2,\zeta) = \mathbf{r}(\alpha_1,\alpha_2) + \frac{h(\alpha_1,\alpha_2)}{2} z\mathbf{n}(\alpha_1,\alpha_2) \tag{2}$$

In Eq. (2), the quantity $z = 2\zeta/h(\alpha_1,\alpha_2)$ with $z \in [-1,1]$ is a dimensionless variable that identifies the points located along the thickness direction of the shell. Eq. (2) is defined within a rectangular physical domain, denoted as $[\alpha_1^0,\alpha_1^1] \times [\alpha_2^0,\alpha_2^1]$, where α_i^0, α_i^1 with $i = 1,2$ represent the locations of the four lateral surfaces of the shell solid. Starting from the position vector of the reference surface, the well-known Lamé parameters $A_1(\alpha_1,\alpha_2)$ and $A_2(\alpha_1,\alpha_2)$ are introduced within the physical domain, defined according to the relation reported below:

$$A_1 = \sqrt{\mathbf{r}_{,1}\cdot\mathbf{r}_{,1}}, \quad A_2 = \sqrt{\mathbf{r}_{,2}\cdot\mathbf{r}_{,2}} \tag{3}$$

In Eq. (3), $\mathbf{r}_{,i} = \partial\mathbf{r}/\partial\alpha_i$ with $i = 1,2$ denote the partial derivatives of the reference surface position vector $\mathbf{r}$ with respect to $\alpha_i = \alpha_1,\alpha_2$. For completeness, the quantities $\mathbf{r}_{,ij} = \partial^2\mathbf{r}/(\partial\alpha_i\partial\alpha_j)$ with $i,j = 1,2$ are the second-order partial derivatives of the reference surface $\mathbf{r}$ with respect to $\alpha_i,\alpha_j = \alpha_1,\alpha_2$. In this way, the principal curvature radii of the reference surface, denoted by R_1 and R_2, are evaluated at each point of the reference surface as follows:

$$R_1(\alpha_1,\alpha_2) = -\frac{\mathbf{r}_{,1}\cdot\mathbf{r}_{,1}}{\mathbf{r}_{,11}\cdot\mathbf{n}}, \quad R_2(\alpha_1,\alpha_2) = -\frac{\mathbf{r}_{,2}\cdot\mathbf{r}_{,2}}{\mathbf{r}_{,22}\cdot\mathbf{n}} \tag{4}$$

In Eq. (4), $\mathbf{n}$ denotes the outward unit vector of the reference surface. This vector is defined as:

$$\mathbf{n}(\alpha_1,\alpha_2) = \frac{\mathbf{r}_{,1}\times\mathbf{r}_{,2}}{|\mathbf{r}_{,1}\times\mathbf{r}_{,2}|} \tag{5}$$

In this way, the through-the-thickness scaling parameters $H_i = H_1, H_2$ are introduced for each point of the 3D solid:

$$H_i(\alpha_1,\alpha_2,\zeta) = 1 + \frac{\zeta}{R_i} \tag{6}$$

The thickness h of the doubly-curved laminated shell structure, introduced previously, is obtained as the sum of the individual thicknesses h_k with $k = 1,\dots,l$ of each k-th layer, where l is the total number of laminae:

$$h(\alpha_1,\alpha_2) = \sum_{k=1}^{l} h_k(\alpha_1,\alpha_2) = \sum_{k=1}^{l} (\zeta_{k+1}(\alpha_1,\alpha_2) - \zeta_k(\alpha_1,\alpha_2)) \tag{7}$$

As can be seen, the arbitrary k-th layer is located between the thickness coordinates ζ_k and ζ_{k+1}. All these geometric quantities, defined for a rectangular continuum-based physical domain, are thus evaluated on a 2D discrete grid of size $I_N \times I_M$. This grid is located within the rectangular interval $[\alpha_1^0,\alpha_1^1] \times [\alpha_2^0,\alpha_2^1]$. The coordinates α_{1f} and α_{2g} of the arbitrary point of the grid at issue are determined from the quantities r_f and r_g, defined for each $f = 1,\dots,I_N$ and $g = 1,\dots,I_M$, which are the roots of the Legendre polynomials [69], denoted by $LGL_{I_P+1}(\xi_r)$, evaluated for $I_P = I_N, I_M$ from the Lobatto and Legendre polynomials A_{I_P-1} and L_{I_P}, respectively:

$$LGL_{I_P+1}(\xi_r) = (1-\xi_r^2)A_{I_P-1}(\xi_r) = (1-\xi_r^2)\frac{d}{d\xi_r}(L_{I_P}(\xi_r)) \tag{8}$$

with $r = 1,2$ and $\xi_r \in [-1,1]$. The Legendre polynomials occurring in Eq. (8) are obtained using the following recursive expression:

$$L_{I_P}(\xi_r) = \frac{(2I_P-3)\xi_r L_{I_P-1}(\xi_r) - (I_P-2)L_{I_P-2}(\xi_r)}{I_P-1} \tag{9}$$

with $L_1(\xi_r) = 1$ and $L_2(\xi_r) = \xi_r$. Finally, the following transformations are used to determine the quantities r_f, r_g:

$$\begin{aligned} \alpha_{1f} &= \frac{\alpha_1^1-\alpha_1^0}{r_{I_N}-r_1}(r_f-r_1) + \alpha_1^0 \\ \alpha_{2g} &= \frac{\alpha_2^1-\alpha_2^0}{r_{I_M}-r_1}(r_g-r_1) + \alpha_2^0 \end{aligned} \tag{10}$$

In this model, a higher-order expansion of the displacement field components $U_1^{(k)}, U_2^{(k)}, U_3^{(k)}$ along the thickness direction is developed using the unified formulation. To this end, the matrix $\mathbf{F}_\tau^{(k)}$ is introduced, which contains the thickness functions $F_\tau^{(k)\alpha_1}, F_\tau^{(k)\alpha_2}, F_\tau^{(k)\alpha_3}$ associated with the τ-th order of the kinematic expansion [69], being $\tau = 0,\dots,N+1$. In this way, the displacement field vector $\mathbf{U}^{(k)}$ is expressed as follows:

$$\mathbf{U}^{(k)}(\alpha_1,\alpha_2,\zeta,t) = \sum_{\tau=0}^{N+1} \mathbf{F}_\tau^{(k)}(\zeta)\mathbf{u}^{(\tau)}(\alpha_1,\alpha_2,t) \tag{11}$$

The vector $\mathbf{u}^{(\tau)}$ is defined on the reference surface for each $\tau = 0,\dots,N+1$ and contains the generalized unknown variables of the formulation, which are the generalized displacement field components $u_1^{(\tau)}, u_2^{(\tau)}, u_3^{(\tau)}$ associated with any $\tau = 0,\dots,N+1$. Using an extended notation, the previous relation becomes [69]:

$$\begin{bmatrix} U_1^{(k)} \\ U_2^{(k)} \\ U_3^{(k)} \end{bmatrix} = \sum_{\tau=0}^{N+1} \begin{bmatrix} F_\tau^{(k)\alpha_1} & 0 & 0 \\ 0 & F_\tau^{(k)\alpha_2} & 0 \\ 0 & 0 & F_\tau^{(k)\alpha_3} \end{bmatrix} \begin{bmatrix} u_1^{(\tau)} \\ u_2^{(\tau)} \\ u_3^{(\tau)} \end{bmatrix} \tag{12}$$

In the present work, the following expressions are adopted for the set of thickness functions, based on power polynomials:

$$F_\tau^{(k)\alpha_i}(\zeta) = \begin{cases} \zeta^\tau & \tau = 0,\dots,N \\ (-1)^k z_k = (-1)^k \dfrac{2}{\zeta_{k+1}-\zeta_k}\zeta - \dfrac{\zeta_{k+1}+\zeta_k}{\zeta_{k+1}-\zeta_k} & \tau = N+1 \end{cases} \tag{13}$$

In particular, power functions are adopted for $\tau = 0,\dots,N$, while the thickness function associated with $\tau = N+1$ allows for the prediction of zigzag effects within the structure. To easily identify the kinematic model used in each simulation, the nomenclature $\mathrm{EDZ}-N$ is adopted, where N is the maximum kinematic expansion order. Furthermore, “E” stands for ESL formulation, while “D” is used to identify the displacement field components as the unknown variables in the formulation. Finally, “Z” is used only when the zigzag function is adopted into the kinematic model. The unknown variables of the theory, namely the generalized displacement field components $u_1^{(\tau)}, u_2^{(\tau)}, u_3^{(\tau)}$ for each $\tau = 0, \ldots, N+1$, are interpolated on the computational grid introduced in Eq. (10) using the 2D Lagrange polynomials [69]. To this end, for each quantity α_{1f} and α_{2g}, these polynomials are evaluated from the relations reported below:

$$l_f(\alpha_1) = \frac{\prod_{i=1}^{I_N}(\alpha_1 - \alpha_{1i})}{(\alpha_1 - \alpha_{1f}) \prod_{i=1,\ i\neq f}^{I_N} (\alpha_{1f} - \alpha_{1i})}, \quad l_g(\alpha_2) = \frac{\prod_{j=1}^{I_M}(\alpha_2 - \alpha_{2j})}{(\alpha_2 - \alpha_{2g}) \prod_{j=1,\ j\neq g}^{I_M} (\alpha_{2g} - \alpha_{2j})} \tag{14}$$

The polynomials $l_f(\alpha_1)$ and $l_g(\alpha_2)$ are then assembled into the vectors $\boldsymbol{l}_{\alpha_1}$ and $\boldsymbol{l}_{\alpha_2}$, respectively. These vectors, of size $1 \times I_N$ and $1 \times I_M$, take the following extended form:

$$\begin{aligned} \boldsymbol{l}_{\alpha_1} &= \left[l_1(\alpha_1) \ \ldots \ l_f(\alpha_1) \ \ldots \ l_{I_N}(\alpha_1) \right] \\ \boldsymbol{l}_{\alpha_2} &= \left[l_1(\alpha_2) \ \ldots \ l_g(\alpha_2) \ \ldots \ l_{I_M}(\alpha_2) \right] \end{aligned} \tag{15}$$

For the sake of completeness, the first-order derivatives of the interpolating polynomials with respect to α_1, α_2 are conveniently collected into the vectors $\boldsymbol{l}_{\alpha_1}^{(1)}$ and $\boldsymbol{l}_{\alpha_2}^{(1)}$ of size $1 \times I_N$ and $1 \times I_M$, respectively, introducing the positions $l_f^{(1)}(\alpha_1) = \partial l_f / \partial \alpha_1$ and $l_g^{(1)}(\alpha_2) = \partial l_g / \partial \alpha_2$ with $f = 1, \ldots, I_N$ and $g = 1, \ldots, I_M$:

$$\begin{aligned} \boldsymbol{l}_{\alpha_1}^{(1)} &= \left[l_1^{(1)}(\alpha_1) \ \ldots \ l_f^{(1)}(\alpha_1) \ \ldots \ l_{I_N}^{(1)}(\alpha_1) \right] \\ \boldsymbol{l}_{\alpha_2}^{(1)} &= \left[l_1^{(1)}(\alpha_2) \ \ldots \ l_g^{(1)}(\alpha_2) \ \ldots \ l_{I_M}^{(1)}(\alpha_2) \right] \end{aligned} \tag{16}$$

Starting from the definitions in Eq. (15), each element of the generalized displacement field vector $\mathbf{u}^{(\tau)}$ is expressed with a higher-order Lagrange interpolation, represented in condensed matrix notation as follows:

$$\mathbf{u}^{(\tau)} = \mathbf{N}^T \overline{\mathbf{u}}^{(\tau)} \tag{17}$$

where vector $\overline{\mathbf{u}}^{(\tau)}$ contains the values assumed by the elements of $\mathbf{u}^{(\tau)}$ on a discrete 2D grid of size $I_N \times I_M$, while the shape functions matrix $\mathbf{N}$ of size $3 \times (3 I_N I_M)$ is defined from the vectors $\boldsymbol{l}_{\alpha_1}$ and $\boldsymbol{l}_{\alpha_2}$, introduced in Eq. (15), through the Kronecker product operation, denoted by $\otimes$, in accordance with Ref. [69]:

$$\mathbf{N}^T = \begin{bmatrix} \overline{\mathbf{N}}^T & \mathbf{0} & \mathbf{0} \\ \mathbf{0} & \overline{\mathbf{N}}^T & \mathbf{0} \\ \mathbf{0} & \mathbf{0} & \overline{\mathbf{N}}^T \end{bmatrix} = \begin{bmatrix} \boldsymbol{l}_{\alpha_2} \otimes \boldsymbol{l}_{\alpha_1} & \mathbf{0} & \mathbf{0} \\ \mathbf{0} & \boldsymbol{l}_{\alpha_2} \otimes \boldsymbol{l}_{\alpha_1} & \mathbf{0} \\ \mathbf{0} & \mathbf{0} & \boldsymbol{l}_{\alpha_2} \otimes \boldsymbol{l}_{\alpha_1} \end{bmatrix} \tag{18}$$

In this way, the higher-order interpolation in Eq. (17) can be written in expanded form as follows:

$$\begin{bmatrix} u_1^{(\tau)}(\alpha_1, \alpha_2, t) \\ u_2^{(\tau)}(\alpha_1, \alpha_2, t) \\ u_3^{(\tau)}(\alpha_1, \alpha_2, t) \end{bmatrix} = \sum_{f=1}^{I_N} \sum_{g=1}^{I_M} \begin{bmatrix} l_f(\alpha_1) l_g(\alpha_2) & 0 & 0 \\ 0 & l_f(\alpha_1) l_g(\alpha_2) & 0 \\ 0 & 0 & l_f(\alpha_1) l_g(\alpha_2) \end{bmatrix} \begin{bmatrix} u_1^{(\tau)}(\alpha_{1f}, \alpha_{2g}, t) \\ u_2^{(\tau)}(\alpha_{1f}, \alpha_{2g}, t) \\ u_3^{(\tau)}(\alpha_{1f}, \alpha_{2g}, t) \end{bmatrix} \tag{19}$$

where $(\alpha_{1f}, \alpha_{2g})$ is the location of the arbitrary point of the 2D grid within the rectangular physical domain. Finally, the vector $\overline{\mathbf{u}}^{(\tau)}$ in Eq. (17) is conveniently arranged by introducing the matrices $\overline{\mathbf{u}}_i^{(\tau)} = \overline{\mathbf{u}}_1^{(\tau)}, \overline{\mathbf{u}}_2^{(\tau)}, \overline{\mathbf{u}}_3^{(\tau)}$, which collect the values $u_{i(fg)}^{(\tau)} = u_{1(fg)}^{(\tau)}, u_{2(fg)}^{(\tau)}, u_{3(fg)}^{(\tau)}$ of the generalized displacement field variables $u_i^{(\tau)} = u_1^{(\tau)}, u_2^{(\tau)}, u_3^{(\tau)}$ at the discrete points $(\alpha_{1f}, \alpha_{2g})$ belonging to the 2D discrete grid, setting $f = 1, \ldots, I_N$ and $g = 1, \ldots, I_M$. The following definition can be, thus, considered:

$$\overline{\mathbf{u}}^{(\tau)} = \begin{bmatrix} \overrightarrow{\mathbf{u}}_1^{(\tau)} \\ \overrightarrow{\mathbf{u}}_2^{(\tau)} \\ \overrightarrow{\mathbf{u}}_3^{(\tau)} \end{bmatrix} \tag{20}$$

In Eq. (20), the sub-vectors $\overrightarrow{\mathbf{u}}_i^{(\tau)} = \overrightarrow{\mathbf{u}}_1^{(\tau)}, \overrightarrow{\mathbf{u}}_2^{(\tau)}, \overrightarrow{\mathbf{u}}_3^{(\tau)}$ are defined from the matrices $\overline{\mathbf{u}}_i^{(\tau)} = \overline{\mathbf{u}}_1^{(\tau)}, \overline{\mathbf{u}}_2^{(\tau)}, \overline{\mathbf{u}}_3^{(\tau)}$ through the by-column vectorization operation. If $\mathbf{A}$ is a 2D matrix of size $I_N \times I_M$, whose arbitrary element is denoted by A_{ij} with $i = 1, \ldots, I_N$ and $j = 1, \ldots, I_M$, the vectorization operation defines a column vector $\overrightarrow{\mathbf{A}}$ of size $I_N I_M \times 1$, expressed as follows [69]:

$$\overrightarrow{\mathbf{A}} = \mathrm{Vec}(\mathbf{A}) \ \Leftrightarrow \ A_k = \left(A_{ij}\right)_k \tag{21}$$

where the index $k = 1, \ldots, I_N I_M$ is defined so that $k = i + (j-1) I_N$. Thus, vectors $\overrightarrow{\mathbf{u}}_i^{(\tau)} = \overrightarrow{\mathbf{u}}_1^{(\tau)}, \overrightarrow{\mathbf{u}}_2^{(\tau)}, \overrightarrow{\mathbf{u}}_3^{(\tau)}$ take the following aspect, being $u_{i(fg)}^{(\tau)} = u_{1(fg)}^{(\tau)}, u_{2(fg)}^{(\tau)}, u_{3(fg)}^{(\tau)}$ their corresponding arbitrary elements with $f = 1, \ldots, I_N$ and $g = 1, \ldots, I_M$:

$$\begin{aligned} \overrightarrow{\mathbf{u}}_i^{(\tau)} &= \mathrm{Vec}\left(\overline{\mathbf{u}}_i^{(\tau)}\right) \\ &= \left[u_{i\,(11)}^{(\tau)} \ \cdots \ u_{i\,(I_N 1)}^{(\tau)} \ \ u_{i\,(12)}^{(\tau)} \ \cdots \ u_{i\,(I_N 2)}^{(\tau)} \ \ u_{i\,(1 I_M)}^{(\tau)} \ \cdots \ u_{i\,(I_N I_M)}^{(\tau)} \right]^T \end{aligned} \tag{22}$$

for $i = 1, 2, 3$. At this point, the higher-order 2D interpolation provided in Eq. (17) is substituted into the generalized kinematic model expressed in Eq. (11), leading to the following relation:

$$\mathbf{U}^{(k)} = \sum_{\tau=0}^{N+1} \mathbf{F}_\tau^{(k)} \mathbf{u}^{(\tau)} = \sum_{\tau=0}^{N+1} \mathbf{F}_\tau^{(k)} \mathbf{N}^T \overline{\mathbf{u}}^{(\tau)} \tag{23}$$

The governing equations are derived from the Hamiltonian principle by assuming a stationary configuration of the total strain energy over an arbitrary time interval $[t_1, t_2]$. To this end, the following relation is considered:

$$\int_{t_1}^{t_2} (\delta\Phi - \delta T) dt = \int_{t_1}^{t_2} \delta\Phi \, dt - \int_{t_1}^{t_2} \delta T \, dt = 0 \tag{24}$$

The higher-order ESL definition equations are derived for a doubly-curved laminated shell structure employing curvilinear principal coordinates. To this end, the kinematic relations for a general doubly-curved 3D shell are recalled hereafter, where $\mathbf{D}$ denotes the 3D differential definition operator, as defined in Ref. [69]:

$$\boldsymbol{\varepsilon}^{(k)} = \mathbf{D}\,\mathbf{U}^{(k)} = \mathbf{D}_\zeta \left(\sum_{i=1}^{3} \mathbf{D}_\Omega^{\alpha_i} \right) \mathbf{U}^{(k)} \tag{25}$$

In Eq. (25), the displacement field vector $\mathbf{U}^{(k)}$ is transformed into the 3D strain vector $\boldsymbol{\varepsilon}^{(k)}(\alpha_1, \alpha_2, \zeta, t) = \left[\varepsilon_1^{(k)} \ \ \varepsilon_2^{(k)} \ \ \gamma_{12}^{(k)} \ \ \gamma_{13}^{(k)} \ \ \gamma_{23}^{(k)} \ \ \varepsilon_3^{(k)} \right]^T$. The differential operator $\mathbf{D}$ is conveniently expressed in terms of operators $\mathbf{D}_\zeta$ and $\mathbf{D}_\Omega^{\alpha_i} = \mathbf{D}_\Omega^{\alpha_1}, \mathbf{D}_\Omega^{\alpha_2}, \mathbf{D}_\Omega^{\alpha_3}$, which contain the terms of the kinematic relations defined in terms of the thickness variable ζ and those ones associated with the in-plane variables α_1, α_2, respectively. These operators are expressed in matrix form as follows:

$$\mathbf{D}_{\Omega}^{\alpha_1} = \begin{bmatrix} \frac{1}{A_1}\frac{\partial}{\partial \alpha_1} & 0 & 0 \\ \frac{1}{A_1A_2}\frac{\partial A_2}{\partial \alpha_1} & 0 & 0 \\ -\frac{1}{A_1A_2}\frac{\partial A_1}{\partial \alpha_2} & 0 & 0 \\ \frac{1}{A_2}\frac{\partial}{\partial \alpha_2} & 0 & 0 \\ -\frac{1}{R_1} & 0 & 0 \\ 0 & 0 & 0 \\ 1 & 0 & 0 \\ 0 & 0 & 0 \\ 0 & 0 & 0 \end{bmatrix}, \quad \mathbf{D}_{\Omega}^{\alpha_2} = \begin{bmatrix} 0 & \frac{1}{A_1A_2}\frac{\partial A_1}{\partial \alpha_2} & 0 \\ 0 & \frac{1}{A_2}\frac{\partial}{\partial \alpha_2} & 0 \\ 0 & \frac{1}{A_1}\frac{\partial}{\partial \alpha_1} & 0 \\ 0 & -\frac{1}{A_1A_2}\frac{\partial A_2}{\partial \alpha_1} & 0 \\ 0 & 0 & 0 \\ 0 & -\frac{1}{R_2} & 0 \\ 0 & 0 & 0 \\ 0 & 1 & 0 \\ 0 & 0 & 0 \end{bmatrix}, \quad \mathbf{D}_{\Omega}^{\alpha_3} = \begin{bmatrix} 0 & 0 & \frac{1}{R_1} \\ 0 & 0 & \frac{1}{R_2} \\ 0 & 0 & 0 \\ 0 & 0 & 0 \\ 0 & 0 & \frac{1}{A_1}\frac{\partial}{\partial \alpha_1} \\ 0 & 0 & \frac{1}{A_2}\frac{\partial}{\partial \alpha_2} \\ 0 & 0 & 0 \\ 0 & 0 & 0 \\ 0 & 0 & 1 \end{bmatrix} \tag{26}$$

$$\mathbf{D}_{\zeta} = \begin{bmatrix} \frac{1}{H_1} & 0 & 0 & 0 & 0 & 0 & 0 & 0 & 0 \\ 0 & \frac{1}{H_2} & 0 & 0 & 0 & 0 & 0 & 0 & 0 \\ 0 & 0 & \frac{1}{H_1} & \frac{1}{H_2} & 0 & 0 & 0 & 0 & 0 \\ 0 & 0 & 0 & 0 & \frac{1}{H_1} & 0 & \frac{\partial}{\partial \zeta} & 0 & 0 \\ 0 & 0 & 0 & 0 & 0 & \frac{1}{H_2} & 0 & \frac{\partial}{\partial \zeta} & 0 \\ 0 & 0 & 0 & 0 & 0 & 0 & 0 & 0 & \frac{\partial}{\partial \zeta} \end{bmatrix} \tag{27}$$

By introducing the higher-order expansion of displacement field components, as presented in Eq. (23), into the 3D definition Eq. (25), the following relation is obtained in matrix notation:

$$\boldsymbol{\varepsilon}^{(k)} = \sum_{\tau=0}^{N+1}\sum_{i=1}^{3} \mathbf{D}_{\zeta}\mathbf{D}_{\Omega}^{\alpha_i}\mathbf{F}^{(k\tau)}\mathbf{u}^{(\tau)} = \sum_{\tau=0}^{N+1}\sum_{i=1}^{3} \mathbf{Z}^{(k\tau)\alpha_i}\mathbf{D}_{\Omega}^{\alpha_i}\mathbf{u}^{(\tau)} = \sum_{\tau=0}^{N+1}\sum_{i=1}^{3} \mathbf{Z}^{(k\tau)\alpha_i}\boldsymbol{\varepsilon}^{(\tau)\alpha_i} \tag{28}$$

where the matrix $\mathbf{Z}^{(k\tau)\alpha_i} = \mathbf{D}_{\zeta}F^{(k\tau)\alpha_i}$ has been conveniently introduced. In this way, the 3D strain vector $\boldsymbol{\varepsilon}^{(k)}$ can be expanded in analogy with Eq. (23) by introducing the generalized strain vector $\boldsymbol{\varepsilon}^{(\tau)\alpha_i} = \begin{bmatrix} \varepsilon_1^{(\tau)\alpha_i} & \varepsilon_2^{(\tau)\alpha_i} & \gamma_1^{(\tau)\alpha_i} & \gamma_2^{(\tau)\alpha_i} & \gamma_{13}^{(\tau)\alpha_i} & \gamma_{23}^{(\tau)\alpha_i} & \omega_{13}^{(\tau)\alpha_i} & \omega_{23}^{(\tau)\alpha_i} & \varepsilon_3^{(\tau)\alpha_i} \end{bmatrix}^T$, defined for each $\tau = 0, ..., N+1$ and $i = 1,2,3$. This vector is then expressed from the interpolation of the DOFs values in the 2D discrete grid using the shape functions matrix from Eq. (18):

$$\boldsymbol{\varepsilon}^{(\tau)\alpha_i} = \mathbf{D}_{\Omega}^{\alpha_i}\mathbf{u}^{(\tau)} = \mathbf{D}_{\Omega}^{\alpha_i}\mathbf{N}^T\overline{\mathbf{u}}^{(\tau)} = \mathbf{B}^{\alpha_i}\overline{\mathbf{u}}^{(\tau)} \tag{29}$$

The matrices $\mathbf{B}^{\alpha_i} = \mathbf{B}^{\alpha_1}, \mathbf{B}^{\alpha_2}, \mathbf{B}^{\alpha_3}$ are defined as follows [69]:

$$\mathbf{B}^{\alpha_1} = \begin{bmatrix} \frac{1}{A_1}\boldsymbol{l}_{\alpha_2}\otimes\boldsymbol{l}_{\alpha_1}^{(1)} & \mathbf{0} & \mathbf{0} \\ \frac{1}{A_1A_2}\frac{\partial A_2}{\partial \alpha_1}\boldsymbol{l}_{\alpha_2}\otimes\boldsymbol{l}_{\alpha_1} & \mathbf{0} & \mathbf{0} \\ -\frac{1}{A_1A_2}\frac{\partial A_1}{\partial \alpha_2}\boldsymbol{l}_{\alpha_2}\otimes\boldsymbol{l}_{\alpha_1} & \mathbf{0} & \mathbf{0} \\ \frac{1}{A_2}\boldsymbol{l}_{\alpha_2}^{(1)}\otimes\boldsymbol{l}_{\alpha_1} & \mathbf{0} & \mathbf{0} \\ -\frac{1}{R_1}\boldsymbol{l}_{\alpha_2}\otimes\boldsymbol{l}_{\alpha_1} & \mathbf{0} & \mathbf{0} \\ \mathbf{0} & \mathbf{0} & \mathbf{0} \\ \boldsymbol{l}_{\alpha_2}\otimes\boldsymbol{l}_{\alpha_1} & \mathbf{0} & \mathbf{0} \\ \mathbf{0} & \mathbf{0} & \mathbf{0} \\ \mathbf{0} & \mathbf{0} & \mathbf{0} \end{bmatrix}, \quad \mathbf{B}^{\alpha_2} = \begin{bmatrix} \mathbf{0} & \frac{1}{A_1A_2}\frac{\partial A_1}{\partial \alpha_2}\boldsymbol{l}_{\alpha_2}\otimes\boldsymbol{l}_{\alpha_1} & \mathbf{0} \\ \mathbf{0} & \frac{1}{A_2}\boldsymbol{l}_{\alpha_2}^{(1)}\otimes\boldsymbol{l}_{\alpha_1} & \mathbf{0} \\ \mathbf{0} & \frac{1}{A_1}\boldsymbol{l}_{\alpha_2}\otimes\boldsymbol{l}_{\alpha_1}^{(1)} & \mathbf{0} \\ \mathbf{0} & -\frac{1}{A_1A_2}\frac{\partial A_2}{\partial \alpha_1}\boldsymbol{l}_{\alpha_2}\otimes\boldsymbol{l}_{\alpha_1} & \mathbf{0} \\ \mathbf{0} & \mathbf{0} & \mathbf{0} \\ \mathbf{0} & -\frac{1}{R_2}\boldsymbol{l}_{\alpha_2}\otimes\boldsymbol{l}_{\alpha_1} & \mathbf{0} \\ \mathbf{0} & \mathbf{0} & \mathbf{0} \\ \mathbf{0} & \boldsymbol{l}_{\alpha_2}\otimes\boldsymbol{l}_{\alpha_1} & \mathbf{0} \\ \mathbf{0} & \mathbf{0} & \mathbf{0} \end{bmatrix}, \quad \mathbf{B}^{\alpha_3} = \begin{bmatrix} \mathbf{0} & \mathbf{0} & \frac{1}{R_1}\boldsymbol{l}_{\alpha_2}\otimes\boldsymbol{l}_{\alpha_1} \\ \mathbf{0} & \mathbf{0} & \frac{1}{R_2}\boldsymbol{l}_{\alpha_2}\otimes\boldsymbol{l}_{\alpha_1} \\ \mathbf{0} & \mathbf{0} & \mathbf{0} \\ \mathbf{0} & \mathbf{0} & \mathbf{0} \\ \mathbf{0} & \mathbf{0} & \frac{1}{A_1}\boldsymbol{l}_{\alpha_2}\otimes\boldsymbol{l}_{\alpha_1}^{(1)} \\ \mathbf{0} & \mathbf{0} & \frac{1}{A_2}\boldsymbol{l}_{\alpha_2}^{(1)}\otimes\boldsymbol{l}_{\alpha_1} \\ \mathbf{0} & \mathbf{0} & \mathbf{0} \\ \mathbf{0} & \mathbf{0} & \mathbf{0} \\ \mathbf{0} & \mathbf{0} & \boldsymbol{l}_{\alpha_2}\otimes\boldsymbol{l}_{\alpha_1} \end{bmatrix} \tag{30}$$

The constitutive relationship at an arbitrary point of the doubly-curved 3D solid accounts for a linear elastic, generally anisotropic behaviour. More specifically, the constitutive relation reported below is established between the 3D strain and stress vectors $\boldsymbol{\varepsilon}^{(k)}(\alpha_1, \alpha_2, \zeta, t)$ and

$\boldsymbol{\sigma}^{(k)}(\alpha_1,\alpha_2,\zeta,t)$, where $\overline{E}_{ij}^{(k)}$ are the constitutive coefficients for $i,j=1,\dots,6$ [69]:

$$\boldsymbol{\sigma}^{(k)}=\overline{\mathbf{E}}^{(k)}\boldsymbol{\varepsilon}^{(k)}\quad\Leftrightarrow\quad\begin{bmatrix}\sigma_1^{(k)}\\\sigma_2^{(k)}\\\tau_{12}^{(k)}\\\tau_{13}^{(k)}\\\tau_{23}^{(k)}\\\sigma_3^{(k)}\end{bmatrix}=\begin{bmatrix}\overline{E}_{11}^{(k)}&\overline{E}_{12}^{(k)}&\overline{E}_{16}^{(k)}&\overline{E}_{14}^{(k)}&\overline{E}_{15}^{(k)}&\overline{E}_{13}^{(k)}\\\overline{E}_{12}^{(k)}&\overline{E}_{22}^{(k)}&\overline{E}_{26}^{(k)}&\overline{E}_{24}^{(k)}&\overline{E}_{25}^{(k)}&\overline{E}_{23}^{(k)}\\\overline{E}_{16}^{(k)}&\overline{E}_{26}^{(k)}&\overline{E}_{66}^{(k)}&\overline{E}_{46}^{(k)}&\overline{E}_{56}^{(k)}&\overline{E}_{36}^{(k)}\\\overline{E}_{14}^{(k)}&\overline{E}_{24}^{(k)}&\overline{E}_{46}^{(k)}&\overline{E}_{44}^{(k)}&\overline{E}_{45}^{(k)}&\overline{E}_{34}^{(k)}\\\overline{E}_{15}^{(k)}&\overline{E}_{25}^{(k)}&\overline{E}_{56}^{(k)}&\overline{E}_{45}^{(k)}&\overline{E}_{55}^{(k)}&\overline{E}_{35}^{(k)}\\\overline{E}_{13}^{(k)}&\overline{E}_{23}^{(k)}&\overline{E}_{36}^{(k)}&\overline{E}_{34}^{(k)}&\overline{E}_{35}^{(k)}&\overline{E}_{33}^{(k)}\end{bmatrix}\begin{bmatrix}\varepsilon_1^{(k)}\\\varepsilon_2^{(k)}\\\gamma_{12}^{(k)}\\\gamma_{13}^{(k)}\\\gamma_{23}^{(k)}\\\varepsilon_3^{(k)}\end{bmatrix}\tag{31}$$

for $k=1,\dots,l$. The previous relation is associated with the curvilinear geometric reference system $O'\alpha_1\alpha_2\zeta$. In the same way, the 3D constitutive equation can be expressed in the material reference system $O'\alpha_1^{(k)}\alpha_2^{(k)}\zeta^{(k)}$, as shown below:

$$\widehat{\sigma}^{(k)}=\mathbf{E}^{(k)}\widehat{\varepsilon}^{(k)}\quad\Leftrightarrow\quad\begin{bmatrix}\widehat{\sigma}_1^{(k)}\\\widehat{\sigma}_2^{(k)}\\\widehat{\tau}_{12}^{(k)}\\\widehat{\tau}_{13}^{(k)}\\\widehat{\tau}_{23}^{(k)}\\\widehat{\sigma}_3^{(k)}\end{bmatrix}=\begin{bmatrix}E_{11}^{(k)}&E_{12}^{(k)}&E_{16}^{(k)}&E_{14}^{(k)}&E_{15}^{(k)}&E_{13}^{(k)}\\E_{12}^{(k)}&E_{22}^{(k)}&E_{26}^{(k)}&E_{24}^{(k)}&E_{25}^{(k)}&E_{23}^{(k)}\\E_{16}^{(k)}&E_{26}^{(k)}&E_{66}^{(k)}&E_{46}^{(k)}&E_{56}^{(k)}&E_{36}^{(k)}\\E_{14}^{(k)}&E_{24}^{(k)}&E_{46}^{(k)}&E_{44}^{(k)}&E_{45}^{(k)}&E_{34}^{(k)}\\E_{15}^{(k)}&E_{25}^{(k)}&E_{56}^{(k)}&E_{45}^{(k)}&E_{55}^{(k)}&E_{35}^{(k)}\\E_{13}^{(k)}&E_{23}^{(k)}&E_{36}^{(k)}&E_{34}^{(k)}&E_{35}^{(k)}&E_{33}^{(k)}\end{bmatrix}\begin{bmatrix}\widehat{\varepsilon}_1^{(k)}\\\widehat{\varepsilon}_2^{(k)}\\\widehat{\gamma}_{12}^{(k)}\\\widehat{\gamma}_{13}^{(k)}\\\widehat{\gamma}_{23}^{(k)}\\\widehat{\varepsilon}_3^{(k)}\end{bmatrix}\tag{32}$$

being $E_{ij}^{(k)}$ the constitutive coefficient of the material in the k-th layer, while $\widehat{\varepsilon}^{(k)}(\alpha_1,\alpha_2,\zeta,t)$ and $\widehat{\sigma}^{(k)}(\alpha_1,\alpha_2,\zeta,t)$ are the 3D strain and stress vectors in the material reference system, respectively. The material reference system can be rotated with respect to the geometric reference system to account for an arbitrary orientation of a layer in the lamination scheme. To this end, the transformation matrix $\mathbf{T}^{(k)}$ is defined, and the 3D constitutive matrix $\mathbf{E}^{(k)}$ is rotated into the geometric reference system 3D constitutive matrix $\overline{\mathbf{E}}^{(k)}$ as follows:

$$\overline{\mathbf{E}}^{(k)}=\mathbf{T}^{(k)}\mathbf{E}^{(k)}\left(\mathbf{T}^{(k)}\right)^T\tag{33}$$

If the material axis along the thickness direction corresponds to the geometric axis, namely $\zeta^{(k)}\equiv\zeta$, the rotation matrix $\mathbf{T}^{(k)}$ can be expressed in terms of the angle, $\vartheta^{(k)}$, between $\alpha_1^{(k)}$ and α_1 axes, measured clockwise. This matrix is derived from the rotation matrix $\mathbf{H}^{(k)}$, which is defined as follows:

$$\mathbf{H}^{(k)}=\begin{bmatrix}\cos\vartheta^{(k)}&\sin\vartheta^{(k)}&0\\-\sin\vartheta^{(k)}&\cos\vartheta^{(k)}&0\\0&0&1\end{bmatrix}\tag{34}$$

Based on the definition of Eq. (34), it gives [69]:

$$\begin{aligned}\mathbf{T}^{(k)}&=\overline{\mathbf{T}}^{(k)}_{([1,5,4,7,8,9]\times[1,5,2+4,3+7,6+8,9])}\\&=\left(\mathbf{H}^{(k)T}\otimes\left(\mathbf{H}^{(k)}\right)^{-1}\right)_{([1,5,4,7,8,9]\times[1,5,2+4,3+7,6+8,9])}\end{aligned}\tag{35}$$

where $\otimes$ denotes the Kronecker product. According to Eq. (35), the elements of the matrix $\mathbf{T}^{(k)}$ are obtained by selecting the rows and columns specified within the square brackets from matrix $\overline{\mathbf{T}}^{(k)}$. In addition, the third, the fourth, and the fifth columns of $\mathbf{T}^{(k)}$ are obtained from the sum of the corresponding elements in the appropriate columns of matrix $\overline{\mathbf{T}}^{(k)}$. Finally, the elements of the matrix $\mathbf{E}^{(k)}$ correspond to the 3D constitutive elastic stiffness constants of the material, namely $E_{ij}^{(k)}=C_{ij}^{(k)}$, or to the reduced elastic stiffness coefficients $E_{ij}^{(k)}=Q_{ij}^{(k)}$, depending on the selected kinematic model in Eq. (11). The components of the 3D stress vector $\boldsymbol{\sigma}^{(k)}$ are now used to compute the virtual variation $\delta\Phi$ of the elastic strain energy within the doubly-curved solid:

$$\delta\Phi=\sum_{k=1}^{l}\int_{\alpha_1}\int_{\alpha_2}\int_{\zeta_k}^{\zeta_{k+1}}\left(\delta\boldsymbol{\varepsilon}^{(k)T}\boldsymbol{\sigma}^{(k)}\right)A_1A_2H_1H_2d\alpha_1d\alpha_2d\zeta\tag{36}$$

Introducing the higher-order kinematic model from Eq. (23) through the kinematic relations in Eqs. (28) and (29), Eq. (36) can be expressed as follows [69]:

$$\begin{aligned}\delta\Phi&=\sum_{k=1}^{l}\int_{\alpha_1}\int_{\alpha_2}\int_{\zeta_k}^{\zeta_{k+1}}\left(\sum_{\tau=0}^{N+1}\sum_{i=1}^{3}\mathbf{Z}^{(k\tau)\alpha_i}\delta\boldsymbol{\varepsilon}^{(\tau)\alpha_i}\right)^T\boldsymbol{\sigma}^{(k)}A_1H_1A_2H_2d\zeta d\alpha_1d\alpha_2=\\&=\sum_{k=1}^{l}\int_{\alpha_1}\int_{\alpha_2}\int_{\zeta_k}^{\zeta_{k+1}}\left(\sum_{\tau=0}^{N+1}\sum_{i=1}^{3}\left(\delta\boldsymbol{\varepsilon}^{(\tau)\alpha_i}\right)^T\left(\mathbf{Z}^{(k\tau)\alpha_i}\right)^T\right)\boldsymbol{\sigma}^{(k)}A_1H_1A_2H_2d\zeta d\alpha_1d\alpha_2=\\&=\sum_{\tau=0}^{N+1}\sum_{i=1}^{3}\int_{\alpha_1}\int_{\alpha_2}\left(\delta\boldsymbol{\varepsilon}^{(\tau)\alpha_i}\right)^T\sum_{k=1}^{l}\int_{\zeta_k}^{\zeta_{k+1}}\left(\mathbf{Z}^{(k\tau)\alpha_i}\right)^T\boldsymbol{\sigma}^{(k)}H_1H_2d\zeta A_1A_2d\alpha_1d\alpha_2=\\&=\sum_{\tau=0}^{N+1}\sum_{i=1}^{3}\int_{\alpha_1}\int_{\alpha_2}\left(\delta\boldsymbol{\varepsilon}^{(\tau)\alpha_i}\right)^T\mathbf{S}^{(\tau)\alpha_i}A_1A_2d\alpha_1d\alpha_2\end{aligned}\tag{37}$$

In Eq. (37), the integration along the thickness direction is embedded into the definition of the generalized stress resultants vector $\mathbf{S}^{(\tau)\alpha_i}=\mathbf{S}^{(\tau)\alpha_i}(\alpha_1,\alpha_2,t)$, whose components are located along the reference surface and are defined for any $\tau=0,\dots,N+1$ and $i=1,2,3$. This vector takes the following extended representation:

$$\begin{aligned}\mathbf{S}^{(\tau)\alpha_i}&=\sum_{k=1}^{l}\int_{\zeta_k}^{\zeta_{k+1}}\left(\mathbf{Z}^{(k\tau)\alpha_i}\right)^T\boldsymbol{\sigma}^{(k)}H_1H_2d\zeta=\\&=\left[N_1^{(\tau)\alpha_i}\quad N_2^{(\tau)\alpha_i}\quad N_{12}^{(\tau)\alpha_i}\quad N_{21}^{(\tau)\alpha_i}\quad T_1^{(\tau)\alpha_i}\quad T_2^{(\tau)\alpha_i}\quad P_1^{(\tau)\alpha_i}\quad P_2^{(\tau)\alpha_i}\quad S_3^{(\tau)\alpha_i}\right]^T\end{aligned}\tag{38}$$

By substituting the 3D constitutive relationship from Eqs. (31) into Eq. (38) and the higher-order expansion of the kinematic relation as in Eq. (28), the following generalized constitutive relation is obtained:

$$\mathbf{S}^{(\tau)\alpha_i}=\sum_{\eta=0}^{N+1}\sum_{j=1}^{3}\mathbf{A}^{(\tau\eta)\alpha_i\alpha_j}\boldsymbol{\varepsilon}^{(\tau)\alpha_i}=\sum_{\eta=0}^{N+1}\sum_{j=1}^{3}\mathbf{A}^{(\tau\eta)\alpha_i\alpha_j}\mathbf{D}_{\Omega}^{\alpha_i}\mathbf{N}^T\overline{\mathbf{u}}^{(\tau)}\tag{39}$$

Here, $\mathbf{A}^{(\tau\eta)\alpha_i\alpha_j}$ denotes the generalized stiffness matrix of the laminate, defined for each $\tau,\eta=0,\dots,N+1$ and $i,j=1,2,3$. This matrix takes the following extended form [69]:

$$\mathbf{A}^{(\tau\eta)\alpha_i\alpha_j} = \begin{bmatrix} A^{(\tau\eta)[00]\alpha_i\alpha_j}_{11(20)} & A^{(\tau\eta)[00]\alpha_i\alpha_j}_{12(11)} & A^{(\tau\eta)[00]\alpha_i\alpha_j}_{16(20)} & A^{(\tau\eta)[00]\alpha_i\alpha_j}_{16(11)} & A^{(\tau\eta)[00]\alpha_i\alpha_j}_{14(20)} & A^{(\tau\eta)[00]\alpha_i\alpha_j}_{15(11)} & A^{(\tau\eta)[01]\alpha_i\alpha_j}_{14(10)} & A^{(\tau\eta)[01]\alpha_i\alpha_j}_{15(10)} & A^{(\tau\eta)[01]\alpha_i\alpha_j}_{13(10)} \\ A^{(\tau\eta)[00]\alpha_i\alpha_j}_{12(11)} & A^{(\tau\eta)[00]\alpha_i\alpha_j}_{22(02)} & A^{(\tau\eta)[00]\alpha_i\alpha_j}_{26(11)} & A^{(\tau\eta)[00]\alpha_i\alpha_j}_{26(02)} & A^{(\tau\eta)[00]\alpha_i\alpha_j}_{24(11)} & A^{(\tau\eta)[00]\alpha_i\alpha_j}_{25(02)} & A^{(\tau\eta)[01]\alpha_i\alpha_j}_{24(01)} & A^{(\tau\eta)[01]\alpha_i\alpha_j}_{25(01)} & A^{(\tau\eta)[01]\alpha_i\alpha_j}_{23(01)} \\ A^{(\tau\eta)[00]\alpha_i\alpha_j}_{16(20)} & A^{(\tau\eta)[00]\alpha_i\alpha_j}_{26(11)} & A^{(\tau\eta)[00]\alpha_i\alpha_j}_{66(20)} & A^{(\tau\eta)[00]\alpha_i\alpha_j}_{66(11)} & A^{(\tau\eta)[00]\alpha_i\alpha_j}_{46(20)} & A^{(\tau\eta)[00]\alpha_i\alpha_j}_{56(11)} & A^{(\tau\eta)[01]\alpha_i\alpha_j}_{46(10)} & A^{(\tau\eta)[01]\alpha_i\alpha_j}_{56(10)} & A^{(\tau\eta)[01]\alpha_i\alpha_j}_{36(10)} \\ A^{(\tau\eta)[00]\alpha_i\alpha_j}_{16(11)} & A^{(\tau\eta)[00]\alpha_i\alpha_j}_{26(02)} & A^{(\tau\eta)[00]\alpha_i\alpha_j}_{66(11)} & A^{(\tau\eta)[00]\alpha_i\alpha_j}_{66(02)} & A^{(\tau\eta)[00]\alpha_i\alpha_j}_{46(11)} & A^{(\tau\eta)[00]\alpha_i\alpha_j}_{56(02)} & A^{(\tau\eta)[01]\alpha_i\alpha_j}_{46(01)} & A^{(\tau\eta)[01]\alpha_i\alpha_j}_{56(01)} & A^{(\tau\eta)[01]\alpha_i\alpha_j}_{36(01)} \\ A^{(\tau\eta)[00]\alpha_i\alpha_j}_{14(20)} & A^{(\tau\eta)[00]\alpha_i\alpha_j}_{24(11)} & A^{(\tau\eta)[00]\alpha_i\alpha_j}_{46(20)} & A^{(\tau\eta)[00]\alpha_i\alpha_j}_{46(11)} & A^{(\tau\eta)[00]\alpha_i\alpha_j}_{44(20)} & A^{(\tau\eta)[00]\alpha_i\alpha_j}_{45(11)} & A^{(\tau\eta)[01]\alpha_i\alpha_j}_{44(10)} & A^{(\tau\eta)[01]\alpha_i\alpha_j}_{45(10)} & A^{(\tau\eta)[01]\alpha_i\alpha_j}_{34(10)} \\ A^{(\tau\eta)[00]\alpha_i\alpha_j}_{15(11)} & A^{(\tau\eta)[00]\alpha_i\alpha_j}_{25(02)} & A^{(\tau\eta)[00]\alpha_i\alpha_j}_{56(11)} & A^{(\tau\eta)[00]\alpha_i\alpha_j}_{56(02)} & A^{(\tau\eta)[00]\alpha_i\alpha_j}_{45(11)} & A^{(\tau\eta)[00]\alpha_i\alpha_j}_{55(02)} & A^{(\tau\eta)[01]\alpha_i\alpha_j}_{45(01)} & A^{(\tau\eta)[01]\alpha_i\alpha_j}_{55(01)} & A^{(\tau\eta)[01]\alpha_i\alpha_j}_{35(01)} \\ A^{(\tau\eta)[10]\alpha_i\alpha_j}_{14(10)} & A^{(\tau\eta)[10]\alpha_i\alpha_j}_{24(01)} & A^{(\tau\eta)[10]\alpha_i\alpha_j}_{46(10)} & A^{(\tau\eta)[10]\alpha_i\alpha_j}_{46(01)} & A^{(\tau\eta)[10]\alpha_i\alpha_j}_{44(10)} & A^{(\tau\eta)[10]\alpha_i\alpha_j}_{45(01)} & A^{(\tau\eta)[11]\alpha_i\alpha_j}_{44(00)} & A^{(\tau\eta)[11]\alpha_i\alpha_j}_{45(00)} & A^{(\tau\eta)[11]\alpha_i\alpha_j}_{34(00)} \\ A^{(\tau\eta)[10]\alpha_i\alpha_j}_{15(10)} & A^{(\tau\eta)[10]\alpha_i\alpha_j}_{25(01)} & A^{(\tau\eta)[10]\alpha_i\alpha_j}_{56(10)} & A^{(\tau\eta)[10]\alpha_i\alpha_j}_{56(01)} & A^{(\tau\eta)[10]\alpha_i\alpha_j}_{45(10)} & A^{(\tau\eta)[10]\alpha_i\alpha_j}_{55(01)} & A^{(\tau\eta)[11]\alpha_i\alpha_j}_{45(00)} & A^{(\tau\eta)[11]\alpha_i\alpha_j}_{55(00)} & A^{(\tau\eta)[11]\alpha_i\alpha_j}_{35(00)} \\ A^{(\tau\eta)[10]\alpha_i\alpha_j}_{13(10)} & A^{(\tau\eta)[10]\alpha_i\alpha_j}_{23(01)} & A^{(\tau\eta)[10]\alpha_i\alpha_j}_{36(10)} & A^{(\tau\eta)[10]\alpha_i\alpha_j}_{36(01)} & A^{(\tau\eta)[10]\alpha_i\alpha_j}_{34(10)} & A^{(\tau\eta)[10]\alpha_i\alpha_j}_{35(01)} & A^{(\tau\eta)[11]\alpha_i\alpha_j}_{34(00)} & A^{(\tau\eta)[11]\alpha_i\alpha_j}_{35(00)} & A^{(\tau\eta)[11]\alpha_i\alpha_j}_{33(00)} \end{bmatrix} \tag{40}$$

Introducing the positions $\partial^0 F_\tau^{(k)\alpha_i} / \partial\zeta^0 = F_\tau^{(k)\alpha_i}$ and $\partial^0 F_\eta^{(k)\alpha_j} / \partial\zeta^0 = F_\eta^{(k)\alpha_j}$, each element of matrix $\mathbf{A}^{(\tau\eta)\alpha_i\alpha_j}$, denoted by $A_{nm\ (pq)}^{(\tau\eta)[fg]\alpha_i\alpha_j}$, is evaluated as follows for each $\tau, \eta = 0, \dots, N+1$ and $i, j = 1, 2, 3$, setting $p, q = 0, 1, 2$, $f, g = 0, 1$ and $n, m = 1, \dots, 6$:

$$A_{nm\ (pq)}^{(\tau\eta)[fg]\alpha_i\alpha_j} = \sum_{k=1}^{l} \int_{\zeta_k}^{\zeta_{k+1}} \overline{B}_{nm}^{(k)} \frac{\partial^f F_\tau^{(k)\alpha_i}}{\partial\zeta^f} \frac{\partial^g F_\eta^{(k)\alpha_j}}{\partial\zeta^g} \frac{H_1 H_2}{H_1^p H_2^q} d\zeta \tag{41}$$

where the coefficients $\overline{B}_{nm}^{(k)}$ are equal to $\overline{E}_{nm}^{(k)}$ for any $n, m = 1, \dots, 6$. In case of lower-order theories, the 3D stiffness coefficients are expressed in terms of the shear correction factor $\kappa(\zeta)$, which is taken to be equal to 5/6 in this work, as follows:

$$\overline{B}_{nm}^{(k)} = \begin{cases} \overline{E}_{nm}^{(k)} & \text{for} \quad n, m = 1, 2, 3, 6 \\ \kappa(\zeta) \overline{E}_{nm}^{(k)} & \text{for} \quad n, m = 4, 5 \end{cases} \tag{42}$$

As can be seen, the generalized constitutive coefficients $A_{nm\ (pq)}^{(\tau\eta)[fg]\alpha_i\alpha_j}$ in Eq. (41) depend on the curvilinear coordinates α_1, α_2. The variability of these coefficients can be neglected by considering the through-the-thickness scaling parameters equal to 1, namely $H_i \cong 1$ for $i = 1, 2$. In this case, these coefficients can be evaluated from the relation reported in the following, derived from Eq. (41) under the assumption that $p = q = 1$:

$$A_{nm\ (pq)}^{(\tau\eta)[fg]\alpha_i\alpha_j} = \sum_{k=1}^{l} \int_{\zeta_k}^{\zeta_{k+1}} \overline{B}_{nm}^{(k)} \frac{\partial^f F_\tau^{(k)\alpha_i}}{\partial\zeta^f} \frac{\partial^g F_\eta^{(k)\alpha_j}}{\partial\zeta^g} d\zeta \tag{43}$$

Under these conditions, the generalized constitutive matrix takes the following extended form:

$$\mathbf{A}^{(\tau\eta)\alpha_i\alpha_j} \cong \begin{bmatrix} A^{(\tau\eta)[00]\alpha_i\alpha_j}_{11(11)} & A^{(\tau\eta)[00]\alpha_i\alpha_j}_{12(11)} & A^{(\tau\eta)[00]\alpha_i\alpha_j}_{16(11)} & A^{(\tau\eta)[00]\alpha_i\alpha_j}_{16(11)} & A^{(\tau\eta)[00]\alpha_i\alpha_j}_{14(11)} & A^{(\tau\eta)[00]\alpha_i\alpha_j}_{15(11)} & A^{(\tau\eta)[01]\alpha_i\alpha_j}_{14(11)} & A^{(\tau\eta)[01]\alpha_i\alpha_j}_{15(11)} & A^{(\tau\eta)[01]\alpha_i\alpha_j}_{13(11)} \\ A^{(\tau\eta)[00]\alpha_i\alpha_j}_{12(11)} & A^{(\tau\eta)[00]\alpha_i\alpha_j}_{22(11)} & A^{(\tau\eta)[00]\alpha_i\alpha_j}_{26(11)} & A^{(\tau\eta)[00]\alpha_i\alpha_j}_{26(11)} & A^{(\tau\eta)[00]\alpha_i\alpha_j}_{24(11)} & A^{(\tau\eta)[00]\alpha_i\alpha_j}_{25(11)} & A^{(\tau\eta)[01]\alpha_i\alpha_j}_{24(11)} & A^{(\tau\eta)[01]\alpha_i\alpha_j}_{25(11)} & A^{(\tau\eta)[01]\alpha_i\alpha_j}_{23(11)} \\ A^{(\tau\eta)[00]\alpha_i\alpha_j}_{16(11)} & A^{(\tau\eta)[00]\alpha_i\alpha_j}_{26(11)} & A^{(\tau\eta)[00]\alpha_i\alpha_j}_{66(11)} & A^{(\tau\eta)[00]\alpha_i\alpha_j}_{66(11)} & A^{(\tau\eta)[00]\alpha_i\alpha_j}_{46(11)} & A^{(\tau\eta)[00]\alpha_i\alpha_j}_{56(11)} & A^{(\tau\eta)[01]\alpha_i\alpha_j}_{46(11)} & A^{(\tau\eta)[01]\alpha_i\alpha_j}_{56(11)} & A^{(\tau\eta)[01]\alpha_i\alpha_j}_{36(11)} \\ A^{(\tau\eta)[00]\alpha_i\alpha_j}_{16(11)} & A^{(\tau\eta)[00]\alpha_i\alpha_j}_{26(11)} & A^{(\tau\eta)[00]\alpha_i\alpha_j}_{66(11)} & A^{(\tau\eta)[00]\alpha_i\alpha_j}_{66(11)} & A^{(\tau\eta)[00]\alpha_i\alpha_j}_{46(11)} & A^{(\tau\eta)[00]\alpha_i\alpha_j}_{56(11)} & A^{(\tau\eta)[01]\alpha_i\alpha_j}_{46(11)} & A^{(\tau\eta)[01]\alpha_i\alpha_j}_{56(11)} & A^{(\tau\eta)[01]\alpha_i\alpha_j}_{36(11)} \\ A^{(\tau\eta)[00]\alpha_i\alpha_j}_{14(11)} & A^{(\tau\eta)[00]\alpha_i\alpha_j}_{24(11)} & A^{(\tau\eta)[00]\alpha_i\alpha_j}_{46(11)} & A^{(\tau\eta)[00]\alpha_i\alpha_j}_{46(11)} & A^{(\tau\eta)[00]\alpha_i\alpha_j}_{44(11)} & A^{(\tau\eta)[00]\alpha_i\alpha_j}_{45(11)} & A^{(\tau\eta)[01]\alpha_i\alpha_j}_{44(11)} & A^{(\tau\eta)[01]\alpha_i\alpha_j}_{45(11)} & A^{(\tau\eta)[01]\alpha_i\alpha_j}_{34(11)} \\ A^{(\tau\eta)[00]\alpha_i\alpha_j}_{15(11)} & A^{(\tau\eta)[00]\alpha_i\alpha_j}_{25(11)} & A^{(\tau\eta)[00]\alpha_i\alpha_j}_{56(11)} & A^{(\tau\eta)[00]\alpha_i\alpha_j}_{56(11)} & A^{(\tau\eta)[00]\alpha_i\alpha_j}_{45(11)} & A^{(\tau\eta)[00]\alpha_i\alpha_j}_{55(11)} & A^{(\tau\eta)[01]\alpha_i\alpha_j}_{45(11)} & A^{(\tau\eta)[01]\alpha_i\alpha_j}_{55(11)} & A^{(\tau\eta)[01]\alpha_i\alpha_j}_{35(11)} \\ A^{(\tau\eta)[10]\alpha_i\alpha_j}_{14(11)} & A^{(\tau\eta)[10]\alpha_i\alpha_j}_{24(11)} & A^{(\tau\eta)[10]\alpha_i\alpha_j}_{46(11)} & A^{(\tau\eta)[10]\alpha_i\alpha_j}_{46(11)} & A^{(\tau\eta)[10]\alpha_i\alpha_j}_{44(11)} & A^{(\tau\eta)[10]\alpha_i\alpha_j}_{45(11)} & A^{(\tau\eta)[11]\alpha_i\alpha_j}_{44(11)} & A^{(\tau\eta)[11]\alpha_i\alpha_j}_{45(11)} & A^{(\tau\eta)[11]\alpha_i\alpha_j}_{34(11)} \\ A^{(\tau\eta)[10]\alpha_i\alpha_j}_{15(11)} & A^{(\tau\eta)[10]\alpha_i\alpha_j}_{25(11)} & A^{(\tau\eta)[10]\alpha_i\alpha_j}_{56(11)} & A^{(\tau\eta)[10]\alpha_i\alpha_j}_{56(11)} & A^{(\tau\eta)[10]\alpha_i\alpha_j}_{45(11)} & A^{(\tau\eta)[10]\alpha_i\alpha_j}_{55(11)} & A^{(\tau\eta)[11]\alpha_i\alpha_j}_{45(11)} & A^{(\tau\eta)[11]\alpha_i\alpha_j}_{55(11)} & A^{(\tau\eta)[11]\alpha_i\alpha_j}_{35(11)} \\ A^{(\tau\eta)[10]\alpha_i\alpha_j}_{13(11)} & A^{(\tau\eta)[10]\alpha_i\alpha_j}_{23(11)} & A^{(\tau\eta)[10]\alpha_i\alpha_j}_{36(11)} & A^{(\tau\eta)[10]\alpha_i\alpha_j}_{36(11)} & A^{(\tau\eta)[10]\alpha_i\alpha_j}_{34(11)} & A^{(\tau\eta)[10]\alpha_i\alpha_j}_{35(11)} & A^{(\tau\eta)[11]\alpha_i\alpha_j}_{34(11)} & A^{(\tau\eta)[11]\alpha_i\alpha_j}_{35(11)} & A^{(\tau\eta)[11]\alpha_i\alpha_j}_{33(11)} \end{bmatrix} \tag{44}$$

The virtual variation of the elastic strain energy, as presented in Eq. (37), is expressed as follows [69]:

$$\begin{aligned}\delta\Phi &= \sum_{\tau=0}^{N+1}\sum_{i=1}^{3}\int_{\alpha_1}\int_{\alpha_2}\left(\delta\boldsymbol{\varepsilon}^{(\tau)\alpha_i}\right)^T\mathbf{S}^{(\tau)\alpha_i}A_1A_2d\alpha_1d\alpha_2 = \\ &= \sum_{\tau=0}^{N+1}\sum_{\eta=0}^{N+1}\sum_{i=1}^{3}\sum_{j=1}^{3}\int_{\alpha_1}\int_{\alpha_2}\left(\delta\left(\mathbf{D}_\Omega^{\alpha_i}\mathbf{u}^{(\tau)}\right)\right)^T\mathbf{A}^{(\tau\eta)\alpha_i\alpha_j}\mathbf{D}_\Omega^{\alpha_j}\mathbf{u}^{(\eta)}A_1A_2d\alpha_1d\alpha_2 = \\ &= \sum_{\tau=0}^{N+1}\sum_{\eta=0}^{N+1}\sum_{i=1}^{3}\sum_{j=1}^{3}\int_{\alpha_1}\int_{\alpha_2}\left(\mathbf{D}_\Omega^{\alpha_i}\mathbf{N}^T\delta\overline{\mathbf{u}}^{(\tau)}\right)^T\mathbf{A}^{(\tau\eta)\alpha_i\alpha_j}\left(\mathbf{D}_\Omega^{\alpha_j}\mathbf{N}^T\overline{\mathbf{u}}^{(\eta)}\right)A_1A_2d\alpha_1d\alpha_2 = \\ &= \sum_{\tau=0}^{N+1}\sum_{\eta=0}^{N+1}\delta\overline{\mathbf{u}}^{(\tau)T}\left(\sum_{i=1}^{3}\sum_{j=1}^{3}\int_{\alpha_1}\int_{\alpha_2}\left(\mathbf{D}_\Omega^{\alpha_i}\mathbf{N}^T\right)^T\mathbf{A}^{(\tau\eta)\alpha_i\alpha_j}\left(\mathbf{D}_\Omega^{\alpha_j}\mathbf{N}^T\right)A_1A_2d\alpha_1d\alpha_2\right)\overline{\mathbf{u}}^{(\eta)} = \\ &= \sum_{\tau=0}^{N+1}\sum_{\eta=0}^{N+1}\delta\overline{\mathbf{u}}^{(\tau)T}\overline{\mathbf{K}}^{(\tau\eta)}\overline{\mathbf{u}}^{(\eta)}\end{aligned} \tag{45}$$

The generalized stiffness matrix $\overline{\mathbf{K}}^{(\tau\eta)}$ of size $(3I_NI_M)\times(3I_NI_M)$ can be, thus, defined as:

$$\begin{aligned}\overline{\mathbf{K}}^{(\tau\eta)} &= \sum_{i=1}^{3}\sum_{j=1}^{3}\int_{\alpha_1}\int_{\alpha_2}\left(\mathbf{D}_\Omega^{\alpha_i}\mathbf{N}^T\right)^T\mathbf{A}^{(\tau\eta)\alpha_i\alpha_j}\left(\mathbf{D}_\Omega^{\alpha_j}\mathbf{N}^T\right)A_1A_2d\alpha_1d\alpha_2 \\ &= \sum_{i=1}^{3}\sum_{j=1}^{3}\int_{\alpha_1}\int_{\alpha_2}\left(\mathbf{B}^{\alpha_i}\right)^T\mathbf{A}^{(\tau\eta)\alpha_i\alpha_j}\mathbf{B}^{\alpha_j}A_1A_2d\alpha_1d\alpha_2\end{aligned} \tag{46}$$

If $\overline{\mathbf{B}}^{\alpha_i} = \overline{\mathbf{D}}_\Omega^{\alpha_i}\overline{\mathbf{N}}^T$ are matrices of size $9\times(I_NI_M)$, one gets:

$$\overline{\mathbf{K}}^{(\tau\eta)} = \int_{\alpha_1}\int_{\alpha_2}\begin{bmatrix}\overline{\mathbf{K}}_s^{(\tau\eta)\alpha_1\alpha_1} & \overline{\mathbf{K}}_s^{(\tau\eta)\alpha_1\alpha_2} & \overline{\mathbf{K}}_s^{(\tau\eta)\alpha_1\alpha_3} \\ \overline{\mathbf{K}}_s^{(\tau\eta)\alpha_2\alpha_1} & \overline{\mathbf{K}}_s^{(\tau\eta)\alpha_2\alpha_2} & \overline{\mathbf{K}}_s^{(\tau\eta)\alpha_2\alpha_3} \\ \overline{\mathbf{K}}_s^{(\tau\eta)\alpha_3\alpha_1} & \overline{\mathbf{K}}_s^{(\tau\eta)\alpha_3\alpha_2} & \overline{\mathbf{K}}_s^{(\tau\eta)\alpha_3\alpha_3}\end{bmatrix}A_1A_2d\alpha_1d\alpha_2 \tag{47}$$

with $\overline{\mathbf{K}}_s^{(\tau\eta)\alpha_i\alpha_j} = \left(\overline{\mathbf{B}}^{\alpha_i}\right)^T\mathbf{A}^{(\tau\eta)\alpha_i\alpha_j}\overline{\mathbf{B}}^{\alpha_j}$. The virtual variation δT of the kinetic energy of the doubly-curved shell solid is computed according to the following relation:

$$\delta T = \sum_{k=1}^{l}\int_{\zeta_k}^{\zeta_{k+1}}\int_{\alpha_1}\int_{\alpha_2}\rho^{(k)}\left(\delta\dot{\mathbf{U}}^{(k)}\right)^T\dot{\mathbf{U}}^{(k)}H_1H_2A_1A_2d\alpha_1d\alpha_2d\zeta \tag{48}$$

where $\rho^{(k)}$ denotes the mass density of the constituent material in the k-th layer, while vector $\dot{\mathbf{U}}^{(k)} = \left[\dot{U}_1^{(k)} \quad \dot{U}_2^{(k)} \quad \dot{U}_3^{(k)}\right]^T$ contains the first-order time derivatives of the 3D displacement field components, namely $\dot{U}_i^{(k)} = \partial U_i^{(k)}/\partial t$ for $i = 1, 2, 3$. By applying the integration-by-parts rule [69] in the time integration of δT in Eq. (24), starting from Eq. (48), the relation reported below is obtained under the assumption of synchronous motion:

$$\int_{t_1}^{t_2}\delta T dt = -\sum_{k=1}^{l}\int_{t_1}^{t_2}\int_{\zeta_k}^{\zeta_{k+1}}\int_{\alpha_1}\int_{\alpha_2}\rho^{(k)}\left(\delta\mathbf{U}^{(k)}\right)^T\ddot{\mathbf{U}}^{(k)}H_1H_2A_1A_2d\alpha_1d\alpha_2d\zeta\, dt \tag{49}$$

where $\ddot{\mathbf{U}}^{(k)} = \left[\ddot{U}_1^{(k)} \quad \ddot{U}_2^{(k)} \quad \ddot{U}_3^{(k)}\right]^T$ with $\ddot{U}_i^{(k)} = \partial^2U_i^{(k)}/\partial t^2$ for $i = 1, 2, 3$. Introducing the higher-order kinematic model from Eq. (23), Eq. (49) becomes:

$$\delta T = -\sum_{\tau=0}^{N+1}\int_{\alpha_1}\int_{\alpha_2}\left(\delta\mathbf{u}^{(\tau)}\right)^T\left(\sum_{\eta=0}^{N+1}\mathbf{M}^{(\tau\eta)}\ddot{\mathbf{u}}^{(\eta)}\right)A_1A_2d\alpha_1d\alpha_2 \tag{50}$$

The higher-order mass matrix $\mathbf{M}^{(\tau\eta)}$ is defined for each $\tau, \eta = 0, \ldots, N+1$ as follows:

$$\mathbf{M}^{(\tau\eta)} = \begin{bmatrix}I_0^{(\tau\eta)\alpha_1\alpha_1} & 0 & 0 \\ 0 & I_0^{(\tau\eta)\alpha_2\alpha_2} & 0 \\ 0 & 0 & I_0^{(\tau\eta)\alpha_3\alpha_3}\end{bmatrix} \tag{51}$$

Furthermore, the inertia masses $I_0^{(\tau\eta)\alpha_i\alpha_i}$ with $i = 1, 2, 3$ introduced in Eq. (51) are defined from the following relation:

$$I_0^{(\tau\eta)\alpha_i\alpha_i} = \sum_{k=1}^{l}\int_{\zeta_k}^{\zeta_{k+1}}\rho^{(k)}F_\tau^{(k)\alpha_i}F_\eta^{(k)\alpha_i}H_1H_2d\zeta \tag{52}$$

Substituting the higher-order interpolation of the displacement field vector into Eq. (50), one gets [69]:

The mass matrix $\overline{\mathbf{M}}^{(\tau\eta)}$ defined in Eq. (53) takes the following integral form:

$$\begin{aligned}\overline{\mathbf{M}}^{(\tau\eta)} &= \int_{\alpha_1}\int_{\alpha_2}\begin{bmatrix}\overline{\mathbf{M}}^{(\tau\eta)\alpha_1\alpha_1} & \mathbf{0} & \mathbf{0} \\ \mathbf{0} & \overline{\mathbf{M}}^{(\tau\eta)\alpha_2\alpha_2} & \mathbf{0} \\ \mathbf{0} & \mathbf{0} & \overline{\mathbf{M}}^{(\tau\eta)\alpha_3\alpha_3}\end{bmatrix}A_1A_2d\alpha_1d\alpha_2 = \\ &\int_{\alpha_1}\int_{\alpha_2}\begin{bmatrix}\overline{\mathbf{N}}I_0^{(\tau\eta)\alpha_1\alpha_1}\overline{\mathbf{N}}^T & \mathbf{0} & \mathbf{0} \\ \mathbf{0} & \overline{\mathbf{N}}I_0^{(\tau\eta)\alpha_2\alpha_2}\overline{\mathbf{N}}^T & \mathbf{0} \\ \mathbf{0} & \mathbf{0} & \overline{\mathbf{N}}I_0^{(\tau\eta)\alpha_3\alpha_3}\overline{\mathbf{N}}^T\end{bmatrix}A_1A_2d\alpha_1d\alpha_2\end{aligned} \tag{54}$$

When the doubly-curved shell element is described in curvilinear principal coordinates, the physical domain $[\alpha_1^0, \alpha_1^1]\times[\alpha_2^0, \alpha_2^1]$ is rectangular. In the case of arbitrarily-shaped domains, generalized blending

$$\begin{aligned}\delta T = &-\sum_{\tau=0}^{N+1}\int_{\alpha_1}\int_{\alpha_2}\left(\left(\overline{\mathbf{N}}^T\delta\overline{\mathbf{u}}_1^{(\tau)}\right)^T\left(\sum_{\eta=0}^{N+1}I_0^{(\tau\eta)\alpha_1\alpha_1}\overline{\mathbf{N}}^T\ddot{\overline{\mathbf{u}}}_1^{(\eta)}\right) + \left(\overline{\mathbf{N}}^T\delta\overline{\mathbf{u}}_2^{(\tau)}\right)^T\left(\sum_{\eta=0}^{N+1}I_0^{(\tau\eta)\alpha_2\alpha_2}\overline{\mathbf{N}}^T\ddot{\overline{\mathbf{u}}}_2^{(\eta)}\right) + \right. \\ &\left. + \left(\overline{\mathbf{N}}^T\delta\overline{\mathbf{u}}_3^{(\tau)}\right)^T\left(\sum_{\eta=0}^{N+1}I_0^{(\tau\eta)\alpha_3\alpha_3}\overline{\mathbf{N}}^T\ddot{\overline{\mathbf{u}}}_3^{(\eta)}\right)\right)A_1A_2d\alpha_1d\alpha_2 = \\ &= -\sum_{\tau=0}^{N+1}\int_{\alpha_1}\int_{\alpha_2}\left(\left(\delta\overline{\mathbf{u}}_1^{(\tau)}\right)^T\left(\sum_{\eta=0}^{N+1}\overline{\mathbf{N}}I_0^{(\tau\eta)\alpha_1\alpha_1}\overline{\mathbf{N}}^T\right)\ddot{\overline{\mathbf{u}}}_1^{(\eta)} + \left(\delta\overline{\mathbf{u}}_2^{(\tau)}\right)^T\left(\sum_{\eta=0}^{N+1}\overline{\mathbf{N}}I_0^{(\tau\eta)\alpha_2\alpha_2}\overline{\mathbf{N}}^T\right)\ddot{\overline{\mathbf{u}}}_2^{(\eta)} + \right. \\ &\left. + \left(\delta\overline{\mathbf{u}}_3^{(\tau)}\right)^T\left(\sum_{\eta=0}^{N+1}\overline{\mathbf{N}}I_0^{(\tau\eta)\alpha_3\alpha_3}\overline{\mathbf{N}}^T\right)\ddot{\overline{\mathbf{u}}}_3^{(\eta)}\right)A_1A_2d\alpha_1d\alpha_2 = -\sum_{\tau=0}^{N+1}\sum_{\eta=0}^{N+1}\left(\delta\overline{\mathbf{u}}^{(\tau)}\right)^T\overline{\mathbf{M}}^{(\tau\eta)}\ddot{\overline{\mathbf{u}}}^{(\eta)}\end{aligned} \tag{53}$$

functions $\alpha_1(\xi_1,\xi_2)$ and $\alpha_2(\xi_1,\xi_2)$ are used to map the domain. These functions adopt the natural coordinates ξ_1 and ξ_2, defined so that $(\xi_1,\xi_2) \in [-1,+1]\times[-1,+1]$. These functions are provided in the following expressions, see also Ref. [69]:

$$\begin{aligned}\alpha_1(\xi_1,\xi_2) = {}&\frac{1}{2}((1-\xi_2)\overline{\alpha}_{1(1)}(\xi_1)+(1+\xi_1)\overline{\alpha}_{1(2)}(\xi_2)+(1+\xi_2)\overline{\alpha}_{1(3)}(\xi_1)+(1-\xi_1)\overline{\alpha}_{1(4)}(\xi_2))+\\ &-\frac{1}{4}((1-\xi_1)(1-\xi_2)\alpha_{1(1)}+(1+\xi_1)(1-\xi_2)\alpha_{1(2)}+(1+\xi_1)(1+\xi_2)\alpha_{1(3)}+(1-\xi_1)(1+\xi_2)\alpha_{1(4)})\end{aligned} \tag{55}$$

$$\begin{aligned}\alpha_2(\xi_1,\xi_2) = {}&\frac{1}{2}((1-\xi_2)\overline{\alpha}_{2(1)}(\xi_1)+(1+\xi_1)\overline{\alpha}_{2(2)}(\xi_2)+(1+\xi_2)\overline{\alpha}_{2(3)}(\xi_1)+(1-\xi_1)\overline{\alpha}_{2(4)}(\xi_2))+\\ &-\frac{1}{4}((1-\xi_1)(1-\xi_2)\alpha_{2(1)}+(1+\xi_1)(1-\xi_2)\alpha_{2(2)}+(1+\xi_1)(1+\xi_2)\alpha_{2(3)}+(1-\xi_1)(1+\xi_2)\alpha_{2(4)})\end{aligned} \tag{56}$$

In Eqs. (55) and (56), $(\overline{\alpha}_{1(1)},\overline{\alpha}_{2(1)})$, $(\overline{\alpha}_{1(2)},\overline{\alpha}_{2(2)})$, $(\overline{\alpha}_{1(3)},\overline{\alpha}_{2(3)})$, and $(\overline{\alpha}_{1(4)},\overline{\alpha}_{2(4)})$ are the functions that describe the curves of the distorted domain in the parametric space, while $(\alpha_{1(1)},\alpha_{2(1)})$, $(\alpha_{1(2)},\alpha_{2(2)})$, $(\alpha_{1(3)},\alpha_{2(3)})$ and $(\alpha_{1(4)},\alpha_{2(4)})$ denote the four corners of the distorted domain. Starting from Eqs. (55) and (56), the derivation operation with respect to α_1,α_2 is expressed in terms of the derivatives with respect to the natural coordinates ξ_1,ξ_2 using the chain rule. The resulting relation is:

$$\begin{bmatrix}\dfrac{\partial}{\partial\alpha_1}\\[2mm] \dfrac{\partial}{\partial\alpha_2}\end{bmatrix} = \begin{bmatrix}\dfrac{\partial\xi_1}{\partial\alpha_1} & \dfrac{\partial\xi_2}{\partial\alpha_1}\\[2mm] \dfrac{\partial\xi_1}{\partial\alpha_2} & \dfrac{\partial\xi_2}{\partial\alpha_2}\end{bmatrix} \begin{bmatrix}\dfrac{\partial}{\partial\xi_1}\\[2mm] \dfrac{\partial}{\partial\xi_2}\end{bmatrix} = \begin{bmatrix}\xi_{1,\alpha_1} & \xi_{2,\alpha_1}\\ \xi_{1,\alpha_2} & \xi_{2,\alpha_2}\end{bmatrix} \begin{bmatrix}\dfrac{\partial}{\partial\xi_1}\\[2mm] \dfrac{\partial}{\partial\xi_2}\end{bmatrix} \tag{57}$$

In the same way, since the blending functions in Eqs. (55) and (56) must be invertible, the derivatives with respect to ξ_1,ξ_2 can be, also, expressed in terms of α_1,α_2. This leads to the definition of the Jacobian operator $\mathbf{J}$ associated with the mapping transformation of Eqs. (55) and (56). One gets:

$$\begin{bmatrix}\dfrac{\partial}{\partial\xi_1}\\[2mm] \dfrac{\partial}{\partial\xi_2}\end{bmatrix} = \begin{bmatrix}\dfrac{\partial\alpha_1}{\partial\xi_1} & \dfrac{\partial\alpha_2}{\partial\xi_1}\\[2mm] \dfrac{\partial\alpha_1}{\partial\xi_2} & \dfrac{\partial\alpha_2}{\partial\xi_2}\end{bmatrix} \begin{bmatrix}\dfrac{\partial}{\partial\alpha_1}\\[2mm] \dfrac{\partial}{\partial\alpha_2}\end{bmatrix} = \mathbf{J}\begin{bmatrix}\dfrac{\partial}{\partial\alpha_1}\\[2mm] \dfrac{\partial}{\partial\alpha_2}\end{bmatrix} \tag{58}$$

The determinant of the operator $\mathbf{J}$ is, thus, computed as [69]:

$$\det(\mathbf{J}) = \frac{\partial\alpha_1}{\partial\xi_1}\frac{\partial\alpha_2}{\partial\xi_2} - \frac{\partial\alpha_2}{\partial\xi_1}\frac{\partial\alpha_1}{\partial\xi_2} \tag{59}$$

If $\mathbf{J}$ is nonsingular at any point of the domain, namely $\det(\mathbf{J}) \neq 0$, Eq. (58) can be inverted, as shown in the relation below, where the inverse Jacobian operator $\mathbf{J}^{-1}$ is introduced:

$$\begin{aligned}\begin{bmatrix}\dfrac{\partial}{\partial\alpha_1}\\[2mm] \dfrac{\partial}{\partial\alpha_2}\end{bmatrix} &= \mathbf{J}^{-1}\begin{bmatrix}\dfrac{\partial}{\partial\xi_1}\\[2mm] \dfrac{\partial}{\partial\xi_2}\end{bmatrix} = \begin{bmatrix}\dfrac{\partial\xi_1}{\partial\alpha_1} & \dfrac{\partial\xi_2}{\partial\alpha_1}\\[2mm] \dfrac{\partial\xi_1}{\partial\alpha_2} & \dfrac{\partial\xi_2}{\partial\alpha_2}\end{bmatrix} \begin{bmatrix}\dfrac{\partial}{\partial\xi_1}\\[2mm] \dfrac{\partial}{\partial\xi_2}\end{bmatrix}\\ &= \frac{1}{\det(\mathbf{J})}\begin{bmatrix}\dfrac{\partial\alpha_2}{\partial\xi_2} & -\dfrac{\partial\alpha_2}{\partial\xi_1}\\[2mm] -\dfrac{\partial\alpha_1}{\partial\xi_2} & \dfrac{\partial\alpha_1}{\partial\xi_1}\end{bmatrix} \begin{bmatrix}\dfrac{\partial}{\partial\xi_1}\\[2mm] \dfrac{\partial}{\partial\xi_2}\end{bmatrix}\end{aligned} \tag{60}$$

By comparing Eq. (60) with Eq. (57), the following expressions are derived for the quantities $\xi_{1,\alpha_1},\xi_{2,\alpha_1},\xi_{1,\alpha_2},\xi_{2,\alpha_2}$:

$$\begin{aligned}&\xi_{1,\alpha_1} = \frac{1}{\det(\mathbf{J})}\frac{\partial\alpha_2}{\partial\xi_2}, \quad \xi_{2,\alpha_1} = -\frac{1}{\det(\mathbf{J})}\frac{\partial\alpha_2}{\partial\xi_1}\\ &\xi_{1,\alpha_2} = -\frac{1}{\det(\mathbf{J})}\frac{\partial\alpha_1}{\partial\xi_2}, \quad \xi_{2,\alpha_2} = \frac{1}{\det(\mathbf{J})}\frac{\partial\alpha_1}{\partial\xi_1}\end{aligned} \tag{61}$$

The procedure outlined in Eqs. (57)–(61) is, then, applied to second-order derivatives, leading to similar definitions as in Eq. (61). It should be noted that the edges of the distorted domain, labelled by $(\overline{\alpha}_{1(\lambda)},\overline{\alpha}_{2(\lambda)})$ for $\lambda = 1,...,4$ in Eqs. (55) and (56), are described using NURBS curves, in line with CAD geometric principles. The λ-th curve, denoted by $\mathbf{C}^{(\lambda)}(u)$, is defined in terms of the parameter $u \in [a,b]$ and $a,b \in \mathbb{R}$ from a set of $n^{(\lambda)}$ control points denoted by $\mathbf{P}_i^{(\lambda)} = \mathbf{P}^{(\lambda)}(\alpha_{1i},\alpha_{2i})$ with $i = 1,...,n^{(\lambda)}$, using a set of $n^{(\lambda)}+1$ B-Spline functions of order $p^{(\lambda)}$, denoted by $N_{i,p^{(\lambda)}}^{(\lambda)}(u)$ with $i = 0,...,n^{(\lambda)}$, according to the following relation [69]:

$$\mathbf{C}^{(\lambda)}(u) = (\overline{\alpha}_{1(\lambda)}(u),\overline{\alpha}_{2(\lambda)}(u)) = \frac{\sum\limits_{i=0}^{n^{(\lambda)}} N_{i,p^{(\lambda)}}^{(\lambda)}(u)w_i^{(\lambda)}\mathbf{P}^{(\lambda)}(\alpha_{1i},\alpha_{2i})}{\sum\limits_{i=0}^{n^{(\lambda)}} N_{i,p^{(\lambda)}}^{(\lambda)}(u)w_i^{(\lambda)}} \tag{62}$$

where $u \in [a,b] \equiv [0,1]$. Furthermore, according to Eqs. (55) and (56), the free parameter $u \in [0,1]$ is transformed into the natural coordinates $\xi_i = \xi_1,\xi_2 \in [-1,1]$ using the following coordinate transformation:

$$\xi_i = \frac{2}{b-a}(u-a)-1 = 2u-1 \tag{63}$$

It should be noted that the edges of the mapped domain associated with $\lambda = 1$ and $\lambda = 3$ are described in terms of $\xi_1 \in [-1,1]$, while the natural coordinate for $\lambda = 2$ and $\lambda = 4$ is $\xi_2 \in [-1,1]$. The arbitrary control point $\mathbf{P}_i^{(\lambda)} = \mathbf{P}^{(\lambda)}(\alpha_{1i},\alpha_{2i})$ associated with the λ-th curve with $\lambda = 1,...,4$ can be represented as follows:

$$\begin{aligned}\mathbf{P}^{(\lambda)}(\alpha_{1i},\alpha_{2i}) &= r_1^{(\lambda)}(\alpha_{1i},\alpha_{2i})\mathbf{e}_1 + r_2^{(\lambda)}(\alpha_{1i},\alpha_{2i})\mathbf{e}_2 + r_3^{(\lambda)}(\alpha_{1i},\alpha_{2i})\mathbf{e}_3\\ &= \begin{bmatrix}r_1^{(\lambda)}(\alpha_{1i},\alpha_{2i})\\ r_2^{(\lambda)}(\alpha_{1i},\alpha_{2i})\\ r_3^{(\lambda)}(\alpha_{1i},\alpha_{2i})\end{bmatrix}\end{aligned} \tag{64}$$

In Eq. (62), the basis function is defined over the interval $[a,b] = [0, 1]$, while $w_i^{(\lambda)}$ are proper weighting coefficients, which are recursively calculated from a knot vector $\boldsymbol{\Omega}^{(\lambda)}$ consisting of $m^{(\lambda)}$ breakpoints, defined as:

$$\boldsymbol{\Omega}^{(\lambda)} = \left[\underbrace{a^{(\lambda)}, \ \cdots, \ a^{(\lambda)}}_{p^{(\lambda)}+1}, \ u_{p^{(\lambda)}+1}, \ \cdots, \ u_{m^{(\lambda)}-p^{(\lambda)}-1}, \underbrace{b^{(\lambda)}, \ \cdots, \ b^{(\lambda)}}_{p^{(\lambda)}+1} \right] \tag{65}$$

Once the NURBS-based blending functions are introduced as in Eqs. (55) and (56), a local coordinate system is defined, consisting of the unit vectors $\mathbf{n}_s$, $\mathbf{n}_n$ and $\mathbf{n}_\zeta$, whose components are expressed from the principal directions of the shell $\alpha_1, \alpha_2, \zeta$ using the cosine directors of these vectors, as follows:

$$\begin{aligned} \mathbf{n}_n &= \begin{bmatrix} n_{n1} & n_{n2} & n_{n3} \end{bmatrix}^T, \\ \mathbf{n}_s &= \begin{bmatrix} n_{s1} & n_{s2} & n_{s3} \end{bmatrix}^T, \\ \mathbf{n}_\zeta &= \begin{bmatrix} n_{\zeta1} & n_{\zeta2} & n_{\zeta3} \end{bmatrix}^T \end{aligned} \tag{66}$$

In particular, $\mathbf{n}_n, \mathbf{n}_s$ denote the normal and the tangential vector of an arbitrary curve resting on the reference surface, while $\mathbf{n}_\zeta = \mathbf{n}$ coincides with the outward normal unit vector of the reference surface, already introduced in Eq. (5). In this way, the values $n_{n3}, n_{s3}, n_{\zeta1}, n_{\zeta2} = 0$ and $n_{\zeta3} = 1$ can be given to these quantities. The generalized displacement field vector $\mathbf{u}^{(\tau)} = \begin{bmatrix} u_1^{(\tau)} & u_2^{(\tau)} & u_3^{(\tau)} \end{bmatrix}^T$, whose components $u_1^{(\tau)}, u_2^{(\tau)}, u_3^{(\tau)}$ are referred to $\alpha_1, \alpha_2, \zeta$, can be, thus, expressed in terms of the components $u_n^{(\tau)}, u_s^{(\tau)}, u_\zeta^{(\tau)}$ associated with the axes of Eq. (66) using the transformation reported below [69]:

$$\begin{bmatrix} u_n^{(\tau)} \\ u_s^{(\tau)} \\ u_\zeta^{(\tau)} \end{bmatrix} = \begin{bmatrix} n_{n1} & n_{n2} & 0 \\ n_{s1} & n_{s2} & 0 \\ 0 & 0 & 1 \end{bmatrix} \begin{bmatrix} u_1^{(\tau)} \\ u_2^{(\tau)} \\ u_3^{(\tau)} \end{bmatrix} \tag{67}$$

Similarly, the higher-order generalized stress resultants $N_1^{(\tau)\alpha_1}, N_2^{(\tau)\alpha_2}, N_{12}^{(\tau)\alpha_2}, N_{21}^{(\tau)\alpha_1}, T_1^{(\tau)\alpha_3}, T_2^{(\tau)\alpha_3}$, defined with respect to the principal reference system, are transformed into the quantities $N_n^{(\tau)}, N_{ns}^{(\tau)}, T_\zeta^{(\tau)}$, as follows [69]:

$$\begin{aligned} N_n^{(\tau)} &= N_1^{(\tau)\alpha_1} n_{n1}^2 + N_2^{(\tau)\alpha_2} n_{n2}^2 + N_{12}^{(\tau)\alpha_2} n_{n1} n_{n2} + N_{21}^{(\tau)\alpha_1} n_{n1} n_{n2} \\ N_{ns}^{(\tau)} &= N_1^{(\tau)\alpha_1} n_{n1} n_{s1} + N_2^{(\tau)\alpha_2} n_{n2} n_{s2} + N_{12}^{(\tau)\alpha_2} n_{n1} n_{s2} + N_{21}^{(\tau)\alpha_1} n_{n2} n_{s1} \\ T_\zeta^{(\tau)} &= T_1^{(\tau)\alpha_3} n_{n1} + T_2^{(\tau)\alpha_3} n_{n2} \end{aligned} \tag{68}$$

Finally, the higher-order stiffness matrix $\overline{\mathbf{K}}^{(\tau\eta)}$ and the generalized mass matrix $\overline{\mathbf{M}}^{(\tau\eta)}$ from Eqs. (47) and (54), respectively, are evaluated using the natural coordinates ξ_1, ξ_2 in the 2D integrals, as follows:

$$\begin{aligned} \overline{\mathbf{K}}^{(\tau\eta)} &= \int_{-1}^{1}\int_{-1}^{1} \begin{bmatrix} \overline{\mathbf{K}}^{(\tau\eta)\alpha_1\alpha_1} & \overline{\mathbf{K}}^{(\tau\eta)\alpha_1\alpha_2} & \overline{\mathbf{K}}^{(\tau\eta)\alpha_1\alpha_3} \\ \overline{\mathbf{K}}^{(\tau\eta)\alpha_2\alpha_1} & \overline{\mathbf{K}}^{(\tau\eta)\alpha_2\alpha_2} & \overline{\mathbf{K}}^{(\tau\eta)\alpha_2\alpha_3} \\ \overline{\mathbf{K}}^{(\tau\eta)\alpha_3\alpha_1} & \overline{\mathbf{K}}^{(\tau\eta)\alpha_3\alpha_2} & \overline{\mathbf{K}}^{(\tau\eta)\alpha_3\alpha_3} \end{bmatrix} A_1 A_2 \det(J) d\xi_1 d\xi_2 \\ \overline{\mathbf{M}}^{(\tau\eta)} &= \int_{-1}^{1}\int_{-1}^{1} \begin{bmatrix} \overline{\mathbf{M}}^{(\tau\eta)\alpha_1\alpha_1} & \mathbf{0} & \mathbf{0} \\ \mathbf{0} & \overline{\mathbf{M}}^{(\tau\eta)\alpha_2\alpha_2} & \mathbf{0} \\ \mathbf{0} & \mathbf{0} & \overline{\mathbf{M}}^{(\tau\eta)\alpha_3\alpha_3} \end{bmatrix} A_1 A_2 \det(J) d\xi_1 d\xi_2 \end{aligned} \tag{69}$$

Finally, the fundamental equations can be expressed in their weak form for an arbitrary $\tau = 0, \ldots, N+1$ [69]:

$$\sum_{\eta=0}^{N+1} \overline{\mathbf{K}}^{(\tau\eta)} \overline{\mathbf{u}}^{(\eta)} + \sum_{\eta=0}^{N+1} \overline{\mathbf{M}}^{(\tau\eta)} \ddot{\overline{\mathbf{u}}}^{(\eta)} = \mathbf{0} \tag{70}$$

Eq. (70) is provided below in the assembled form to consider the entire kinematic expansion in Eq. (11) from $\tau = 0$ up to $\tau = N+1$:

$$\begin{aligned} &\begin{bmatrix} \overline{\mathbf{K}}^{(00)} & \overline{\mathbf{K}}^{(01)} & \cdots & \overline{\mathbf{K}}^{(0(N))} & \overline{\mathbf{K}}^{(0(N+1))} \\ \overline{\mathbf{K}}^{(10)} & \overline{\mathbf{K}}^{(11)} & \cdots & \overline{\mathbf{K}}^{(1(N))} & \overline{\mathbf{K}}^{(1(N+1))} \\ \vdots & \vdots & \ddots & \vdots & \vdots \\ \overline{\mathbf{K}}^{((N)0)} & \overline{\mathbf{K}}^{((N)1)} & \cdots & \overline{\mathbf{K}}^{((N)(N))} & \overline{\mathbf{K}}^{((N)(N+1))} \\ \overline{\mathbf{K}}^{((N+1)0)} & \overline{\mathbf{K}}^{((N+1)1)} & \cdots & \overline{\mathbf{K}}^{((N+1)(N))} & \overline{\mathbf{K}}^{((N+1)(N+1))} \end{bmatrix} \begin{bmatrix} \overline{\mathbf{u}}^{(0)} \\ \overline{\mathbf{u}}^{(1)} \\ \vdots \\ \overline{\mathbf{u}}^{(N)} \\ \overline{\mathbf{u}}^{(N+1)} \end{bmatrix} + \\ &+ \begin{bmatrix} \overline{\mathbf{M}}^{(00)} & \overline{\mathbf{M}}^{(01)} & \cdots & \overline{\mathbf{M}}^{(0(N))} & \overline{\mathbf{M}}^{(0(N+1))} \\ \overline{\mathbf{M}}^{(10)} & \overline{\mathbf{M}}^{(11)} & \cdots & \overline{\mathbf{M}}^{(1(N))} & \overline{\mathbf{M}}^{(1(N+1))} \\ \vdots & \vdots & \ddots & \vdots & \vdots \\ \overline{\mathbf{M}}^{((N)0)} & \overline{\mathbf{M}}^{((N)1)} & \cdots & \overline{\mathbf{M}}^{((N)(N))} & \overline{\mathbf{M}}^{((N)(N+1))} \\ \overline{\mathbf{M}}^{((N+1)0)} & \overline{\mathbf{M}}^{((N+1)1)} & \cdots & \overline{\mathbf{M}}^{((N+1)(N))} & \overline{\mathbf{M}}^{((N+1)(N+1))} \end{bmatrix} \begin{bmatrix} \ddot{\overline{\mathbf{u}}}^{(0)} \\ \ddot{\overline{\mathbf{u}}}^{(1)} \\ \vdots \\ \ddot{\overline{\mathbf{u}}}^{(N)} \\ \ddot{\overline{\mathbf{u}}}^{(N+1)} \end{bmatrix} = \begin{bmatrix} \mathbf{0} \\ \mathbf{0} \\ \vdots \\ \mathbf{0} \\ \mathbf{0} \end{bmatrix} \end{aligned} \tag{71}$$

Introducing the following expression, based on variables separation, for the displacement field vector $\overline{\mathbf{u}}^{(\tau)}$ in terms of circular frequency $\omega = 2\pi f$, where f is the natural frequency, and $\overline{\mathbf{U}}^{(\tau)}$ the mode shape vector:

$$\overline{\mathbf{u}}^{(\tau)}(\alpha_{1f}, \alpha_{2g}, t) = \overline{\mathbf{U}}^{(\tau)}(\alpha_{1f}, \alpha_{2g})e^{i\omega t} \tag{72}$$

the weak form of the governing equations in Eq. (70) becomes:

$$\sum_{\eta=0}^{N+1} \overline{\mathbf{K}}^{(\tau\eta)}\overline{\mathbf{U}}^{(\eta)} = \omega^2 \sum_{\eta=0}^{N+1} \overline{\mathbf{M}}^{(\tau\eta)}\overline{\mathbf{U}}^{(\eta)} \tag{73}$$

3. Numerical implementation

In this section, some key aspects are discussed regarding the numerical implementation of the dynamic governing equations of the problem under consideration, which are derived in their weak form. In particular, the GDQ method is introduced for the approximation of derivatives, while the GIQ method is used to numerically compute the various integrals, including those appearing in Eqs. (41) and (52). Unlike traditional numerical approaches, which are usually based on the discretization of the unknown function on a computational grid, the GDQ method directly approximates the derivatives of arbitrary order. If we denote a one-dimensional smooth function defined over a closed interval $[a, b]$ with $a, b \in \mathbb{R}$ with $f = f(x)$, the n-th order derivative of f at an arbitrary point $x = x_i$ of a discrete grid with $x_i \in [a, b]$ of elements I_Q, where $i = 1,\ldots,I_Q$, is expressed in terms of the values $f(x_j)$ of the function at the node x_j, for $j = 1, \ldots, I_Q$ [51]:

$$\left.\frac{\partial^n f(x)}{\partial x^n}\right|_{x=x_i} \cong \sum_{j=1}^{I_Q} \varsigma_{ij}^{(n)} f(x_j) \tag{74}$$

In Eq. (74), $\varsigma_{ij}^{(n)}$ denotes the weighting coefficients for the n-th order derivative, introduced for any $i, j = 1, \ldots, I_Q$. These coefficients are computed using the following recursive relationship [51], where $\mathscr{L}^{(1)}(x_i), \mathscr{L}^{(1)}(x_j)$ represent the values of the first-order derivative of the Lagrange interpolating polynomials at the sample points x_i and x_j, respectively:

$$\begin{aligned}
&\varsigma_{ij}^{(1)} = \frac{\mathscr{L}^{(1)}(x_i)}{(x_i - x_j)\mathscr{L}^{(1)}(x_j)} = \frac{\prod\limits_{k=1,\,k\neq i}^{N}(x_i - x_k)}{(x_i - x_j)\prod\limits_{k=1,\,k\neq j}^{N}(x_j - x_k)} && \text{for } i \neq j \\
&\varsigma_{ij}^{(n)} = n\left(\varsigma_{ij}^{(1)}\varsigma_{ii}^{(n-1)} - \frac{\varsigma_{ii}^{(n-1)}}{x_i - x_j}\right) && \text{for } i \neq j,\quad n > 1 \\
&\varsigma_{ii}^{(n)} = -\sum_{j=1 j\neq i}^{N} \varsigma_{ij}^{(n)} && \text{for } i = j,\quad \forall n
\end{aligned} \tag{75}$$

For the sake of completeness, the position $\varsigma_{ij}^{(0)} = \delta_{ij}$ should be considered, δ_{ij} being the well-known Kronecker delta operator. When $[a, b] \equiv [-1, 1]$, the GDQ weighting coefficients are denoted by $\tilde{\varsigma}_{ij}^{(n)}$. In this work, the GDQ coefficients are evaluated for the closed interval $[-1, 1]$, where a discretization of arbitrary sample point $\overline{x}_i$ is introduced. Then, the following coordinate transformation is considered for each node, leading to the definition of the position x_i, for $i = 1,\ldots,I_Q$, with respect to the interval $[a, b]$:

$$x_i = \frac{x_{I_Q} - x_1}{\overline{x}_{I_Q} - \overline{x}_1}(\overline{x}_i - \overline{x}_1) + x_1 \tag{76}$$

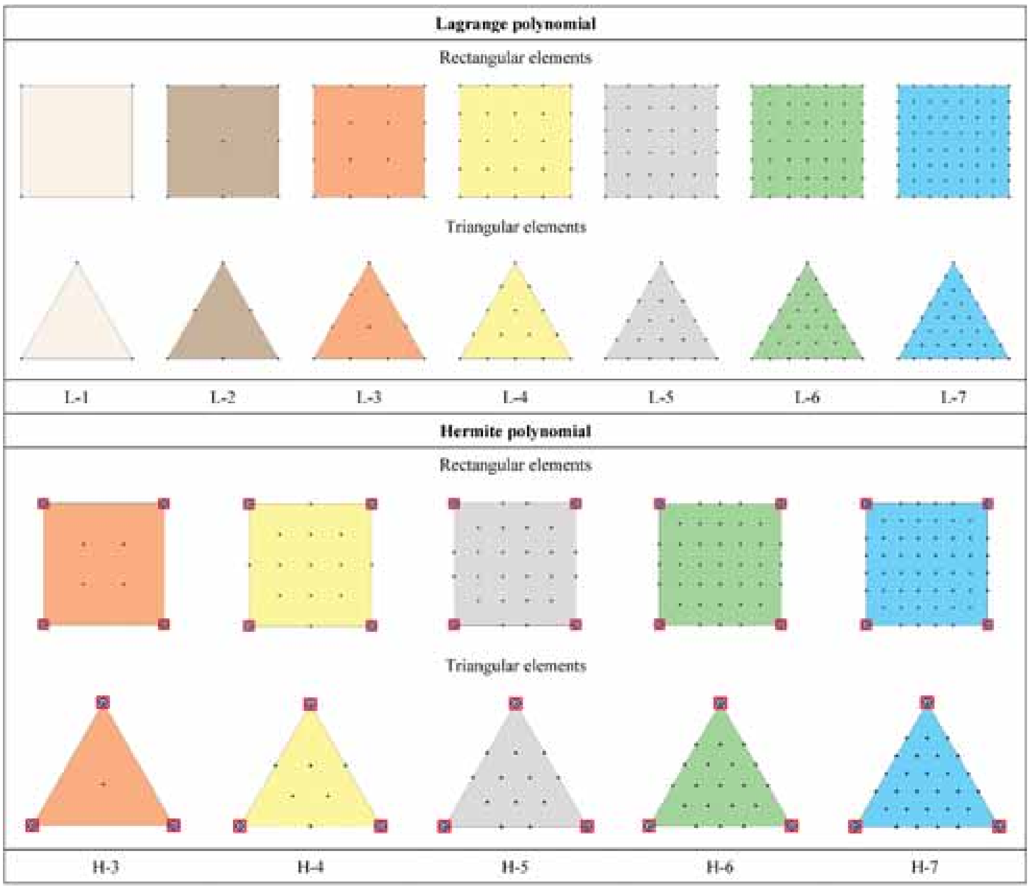

Fig. 1. Representation of the location of nodes in rectangular and triangular finite elements of various orders adopted in 2D simulations, taking into account Lagrange and Hermite shape functions.

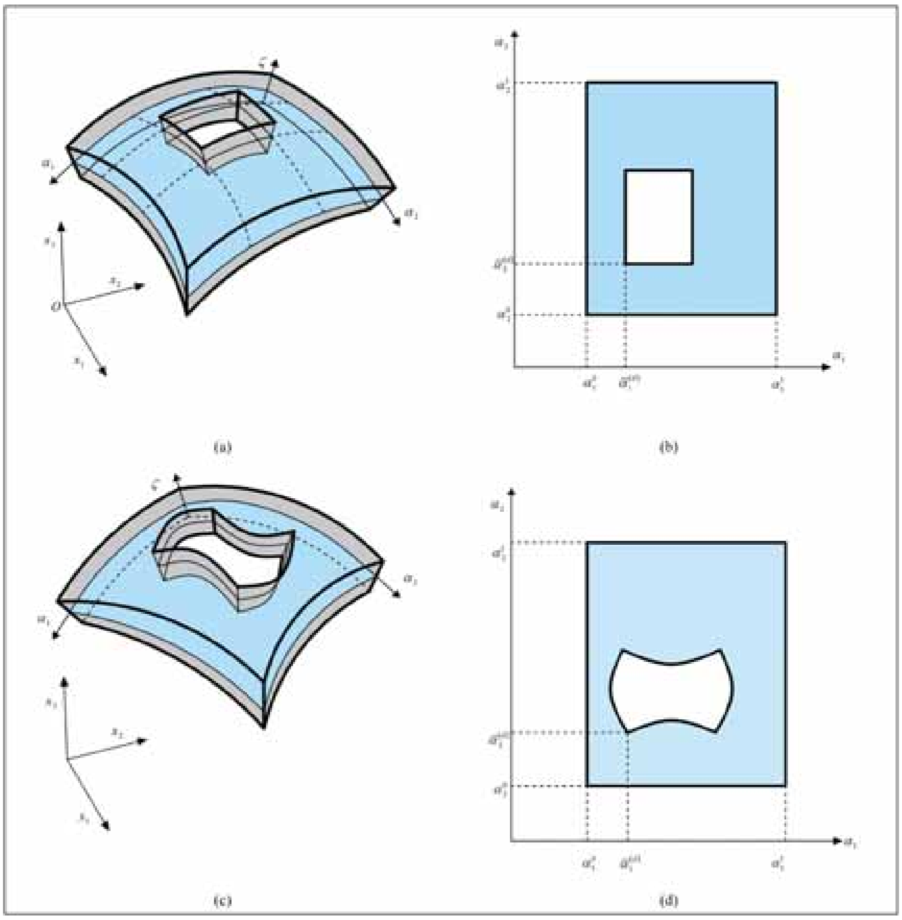

Fig. 2. Schematic representation of an arbitrary *d*-th rectangular hole within a doubly-curved shell element. 3D representation of a doubly-curved shell with rectangular hole (a) and representation of the hole in the rectangular physical domain (b). Generalization to an arbitrarily-shaped hole (c) and representation of the new physical domain (d).

Finally, the weighting coefficients $\varsigma_{ij}^{(n)}$ for the n-th order derivative that must be adopted in Eq. (74) are derived from those $\widetilde{\varsigma}_{ij}^{(n)}$ associated with $[-1,1]$, using the following relation derived in Ref. [51]:

$$\varsigma_{ij}^{(n)} = \left(\frac{\overline{x}_{I_Q} - \overline{x}_1}{x_{I_Q} - x_1}\right)^n \widetilde{\varsigma}_{ij}^{(n)} \tag{77}$$

Starting from the GDQ coefficients $\widetilde{\varsigma}_{ij}^{(1)}$ for the first-order derivative for $[-1,1]$, the so-called shifted coefficients $\overline{\varsigma}_{ij}^{(1)}$ are evaluated for any $i,j = 1,\ldots I_Q$ using the quantity $\varepsilon = 1\times 10^{-10}$, as follows:

$$\overline{\varsigma}_{ij}^{(1)} = \begin{cases} \dfrac{\overline{x}_i - \varepsilon}{\overline{x}_j - \varepsilon}\widetilde{\varsigma}_{ij}^{(1)} & i \neq j \\ \dfrac{1}{\overline{x}_i - \varepsilon} + \widetilde{\varsigma}_{ij}^{(1)} & i = j \end{cases} \tag{78}$$

These coefficients are collected into the matrix $\overline{\varsigma}^{(1)}$. Following a similar approach as in Eq. (74), the GIQ numerical technique approximates the integral of an arbitrary function $f = f(x)$ over a closed interval $[x_i, x_j] \subseteq [a,b]$ as a linear combination of its values $f(x_k)$ at the discrete points x_k, where $k = 1,\ldots,I_Q$:

$$\int_{x_i}^{x_j} f(x)dx = \sum_{k=1}^{I_Q} \widetilde{w}_k^{ij} f(x_k) = \sum_{k=1}^{I_Q}(w_{jk} - w_{ik}) f(x_k) \tag{79}$$

Here, $\widetilde{w}_k^{ij}$ are the weighting coefficients for the integral over the interval $[a,b]$. These coefficients are evaluated from those, denoted by w_{ik}, w_{jk}, associated with the intervals $[a,x_i] \subseteq [a,b]$ and $[a,x_j] \subseteq [a,b]$. They are collected into the GIQ matrix $\mathbf{W}$, whose size is $I_Q \times I_Q$, which is defined as the inverse of the matrix $\overline{\varsigma}^{(1)}$:

$$\mathbf{W} = \left(\overline{\varsigma}^{(1)}\right)^{-1} \tag{80}$$

In this way, the GIQ terms w_{ik}, w_{jk} with $k = 1,\ldots,I_Q$ represent the i-th and the j-th rows, respectively, of matrix $\mathbf{W}$. Finally, the integral of function f over the closed interval $[a,b]$ is computed as follows:

$$\int_a^b f(x)dx = \sum_{k=1}^{I_Q} w_k^{1I_Q} f(x_k) \tag{81}$$

The assembled form of Eq. (73) is, then, obtained by introducing the column vector $\boldsymbol{\delta}$ of size $(3(N+2)I_N I_M)\times 1$, which collects the values of the unknown variables at the points of the discrete computational grid of size $I_N \times I_M$:

$$\boldsymbol{K\delta} = \omega^2 \boldsymbol{M\delta} \Leftrightarrow \begin{bmatrix} \mathbf{K}_{bb} & \mathbf{K}_{bd} \\ \mathbf{K}_{db} & \mathbf{K}_{dd} \end{bmatrix} \begin{bmatrix} \boldsymbol{\delta}_b \\ \boldsymbol{\delta}_d \end{bmatrix} = \omega^2 \begin{bmatrix} \mathbf{0} & \mathbf{0} \\ \mathbf{0} & \mathbf{M}_{dd} \end{bmatrix} \begin{bmatrix} \boldsymbol{\delta}_b \\ \boldsymbol{\delta}_d \end{bmatrix} \tag{82}$$

In Eq. (82), vector $\boldsymbol{\delta} = [\,\boldsymbol{\delta}_b \quad \boldsymbol{\delta}_d\,]^T$ is arranged by means of vectors $\boldsymbol{\delta}_b$ and $\boldsymbol{\delta}_d$, which contain the unknown DOFs associated with the nodes on the boundary and those ones located in the inner part of the grid, respectively. By performing a static condensation of Eq. (82), the discrete governing equations can be expressed in a more efficient form as follows, with $\mathbf{I}$ representing the identity matrix:

$$\left(\mathbf{M}_{dd}^{-1}\left(\mathbf{K}_{dd} - \mathbf{K}_{db}\mathbf{K}_{bb}^{-1}\mathbf{K}_{bd}\right) - \omega^2\mathbf{I}\right)\boldsymbol{\delta}_d = \mathbf{0} \tag{83}$$

4. Applications and results

In this section, the generalized ESL formulation, based on geometric principal coordinates, is used to investigate the dynamic behaviour of arbitrarily-shaped structures with bi-connected geometries, as well as holes and discontinuities. A systematic set of numerical studies is presented, applying the present theoretical formulation, based on higher-order theories, in order to analyse the dynamic behaviour of laminated anisotropic doubly-curved shell structures of arbitrary shape, with bi-connected domain and geometric discontinuities such as holes and cracks. For each case study, a FEM-based 3D solution is used as reference solution for validation purposes. Structures with various curvatures and lamination schemes are analysed, considering both orthotropic and anisotropic materials within the laminates. In particular, the numerical investigations reported in this section use graphite-epoxy and glass-epoxy as orthotropic layers, while a triclinic material is used for the generally anisotropic lamina. The mechanical properties of graphite-epoxy, with density $\rho = 1450\,\mathrm{kg/m^3}$, are provided below in terms of elastic moduli E_1, E_2, E_3, shear moduli G_{12}, G_{13}, G_{23}, and Poisson's coefficients $\nu_{12}, \nu_{13}, \nu_{23}$:

$$\begin{aligned} &E_1 = 137.9 \times 10^9\,\mathrm{N/m^2}, \quad E_2 = E_3 = 8.96 \times 10^9\,\mathrm{N/m^2} \\ &G_{12} = G_{13} = 7.1 \times 10^9\,\mathrm{N/m^2}, \quad G_{23} = 6.2 \times 10^9\,\mathrm{N/m^2} \\ &\nu_{12} = \nu_{13} = 0.3, \quad \nu_{23} = 0.49 \end{aligned} \tag{84}$$

On the other hand, the engineering constants of the glass-epoxy ($\rho = 1900\,\mathrm{kg/m^3}$) take the following values:

$$\begin{aligned} &E_1 = 53.78 \times 10^9\,\mathrm{N/m^2}, \quad E_2 = E_3 = 17.93 \times 10^9\,\mathrm{N/m^2} \\ &G_{12} = G_{13} = 8.96 \times 10^9\,\mathrm{N/m^2}, \quad G_{23} = 3.45 \times 10^9\,\mathrm{N/m^2} \\ &\nu_{12} = \nu_{13} = 0.25, \quad \nu_{23} = 0.34 \end{aligned} \tag{85}$$

The corresponding components $C_{ij} = E_{ij}$ of the 3D constitutive matrix in Eq. (32) are derived from the procedure extensively outlined in Ref. [69]. Finally, the mechanical properties of the triclinic material, with density $\rho = 7750\,\mathrm{kg/m^3}$, are presented below with respect to the material reference system:

$$\begin{bmatrix} C_{11} & C_{12} & C_{16} & C_{14} & C_{15} & C_{13} \\ C_{12} & C_{22} & C_{26} & C_{24} & C_{25} & C_{23} \\ C_{16} & C_{26} & C_{66} & C_{46} & C_{56} & C_{36} \\ C_{14} & C_{24} & C_{46} & C_{44} & C_{45} & C_{34} \\ C_{15} & C_{25} & C_{56} & C_{45} & C_{55} & C_{35} \\ C_{13} & C_{23} & C_{36} & C_{34} & C_{35} & C_{33} \end{bmatrix} = \begin{bmatrix} 98.84 & 53.92 & 0.03 & 1.05 & -0.1 & 50.78 \\ 53.92 & 99.19 & 0.03 & 0.55 & -0.18 & 50.87 \\ 0.03 & 0.03 & 22.55 & -0.04 & 0.25 & 0.02 \\ 1.05 & 0.55 & -0.04 & 21.1 & 0.07 & 1.03 \\ -0.1 & -0.18 & 0.25 & 0.07 & 21.14 & -0.18 \\ 50.78 & 50.87 & 0.02 & 1.03 & -0.18 & 87.23 \end{bmatrix} \times 10^9\,\mathrm{N/m^2} \tag{86}$$

The introduction of holes within the rectangular physical domain is defined by the point $(\overline{\alpha}_1^{(d)}, \overline{\alpha}_2^{(d)})$ with $d = 1,\ldots,\overline{d}$, where $\overline{d}$ denotes the total number of holes within the structure. As illustrated in Fig. 2, this point specifies the location of the hole within the rectangular domain. To simplify the notation, when $\overline{d} = 1$, the positions $(\overline{\alpha}_1^{(d)}, \overline{\alpha}_2^{(d)}) = (\overline{\alpha}_1, \overline{\alpha}_2)$ are used to specify the position and size of the hole.

It should be noted that in the previous works from literature, the ESL formulation was applied to arbitrarily-shaped structures characterized by a single domain, which was mapped into a rectangular computational domain using NURBS-based blending functions. In the present work, the implementation of the theory enables the derivation of the numerical solution of the dynamic governing equations over an arbitrary physical domain using a finite element approximation. To achieve this, the Weak Form PDE interface is used, located within the mathematics module of the software, considering a 2D space dimension. A 2D geometry is here introduced, which represents the domain where the principal coordinates α_1, α_2 are defined. The 2D domain is discretized with a rectangular or triangular mesh, where the number of nodes along each edge has been properly assigned. Then, the geometry of the shell is modelled in the parametric domain starting from the position vector equation of the reference surface $\mathbf{r}(\alpha_1, \alpha_2)$ as in Eq. (2), along with differential geometry quantities, including the Lamé parameters (3), the principal radii of curvature (4), and the outward normal unit vector from Eq. (5). In addition, the analytical expressions of the partial derivatives of these functions are provided. Then, the higher-order definition equations, already introduced in Eq. (29), are used to define the generalized strains collected within the vector $\boldsymbol{\varepsilon}^{(\tau)\alpha_i}$, for each $\tau = 0,\ldots,N+1$. The governing equations are obtained by the software starting from the computation in extended form of all the energy contributions as in Eq. (24), evaluated at each point of the 2D parametric domain. These energy contributions are the elastic strain energy density, denoted by ϕ, and the kinetic energy density $\mathfrak{t}$. They are defined at each point (α_1, α_2) of the parametric domain as follows:

$$\phi(\alpha_1, \alpha_2) = \frac{1}{2} \sum_{\tau=0}^{N+1} \sum_{i=1}^{3} \left(\boldsymbol{\varepsilon}^{(\tau)\alpha_i}\right)^T \mathbf{S}^{(\tau)\alpha_i} = \frac{1}{2} \sum_{\tau=0}^{N+1} \sum_{\eta=0}^{N+1} \sum_{i=1}^{3} \sum_{j=1}^{3} \left(\boldsymbol{\varepsilon}^{(\tau)\alpha_i}\right)^T \mathbf{A}^{(\tau\eta)\alpha_i\alpha_j} \boldsymbol{\varepsilon}^{(\eta)\alpha_j} \tag{87}$$

$$\mathfrak{t}(\alpha_1, \alpha_2) = \frac{1}{2} \sum_{\tau=0}^{N+1} \sum_{\eta=0}^{N+1} \left(\dot{\mathbf{u}}^{(\tau)}\right)^T \mathbf{M}^{(\tau\eta)} \dot{\mathbf{u}}^{(\eta)} \tag{88}$$

The evaluation of the elastic strain energy density $\overline{\Phi}$ of Eq. (87) is conducted by neglecting the effect of curvature in the higher-order constitutive matrix $\mathbf{A}^{(\tau\eta)\alpha_i\alpha_j}$ according to Eq. (44), and the expression reported in Eq. (43) is used to compute the quantities $A_{nm\,(pq)}^{(\tau\eta)[fg]\alpha_i\alpha_j}$, with $p = q = 1$. The quantities ϕ and $\mathfrak{t}$ are related to the virtual variations $\delta\Phi$ and δT of the energy contributions already defined in Eqs. (37) and (48), respectively, as follows:

$$\delta\Phi = \int_{\alpha_1}\int_{\alpha_2} \delta\phi(\alpha_1, \alpha_2) A_1 A_2 d\alpha_1 d\alpha_2 \tag{89}$$

$$\delta T = \int_{\alpha_1}\int_{\alpha_2} \delta\mathfrak{t}(\alpha_1, \alpha_2) A_1 A_2 d\alpha_1 d\alpha_2 \tag{90}$$

The virtual variations $\delta\Phi$ and δT are, then, written within the Weak form PDE module to automatically derive the weak form of the governing equations of the problem under consideration. It should be noted that the integrals occurring in Eqs. (89) and (90) accounts also for the distribution of the Lamé parameters A_1, A_2 at each point of the domain. As a consequence, the quantities $\delta\phi$ and $\delta\mathfrak{t}$ are conveniently multiplied by $A_1 A_2$ when introducing the virtual variation of the energy contributions within the software for a correct evaluation of these integrals. Finally, the boundary conditions of the governing equations are modelled in the software by using the Dirichlet boundary condition module, and the modal analysis of the structure is finally carried out to determine the natural frequencies. Once the virtual variations of all energy contributions are correctly provided, the software automatically discretizes the fundamental equations and provides a finite element

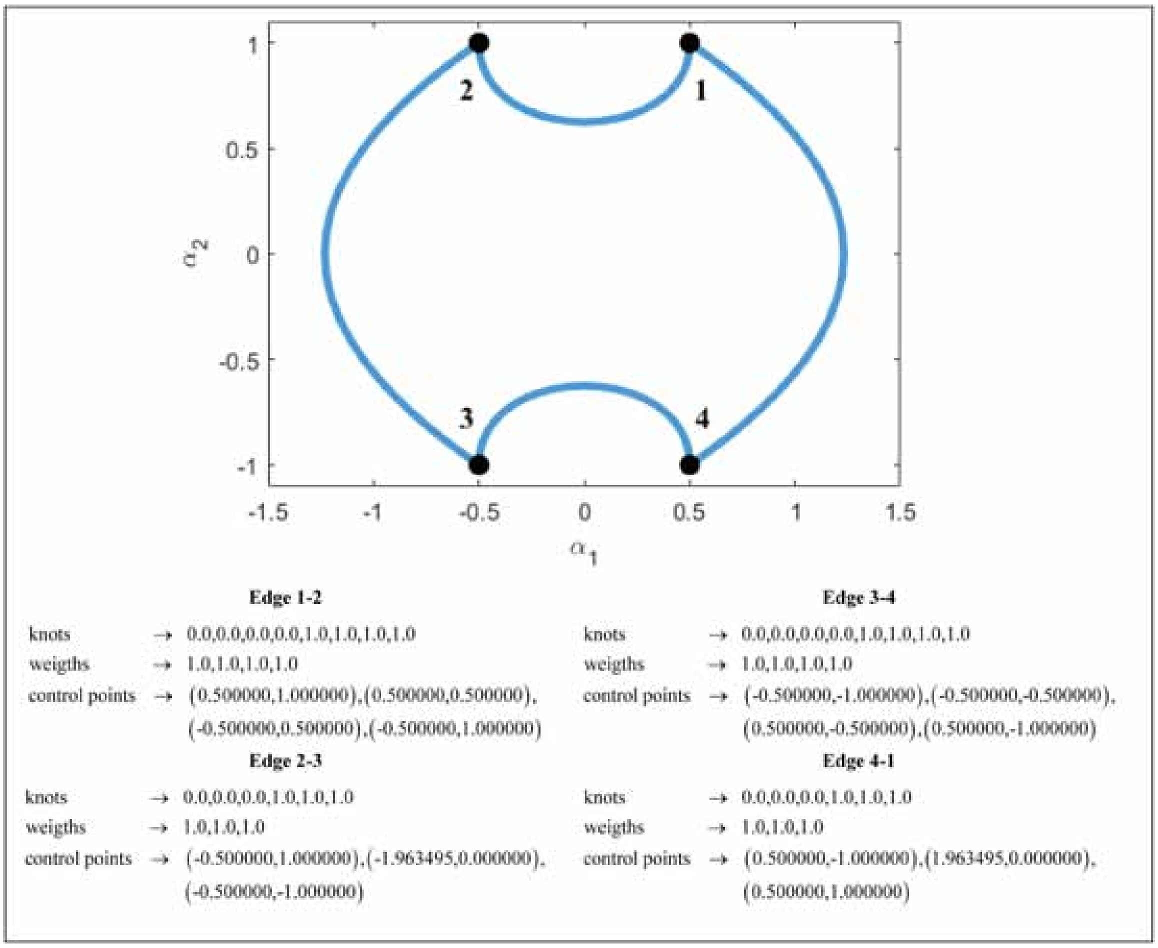

Edge 1-2

knots → 0.0,0.0,0.0,0.0,1.0,1.0,1.0,1.0
weigths → 1.0,1.0,1.0,1.0
control points → (0.500000,1.000000),(0.500000,0.500000),
(-0.500000,0.500000),(-0.500000,1.000000)

Edge 2-3

knots → 0.0,0.0,0.0,1.0,1.0,1.0
weigths → 1.0,1.0,1.0
control points → (-0.500000,1.000000),(-1.963495,0.000000),
(-0.500000,-1.000000)

Edge 3-4

knots → 0.0,0.0,0.0,0.0,1.0,1.0,1.0,1.0
weigths → 1.0,1.0,1.0,1.0
control points → (-0.500000,-1.000000),(-0.500000,-0.500000),
(0.500000,-0.500000),(0.500000,-1.000000)

Edge 4-1

knots → 0.0,0.0,0.0,1.0,1.0,1.0
weigths → 1.0,1.0,1.0
control points → (0.500000,-1.000000),(1.963495,0.000000),
(0.500000,1.000000)

Fig. 3. Distortion of the rectangular physical domain using NURBS description of the boundary edges. Representation of the distorted domain and details on knots, weights, and control points of each edge.

solution with shape functions selected by the user. The shape functions used herein are based on various polynomials of different orders. In this work, the attention is focused on Lagrange and Hermite polynomials. When Lagrange polynomials are used, the continuity of the unknown variables is ensured between adjacent elements. However, the smoothness of the function across the entire parametric domain is not guaranteed. In other words, the solution has C^0 continuity but not higher-order smoothness. On the contrary, the Hermite interpolation functions ensure the continuity of derivatives between adjacent elements, providing a higher level of accuracy with a lower computational effort compared to Lagrange polynomials. It is important to note that, to the best of our knowledge, the discretization of the domain does not directly embed curved edges of each element, but rather it adopts a linear or parabolic discretization of the geometric boundaries. Two or more nodes are then introduced along each edge of the finite element, and polynomial approximation is applied to interpolate the numerical solution. Unlike the GDQ-based weak formulation of the problem, which usually uses a computational grid based on the roots of the Legendre polynomials, the 2D finite element implementation accounts for a uniform node distribution. More specifically, when Lagrange shape functions are adopted, a rectangular grid is defined with evenly spaced computational nodes. Similarly, in the case of triangular finite elements, a regular triangular grid is defined, and the node locations are determined by areal coordinates. On the other hand, when Hermite polynomials are used, the same discretization is applied as with Lagrange rectangular and triangular elements, with the exception of the points on the edges of elements adjacent to the corners, which are not included in the grid. Therefore, additional DOFs are introduced at each corner in the Hermite interpolation with respect to the Lagrange case, which consists in the first-order derivative of the unknown function. Second-order mixed derivatives, typical of Hermite 2D interpolation, are replaced by DOFs associated with the inner points of the element. The actual distribution of nodes within Lagrange and Hermite elements of various orders is shown for both rectangular and triangular elements in Fig. 1. If first-order derivatives are associated with a corner node, a different symbol is used to identify the node in hand. Each element in the figure is based on the 2D polynomial approximation of the unknown variable, here denoted in general as $u(\xi_1, \xi_2)$. A finite element interpolation of the arbitrary unknown variable $u(\xi_1, \xi_2)$ is performed. When Lagrange polynomials are adopted, the values $\overline{u}_i$ for $i = 1, \ldots, \widetilde{N}$ of the unknown variables are interpolated within the computational domain using the shape functions $N_i(\xi_1, \xi_2)$. If $\widetilde{N}$ denotes the total number of points along each finite element boundary, the 2D Lagrange interpolation for a rectangular domain is expressed as:

$$u(\xi_1, \xi_2) = \sum_{i=1}^{\widetilde{N}^2} N_i(\xi_1, \xi_2)\overline{u}_i \tag{91}$$

Similarly, the following relation is adopted for 2D interpolation within a triangular element using Lagrange polynomials:

$$u(\xi_1, \xi_2) = \sum_{i=1}^{\widetilde{N}(\widetilde{N}+1)/2} N_i(\xi_1, \xi_2)\overline{u}_i \tag{92}$$

When Hermite polynomials are employed to interpolate the unknown function $u(\xi_1, \xi_2)$, the associated DOFs are given by the values $\widetilde{u}_i$

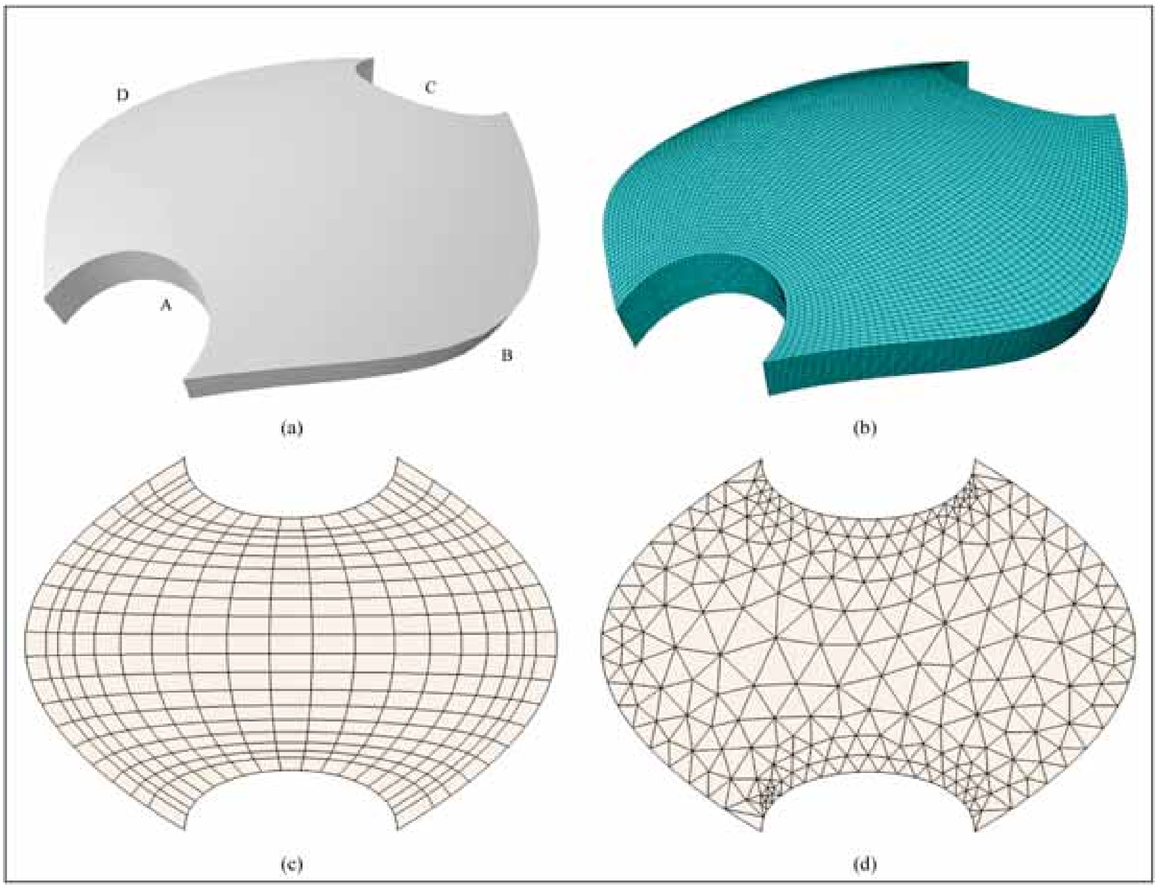

Fig. 4. Geometric model (a) and 3D FEM discretization (b) of a laminated elliptic paraboloid of arbitrary shape made of anisotropic materials. Finite element discretization of the 2D physical domain using rectangular elements (c) and triangular elements (d) for the application of higher-order theories.

for $i = 1,\ldots,\widetilde{N}-8$, assumed by u at the discrete points, similar to the case of Lagrange interpolation. However, for those points adjacent to the corners of the computational elements, these DOFs are replaced by the partial derivatives of the unknown function along ξ_1 and ξ_2 directions, denoted by $\widetilde{u}_{i,\xi_1}$ and $\widetilde{u}_{i,\xi_2}$, respectively, evaluated at the corners of the element. In this way, the Hermite finite element interpolation for a 2D rectangular element with $\widetilde{N}$ nodes along its edges is formulated as follows:

$$\begin{aligned} u(\xi_1,\xi_2) &= \sum_{i=1}^{\tilde{N}^2} N_i(\xi_1,\xi_2)\overline{u}_i \\ &= \sum_{i=1}^{\tilde{N}^2-8} N_i(\xi_1,\xi_2)\widetilde{u}_i + \sum_{i=1}^{4} N_{\tilde{N}^2-8+i}(\xi_1,\xi_2)\widetilde{u}_{i,\xi_1} \\ &\quad + \sum_{i=1}^{4} N_{\tilde{N}^2-4+i}(\xi_1,\xi_2)\widetilde{u}_{i,\xi_2} \end{aligned} \tag{93}$$

In the case of triangular Hermite elements with $\widetilde{N}$ nodes along each boundary, the interpolation of the unknown function $u(\xi_1,\xi_2)$ becomes:

$$\begin{aligned} u(\xi_1,\xi_2) &= \sum_{i=1}^{\tilde{N}(\tilde{N}+1)/2} N_i(\xi_1,\xi_2)\overline{u}_i \\ &= \sum_{i=1}^{\tilde{N}(\tilde{N}+1)/2-6} N_i(\xi_1,\xi_2)\widetilde{u}_i + \sum_{i=1}^{3} N_{(\tilde{N}(\tilde{N}+1)/2)-6+i}(\xi_1,\xi_2)\widetilde{u}_{i,\xi_1} \\ &\quad + \sum_{i=1}^{3} N_{(\tilde{N}(\tilde{N}+1)/2)-3+i}(\xi_1,\xi_2)\widetilde{u}_{i,\xi_2} \end{aligned} \tag{94}$$

For the sake of clarity, in the case of $\widetilde{N} = 4$, the Lagrange interpolation given in Eq. (91) for a rectangular element takes the following form:

$$\begin{aligned} u(\xi_1,\xi_2) &= \sum_{i=1}^{16} N_i(\xi_1,\xi_2)\overline{u}_i = \\ &= N_1(\xi_1,\xi_2)\overline{u}_1 + N_2(\xi_1,\xi_2)\overline{u}_2 + N_3(\xi_1,\xi_2)\overline{u}_3 + N_4(\xi_1,\xi_2)\overline{u}_4 + N_5(\xi_1,\xi_2)\overline{u}_5 + N_6(\xi_1,\xi_2)\overline{u}_6 + \\ &\quad + N_7(\xi_1,\xi_2)\overline{u}_7 + N_8(\xi_1,\xi_2)\overline{u}_8 + N_9(\xi_1,\xi_2)\overline{u}_9 + N_{10}(\xi_1,\xi_2)\overline{u}_{10} + N_{11}(\xi_1,\xi_2)\overline{u}_{11} + N_{12}(\xi_1,\xi_2)\overline{u}_{12} + \\ &\quad + N_{13}(\xi_1,\xi_2)\overline{u}_{13} + N_{14}(\xi_1,\xi_2)\overline{u}_{14} + N_{15}(\xi_1,\xi_2)\overline{u}_{15} + N_{16}(\xi_1,\xi_2)\overline{u}_{16} \end{aligned} \tag{95}$$

The expression in Eq. (95) is applied using parabolic shape functions, based on a rectangular grid of nodes with size $\widetilde{N} \times \widetilde{N} = 4 \times 4$. On the other hand, when Hermite interpolation from Eq. (93) is used, the following relation is obtained, replacing Eq. (95):

$$\begin{aligned} u(\xi_1,\xi_2) &= \sum_{i=1}^{16} N_i(\xi_1,\xi_2)\overline{u}_i = \sum_{i=1}^{16-8} N_i(\xi_1,\xi_2)\widetilde{u}_i + \sum_{i=1}^{4} N_{16-8+i}(\xi_1,\xi_2)\widetilde{u}_{i,\xi_1} + \sum_{i=1}^{4} N_{16-4+i}(\xi_1,\xi_2)\widetilde{u}_{i,\xi_2} = \\ &= N_1(\xi_1,\xi_2)\widetilde{u}_1 + N_2(\xi_1,\xi_2)\widetilde{u}_2 + N_3(\xi_1,\xi_2)\widetilde{u}_3 + N_4(\xi_1,\xi_2)\widetilde{u}_4 + N_5(\xi_1,\xi_2)\widetilde{u}_5 + N_6(\xi_1,\xi_2)\widetilde{u}_6 + \\ &+ N_7(\xi_1,\xi_2)\widetilde{u}_7 + N_8(\xi_1,\xi_2)\widetilde{u}_8 + N_9(\xi_1,\xi_2)\widetilde{u}_{1,\xi_1} + N_{10}(\xi_1,\xi_2)\widetilde{u}_{2,\xi_1} + N_{11}(\xi_1,\xi_2)\widetilde{u}_{3,\xi_1} + N_{12}(\xi_1,\xi_2)\widetilde{u}_{4,\xi_1} + \\ &+ N_{13}(\xi_1,\xi_2)\widetilde{u}_{1,\xi_2} + N_{14}(\xi_1,\xi_2)\widetilde{u}_{2,\xi_2} + N_{15}(\xi_1,\xi_2)\widetilde{u}_{3,\xi_2} + N_{16}(\xi_1,\xi_2)\widetilde{u}_{4,\xi_2} \end{aligned} \tag{96}$$

For triangular elements with $\widetilde{N} = 4$ nodes along each edge, using Lagrange shape functions, the following finite element interpolation is applied:

$$\begin{aligned} u(\xi_1,\xi_2) &= \sum_{i=1}^{10} N_i(\xi_1,\xi_2)\overline{u}_i = \\ &= N_1(\xi_1,\xi_2)\overline{u}_1 + N_2(\xi_1,\xi_2)\overline{u}_2 + N_3(\xi_1,\xi_2)\overline{u}_3 + N_4(\xi_1,\xi_2)\overline{u}_4 + N_5(\xi_1,\xi_2)\overline{u}_5 + N_6(\xi_1,\xi_2)\overline{u}_6 + \\ &+ N_7(\xi_1,\xi_2)\overline{u}_7 + N_8(\xi_1,\xi_2)\overline{u}_8 + N_9(\xi_1,\xi_2)\overline{u}_9 + N_{10}(\xi_1,\xi_2)\overline{u}_{10} \end{aligned} \tag{97}$$

Similarly, in the case of Hermite interpolation functions on triangular elements with $\widetilde{N} = 4$, Eq. (94) is expressed in its expanded form as:

$$\begin{aligned} u(\xi_1,\xi_2) &= \sum_{i=1}^{10} N_i(\xi_1,\xi_2)\overline{u}_i = \sum_{i=1}^{10-6} N_i(\xi_1,\xi_2)\widetilde{u}_i + \sum_{i=1}^{3} N_{10-6+i}(\xi_1,\xi_2)\widetilde{u}_{i,\xi_1} + \sum_{i=1}^{3} N_{10-3+i}(\xi_1,\xi_2)\widetilde{u}_{i,\xi_2} = \\ &= N_1(\xi_1,\xi_2)\widetilde{u}_1 + N_2(\xi_1,\xi_2)\widetilde{u}_2 + N_3(\xi_1,\xi_2)\widetilde{u}_3 + N_4(\xi_1,\xi_2)\widetilde{u}_4 + \\ &+ N_5(\xi_1,\xi_2)\widetilde{u}_{1,\xi_1} + N_6(\xi_1,\xi_2)\widetilde{u}_{2,\xi_1} + N_7(\xi_1,\xi_2)\widetilde{u}_{3,\xi_1} + N_8(\xi_1,\xi_2)\widetilde{u}_{1,\xi_2} + N_9(\xi_1,\xi_2)\widetilde{u}_{2,\xi_2} + N_{10}(\xi_1,\xi_2)\widetilde{u}_{3,\xi_2} \end{aligned} \tag{98}$$

When the GDQ-based implementation is adopted, the fundamental governing equations are solved directly in their strong form, yielding a smooth solution across the parametric domain. However, the strong-form GDQ solution is only valid when a rectangular computational grid can be defined. For bi-connected domains, this strategy cannot be applied. In contrast, the 2D FEM solution developed is derived in a weak form, for any type of 2D parametric domain, including those associated with doubly-curved shells with holes and discontinuities.

The numerical implementation of the governing equations relies on certain assumptions in the generalized constitutive relation of Eq. (39). More specifically, the higher-order constitutive coefficients $A_{nm\,(pq)}^{(\tau\eta)[fg]\alpha_i\alpha_j}$, as evaluated from Eq. (41), are assumed to be uniform across the entire parametric domain. As a result, their dependence on the curvature radii of the shell is neglected, in accordance with Eq. (43), and the material is assumed to have uniform mechanical properties in the overall structure. In addition, no variations in thickness are considered, as the integrals occurring in Eq. (43) are solved numerically using the GIQ method. Therefore, an analytical expression describing the dependence of $A_{nm\,(pq)}^{(\tau\eta)[fg]\alpha_i\alpha_j}$ on the geometric curvilinear coordinates α_1, α_2 is not available.

A preliminary investigation is presented to assess the accuracy of the current 2D FEM model in evaluating the vibrational response of shell structures characterized by singly-connected domains. To this end, an elliptic paraboloid of arbitrary shape is considered. The physical domain of this structure is distorted using the NURBS-based blending functions described in Eqs. (55) and (56), along with the information provided in Fig. 3, which includes knots, weights, and control points. The reference surface equation of the selected shell, which belongs to the class of translational surfaces, is expressed in curvilinear principal coordinates α_1, α_2 as follows [69]:

$$\begin{aligned} \mathbf{r}(\alpha_1,\alpha_2) = &\left(\frac{k^{\alpha_1}\tan\alpha_1}{2} - \frac{k^{\alpha_2}\tan^2\alpha_2}{4}\sin\alpha_1\right)\mathbf{e}_1 - \frac{k^{\alpha_2}\tan\alpha_2}{2}\mathbf{e}_2 \\ &+ \left(\frac{k^{\alpha_1}\tan^2\alpha_1}{4} + \frac{k^{\alpha_2}\tan^2\alpha_2}{4}\cos\alpha_1\right)\mathbf{e}_3 \end{aligned} \tag{99}$$

Here, $k^{\alpha_1} = 2$ and $k^{\alpha_2} = 3$ represent the characteristic parameters of the curves along α_1 and α_2, respectively. These curves correspond to the generatrix and directrix of the translational surface. The distorted domain is shown in Fig. 3, along with the NURBS description of the curved edges of the physical domain. The lamination scheme consists of three layers with thicknesses $h_1 = 0.03\,\mathrm{m}$, $h_2 = 0.04\,\mathrm{m}$, and $h_3 = 0.02\,\mathrm{m}$ and orientations $(35/20/75)$. In particular, the two external laminae are made of graphite-epoxy (84), while the central core is composed of triclinic material (86). The first ten natural frequencies are computed under two different boundary conditions. In the “boundary conditions 1” configuration, the structure is clamped only at the lateral surface denoted by “B”. In contrast, “boundary conditions 2” involves clamping the lateral surfaces denoted as “A” and “C”. In this work, the clamped boundary conditions along a specific boundary edge of the 2D physical

Table 1
First ten natural frequencies of an elliptic paraboloid of arbitrary shape employing the EDZ4 kinematic model. The results are derived with both rectangular and triangular mesh by using Lagrange and Hermite polynomials of various orders, while the reference solution is obtained from 3D FEM and 2D GDQ strong and weak formulations.

	DOFs	f_1 [Hz]	f_2 [Hz]	f_3 [Hz]	f_4 [Hz]	f_5 [Hz]	f_6 [Hz]	f_7 [Hz]	f_8 [Hz]	f_9 [Hz]	f_{10} [Hz]
FFFC											
3D FEM	1426461	68.95	142.37	321.60	395.48	486.92	644.87	811.44	852.97	989.03	1062.61
EDZ4	15138	69.22	142.10	323.10	398.15	490.44	647.95	816.86	858.42	993.71	1067.12
EDZ4 (W)	15138	69.27	142.67	324.10	399.78	492.85	650.92	821.35	861.48	998.13	1070.31
Rectangular mesh											
L-1	7200	77.04	152.09	348.54	418.55	515.64	690.29	868.08	901.52	1056.12	1091.28
L-2	27378	69.17	142.20	322.99	398.80	490.65	648.02	816.79	858.82	994.87	1067.59
L-3	60552	69.11	142.02	322.66	398.44	490.29	647.51	816.14	858.25	994.12	1067.09
L-4	106722	69.10	142.00	322.62	398.38	490.24	647.46	816.07	858.18	994.06	1067.01
L-5	165888	69.10	142.00	322.62	398.37	490.24	647.46	816.06	858.17	994.05	1067.00
L-6	238050	69.09	142.00	322.61	398.37	490.23	647.45	816.06	858.16	994.05	1067.00
L-7	323208	69.09	142.00	322.61	398.37	490.23	647.45	816.06	858.16	994.05	1066.99
H-3	47592	69.19	142.18	323.12	399.06	490.86	647.78	816.76	859.34	995.21	1067.94
H-4	93762	69.12	142.04	322.74	398.52	490.40	647.53	816.24	858.47	994.34	1067.24
H-5	152928	69.10	142.00	322.64	398.38	490.29	647.47	816.12	858.25	994.12	1067.06
H-6	225090	69.09	142.00	322.61	398.37	490.23	647.45	816.06	858.16	994.05	1067.00
H-7	310248	69.10	142.00	322.63	398.38	490.25	647.46	816.08	858.20	994.08	1067.02
Triangular mesh											
L-1	5778	82.50	181.50	368.95	439.51	554.16	726.02	907.27	948.32	1100.12	1154.93
L-2	21690	69.18	142.20	323.05	399.10	490.85	648.07	817.21	859.24	995.60	1067.85
L-3	47754	69.11	142.02	322.66	398.47	490.31	647.50	816.14	858.29	994.14	1067.10
L-4	83970	69.10	142.00	322.62	398.39	490.25	647.46	816.07	858.19	994.06	1067.02
L-5	130338	69.10	142.00	322.62	398.37	490.24	647.46	816.06	858.17	994.05	1067.00
L-6	186858	69.09	142.00	322.61	398.37	490.23	647.45	816.06	858.17	994.05	1067.00
L-7	253530	69.09	142.00	322.61	398.37	490.23	647.45	816.06	858.16	994.05	1066.99
H-3	27486	69.51	142.70	324.54	401.41	492.26	648.73	818.33	862.68	998.41	1070.50
H-4	63702	69.21	142.19	323.17	399.17	490.85	647.79	816.73	859.51	995.32	1067.98
H-5	110070	69.11	142.01	322.71	398.44	490.42	647.50	816.25	858.45	994.30	1067.21
H-6	166590	69.09	142.00	322.61	398.37	490.23	647.45	816.06	858.17	994.05	1067.00
H-7	233262	69.11	142.02	322.67	398.46	490.30	647.49	816.13	858.31	994.19	1067.10
CFCF											
3D FEM	1426461	221.84	251.68	532.75	538.83	639.45	871.74	975.22	1030.32	1074.46	1185.70
EDZ4	15138	223.50	253.40	536.08	542.38	642.39	875.40	980.60	1037.08	1080.21	1191.92
EDZ4 (W)	15138	223.41	253.38	537.31	543.41	643.15	877.24	981.23	1041.34	1083.85	1194.27
Rectangular mesh											
L-1	7200	245.15	276.22	598.81	600.46	674.45	934.85	1011.39	1159.56	1182.68	1251.95
L-2	27378	223.15	252.95	536.65	542.86	642.53	875.32	981.17	1039.92	1082.44	1193.33
L-3	60552	222.76	252.63	535.47	541.63	642.02	874.45	980.34	1037.34	1080.33	1192.15
L-4	106722	222.70	252.59	535.28	541.43	641.96	874.36	980.23	1036.97	1080.03	1192.00
L-5	165888	222.69	252.58	535.24	541.39	641.95	874.34	980.21	1036.91	1079.98	1191.97
L-6	238050	222.69	252.58	535.23	541.39	641.94	874.34	980.20	1036.89	1079.97	1191.96
L-7	323208	222.69	252.58	535.23	541.38	641.94	874.34	980.20	1036.89	1079.96	1191.96
H-3	47592	226.88	255.73	543.51	550.12	647.52	882.62	991.15	1051.79	1092.51	1202.51
H-4	93762	224.42	253.87	538.51	544.84	644.16	877.82	984.60	1042.90	1084.87	1195.95
H-5	152928	223.41	253.11	536.51	542.74	642.97	875.91	982.20	1039.14	1081.78	1193.61
H-6	225090	222.69	252.58	535.23	541.39	641.94	874.34	980.20	1036.89	1079.97	1191.96
H-7	310248	222.95	252.77	535.69	541.86	642.27	874.86	980.82	1037.74	1080.64	1192.53
Triangular mesh											
L-1	5778	256.90	286.18	630.33	635.76	706.38	946.30	1028.14	1224.35	1260.91	1316.51
L-2	21690	223.03	252.88	536.23	542.34	642.78	875.28	981.07	1039.44	1082.18	1194.02
L-3	47754	222.72	252.61	535.32	541.47	642.02	874.39	980.27	1037.09	1080.13	1192.10
L-4	83970	222.69	252.59	535.24	541.40	641.96	874.34	980.21	1036.91	1079.99	1191.98
L-5	130338	222.69	252.58	535.23	541.38	641.95	874.34	980.20	1036.89	1079.97	1191.96
L-6	186858	222.69	252.58	535.23	541.38	641.94	874.34	980.20	1036.89	1079.96	1191.96
L-7	253530	222.69	252.58	535.23	541.38	641.94	874.34	980.20	1036.89	1079.96	1191.96
H-3	27486	225.70	254.95	540.31	546.93	648.51	881.15	993.28	1045.52	1088.20	1204.29
H-4	63702	223.83	253.45	537.01	543.33	644.42	877.06	985.72	1039.90	1082.83	1196.35
H-5	110070	223.16	252.94	535.96	542.18	643.06	875.56	982.83	1038.08	1081.12	1193.86
H-6	166590	222.69	252.58	535.23	541.38	641.94	874.34	980.20	1036.89	1079.97	1191.96
H-7	233262	222.83	252.69	535.45	541.62	642.27	874.70	980.98	1037.27	1080.32	1192.51

domain mean that all generalized displacement field components are assumed to be zero. For each case, a 3D FEM solution is derived from a model consisting of 112700 parabolic brick elements and 475487 nodes, yielding a total number of 1426461 unknown variables. The 3D FEM discretization is shown for clarity in Fig. 4. In addition, the EDZ4 kinematic model is employed to derive a 2D GDQ-based solution from both the strong and the weak form equations. These solutions adopt a discrete grid of $I_N \times I_M = 31 \times 31$ sample points. The grid is based on the Chebyshev-Gauss-Lobatto distribution for strong form simulations [69], while the Legendre-Gauss-Lobatto (LGL) discretization is adopted for the weak form ones. As far as the 2D FEM model is concerned for HSDT analysis, the 2D domain is discretized with both rectangular and triangular elements assigning 19 elements along each edge of the domain.

Mode frequencies are evaluated using the present 2D HSDT FEM solution employing the EDZ4 kinematic model. The finite element implementation is carried out using both triangular and rectangular

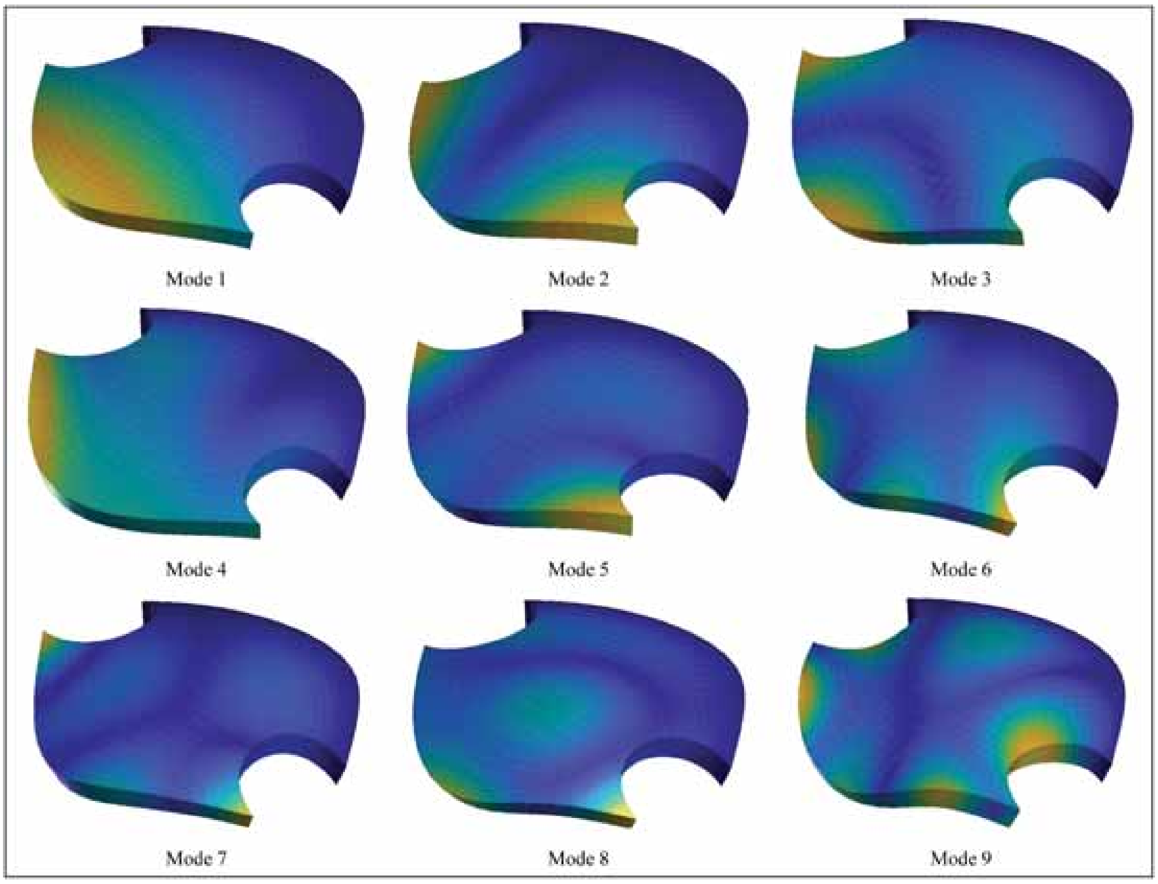

Fig. 5. First nine mode shapes of an elliptic paraboloid of arbitrary shape made of anisotropic materials. The physical domain is distorted by using NURBS-based blending functions. The representations of the vibration modes are derived from the 2D solution.

meshes, considering Lagrange and Hermite polynomials of various orders. In this way, the convergence of the first ten modes to the reference solution is checked. The results are summarized in Table 1. In particular, when Lagrange polynomials of order n are used in the analysis, the symbol $\mathrm{L}-n$ is adopted, while $\mathrm{H}-n$ refers to 2D FEM simulations with Hermite polynomials of order n. As shown in the table, the 3D FEM numerical predictions are perfectly matched when higher-order Lagrange and Hermite polynomials are used. It is worth noting that the 2D FEM analysis achieves the same level of accuracy as the 3D FEM analysis, despite involving significantly a reduced number of DOFs. Finally, a representation of the first nine mode shapes, reconstructed from the 2D solution, is provided in Fig. 5 for the first boundary conditions configuration.

Once it has been demonstrated that the higher-order 2D FEM formulation introduced in this paper can accurately predict the results from 3D FEM models for arbitrarily-shaped structures described by a rectangular distorted domain, additional examples are presented involving the application of the present finite-element approach to zero-curved, singly-curved, and doubly-curved shell structures described by arbitrary bi-connected domains. A laminated anisotropic L-shaped plate is now considered, consisting of two external layers of triclinic material (86) and a central core made of graphite-epoxy (84). The thicknesses of the layers are $h_1 = 0.01\,\mathrm{m}$, $h_2 = 3h_1$, and $h_3 = 2h_1$, while the lamination scheme is given by $(10/35/75)$. The reference surface equation is expressed in principal coordinates according to the relation provided below:

$$\mathbf{r}(\alpha_1,\alpha_2) = \mathbf{r}(x,y) = x\,\mathbf{e}_1 + y\,\mathbf{e}_2 \tag{100}$$

The geometric dimensions of the plate along the α_1 and α_2 directions are $L_1 = 0.8\,\mathrm{m}$ and $L_2 = 1.3\,\mathrm{m}$, respectively. The geometry of L-plate is obtained from that of a rectangular plate by introducing a rectangular hole with $(\overline{\alpha}_1,\overline{\alpha}_2) = (L_1/2, L_2/2)$ and length $L_1/2$ and $L_2/2$ along α_1,α_2, respectively. The structure is clamped along the edges A and F, according to the nomenclature introduced in Fig. 6. A 3D FEM model is developed to derive the reference values for the first ten natural frequencies. Then, the present higher-order ESL theory with the EDZ4 kinematic model is adopted to implement a 2D finite element model, using different shape functions and discretizations. Three different meshes are used for the analysis, as illustrated in Fig. 6. In particular, a rectangular mesh 1 exhibits a significant domain distortion, while a rectangular mesh 2 ensures regular finite elements. The rectangular mesh 1 is characterized by 40 elements along the edges D and F, and 20 elements along the other edges. Similarly, in rectangular mesh 2 and in the triangular mesh, edge F contains 40 elements, while edges A, B, and D are discretized with 20 elements. Finally, edges C and E contain 10 elements. The convergence analysis for each mesh is presented in Table 2, using Lagrange polynomials of various orders. Table 3 shows the convergence of the solution when Hermite polynomials are used. Furthermore, Fig. 7 shows the convergence of results for the first four mode frequencies when using the rectangular mesh 2 and the triangular mesh. Here, a double logarithmic representation is adopted, where the number of DOFs in each simulation is shown on the horizontal axis, and the logarithmic value of the convergence ratio e_i is shown on the vertical axis. This quantity is defined, for each i-th mode, as follows:

$$e_i = \left| \frac{f_i^{\mathrm{EDZ4}} - f_i^{\mathrm{3DFEM}}}{f_i^{\mathrm{3DFEM}}} \right| \tag{101}$$

being f_i^{3DFEM} and f_i^{EDZ4} the i-th natural frequency evaluated with the 3D FEM model and by using the EDZ4 theory in 2D FEM analysis, respec-

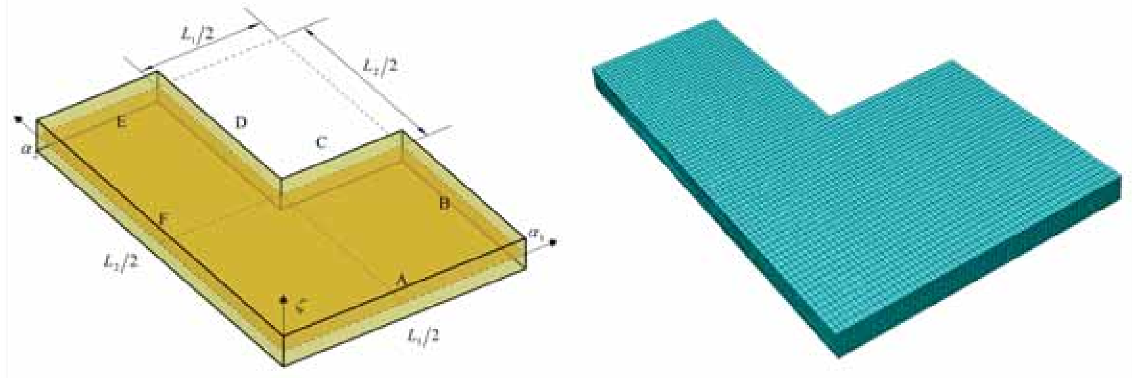

(a) Geometric model (b) 3D FEM mesh

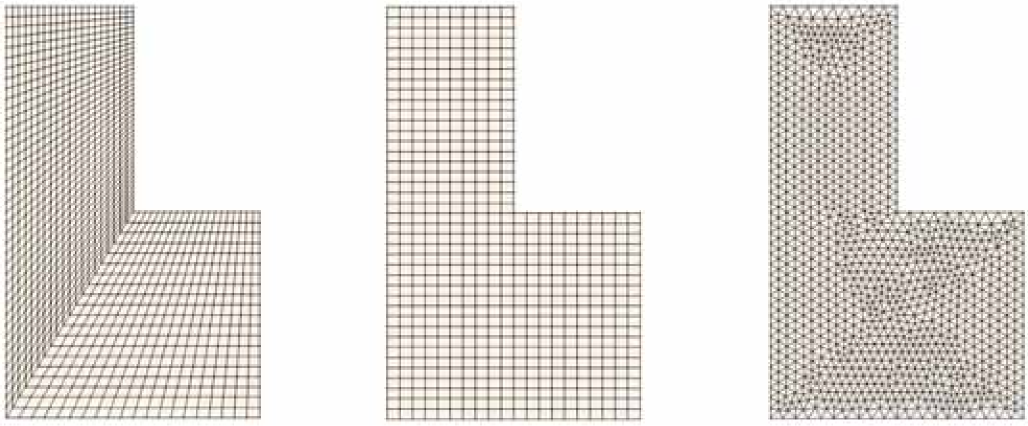

(c) (d) (e)

Fig. 6. Geometric description (a) and finite element discretization of a laminated anisotropic L-shaped plate. Representation of 3D FEM mesh (b) for the reference model, and 2D meshes adopted for higher-order theories. 2D rectangular mesh 1 (c), 2D rectangular mesh 2 (d) and 2D triangular mesh (3).

Table 2

Free vibration analysis of a laminated anisotropic L-shaped rectangular plate. Comparison with 3D FEM solutions using various 2D discretizations of the physical domain. Convergence analysis with Lagrange shape functions of different orders.

Mode f [Hz]	3D FEM		EDZ4						
	C3D8	C3D20	2D rectangular mesh 1						
Element order	1	2	1	2	3	4	5	6	7
DOFs	172854	674793	24156	91476	201996	355716	552636	792756	1076076
1	151.23	150.18	154.94	150.47	150.30	150.24	150.22	150.22	150.21
2	264.57	263.31	270.75	263.94	263.66	263.59	263.56	263.55	263.55
3	402.68	400.81	411.26	401.98	401.56	401.42	401.37	401.34	401.33
4	523.65	519.21	541.65	520.54	520.02	519.85	519.79	519.76	519.75
5	585.27	580.52	601.67	582.15	581.53	581.35	581.29	581.26	581.25
6	848.30	842.56	873.83	845.20	844.47	844.23	844.13	844.09	844.06
7	940.70	936.36	969.35	940.00	939.33	939.14	939.08	939.06	939.05
8	1107.91	1107.17	1114.68	1108.57	1107.65	1107.35	1107.23	1107.16	1107.13
9	1122.34	1113.29	1157.37	1116.84	1115.99	1115.74	1115.65	1115.61	1115.60
10	1193.38	1185.58	1226.80	1190.95	1189.79	1189.44	1189.32	1189.28	1189.27
	C3D8	C3D20	2D rectangular mesh 2						
Element order	1	2	1	2	3	4	5	6	7
DOFs	172854	674793	24156	91476	201996	355716	552636	792756	1076076
1	151.23	150.18	155.70	150.56	150.33	150.26	150.23	150.22	150.21
2	264.57	263.31	276.73	264.50	263.88	263.68	263.60	263.57	263.56
3	402.68	400.81	418.27	402.35	401.69	401.47	401.38	401.34	401.32
4	523.65	519.21	540.25	520.78	520.11	519.89	519.80	519.77	519.76
5	585.27	580.52	605.27	582.43	581.63	581.40	581.30	581.27	581.25
6	848.30	842.56	875.87	845.53	844.56	844.26	844.13	844.07	844.05
7	940.70	936.36	994.84	941.03	939.72	939.33	939.16	939.09	939.06
8	1107.91	1107.17	1113.83	1108.49	1107.57	1107.28	1107.16	1107.12	1107.09
9	1122.34	1113.29	1171.22	1117.61	1116.26	1115.87	1115.70	1115.63	1115.61

(*continued on next page*)

Table 2 (*continued*)

Mode f [Hz]	3D FEM		EDZ4						
	C3D8	C3D20	2D rectangular mesh 1						
Element order	1	2	1	2	3	4	5	6	7
DOFs	172854	674793	24156	91476	201996	355716	552636	792756	1076076
10	1193.38	1185.58	1267.43	1193.03	1190.56	1189.81	1189.48	1189.34	1189.28
	C3D8	C3D20	Triangular mesh						
Element order	1	2	1	2	3	4	5	6	7
DOFs	172854	674793	24156	91476	201996	355716	552636	792756	1076076
1	151.23	150.18	156.13	150.47	150.29	150.24	150.22	150.22	150.21
2	264.57	263.31	273.57	264.08	263.71	263.60	263.57	263.56	263.55
3	402.68	400.81	417.34	402.00	401.54	401.40	401.34	401.32	401.31
4	523.65	519.21	537.98	520.51	520.00	519.84	519.78	519.76	519.75
5	585.27	580.52	611.78	582.20	581.53	581.35	581.28	581.26	581.25
6	848.30	842.56	880.96	845.17	844.40	844.18	844.09	844.06	844.04
7	940.70	936.36	971.19	940.22	939.41	939.17	939.09	939.06	939.05
8	1107.91	1107.17	1113.48	1108.24	1107.46	1107.23	1107.15	1107.11	1107.09
9	1122.34	1113.29	1165.80	1117.00	1116.02	1115.74	1115.65	1115.61	1115.60
10	1193.38	1185.58	1233.22	1191.38	1189.93	1189.48	1189.33	1189.28	1189.26

Table 3
Free vibration analysis of a laminated anisotropic L-shaped rectangular plate. Comparison with 3D FEM solutions using various 2D discretizations of the physical domain. Convergence analysis with Hermite shape functions of different orders.

Mode f [Hz]	3D FEM						
	C3D8	C3D20	2D rectangular mesh 1				
Element order	1	2	3	4	5	6	7
DOFs	172854	674793	157752	310392	506232	745272	1027512
1	151.23	150.18	150.30	150.24	150.22	150.21	150.21
2	264.57	263.31	263.67	263.58	263.56	263.55	263.55
3	402.68	400.81	401.57	401.42	401.36	401.33	401.32
4	523.65	519.21	520.03	519.84	519.78	519.76	519.75
5	585.27	580.52	581.55	581.34	581.28	581.25	581.24
6	848.30	842.56	844.49	844.22	844.12	844.08	844.06
7	940.70	936.36	939.35	939.14	939.08	939.06	939.05
8	1107.91	1107.17	1107.67	1107.30	1107.18	1107.12	1107.08
9	1122.34	1113.29	1116.01	1115.73	1115.64	1115.61	1115.59
10	1193.38	1185.58	1189.82	1189.43	1189.31	1189.27	1189.25
	C3D8	C3D20	2D rectangular mesh 2				
Element order	1	2	3	4	5	6	7
DOFs	172854	674793	81072	157752	256032	375912	517392
1	151.23	150.18	150.38	150.27	150.24	150.22	150.22
2	264.57	263.31	263.96	263.70	263.61	263.57	263.56
3	402.68	400.81	401.96	401.60	401.45	401.39	401.35
4	523.65	519.21	520.14	519.89	519.80	519.76	519.75
5	585.27	580.52	581.98	581.53	581.37	581.30	581.27
6	848.30	842.56	844.91	844.43	844.23	844.14	844.10
7	940.70	936.36	939.93	939.40	939.20	939.11	939.08
8	1107.91	1107.17	1108.26	1107.58	1107.33	1107.22	1107.15
9	1122.34	1113.29	1116.51	1115.96	1115.75	1115.66	1115.62
10	1193.38	1185.58	1190.79	1189.88	1189.51	1189.36	1189.29
	C3D8	C3D20	Triangular mesh				
Element order	1	2	3	4	5	6	7
DOFs	172854	674793	100062	233568	404910	614088	861102
1	151.23	150.18	150.35	150.26	150.23	150.22	150.21
2	264.57	263.31	263.81	263.63	263.58	263.56	263.55
3	402.68	400.81	401.87	401.55	401.43	401.38	401.35
4	523.65	519.21	520.06	519.85	519.78	519.76	519.75
5	585.27	580.52	581.93	581.49	581.36	581.30	581.27
6	848.30	842.56	844.85	844.39	844.22	844.14	844.10
7	940.70	936.36	939.65	939.26	939.13	939.09	939.07
8	1107.91	1107.17	1108.37	1107.60	1107.36	1107.24	1107.17
9	1122.34	1113.29	1116.34	1115.85	1115.70	1115.64	1115.62
10	1193.38	1185.58	1190.24	1189.58	1189.37	1189.30	1189.27

tively. The mode frequencies from the reference solution are very accurately predicted by the present formulation, both for rectangular and triangular discretizations. Even when lower-order shape functions are used, the accuracy of the solution remains very high, especially in the first modes. Indeed, from the representation of the convergence rate shown in Fig. 7, an exponential decay of the discrepancy parameter e_i is observed, with a minimal difference between the results obtained using Lagrange and Hermite shape functions. For a triangular mesh, a higher

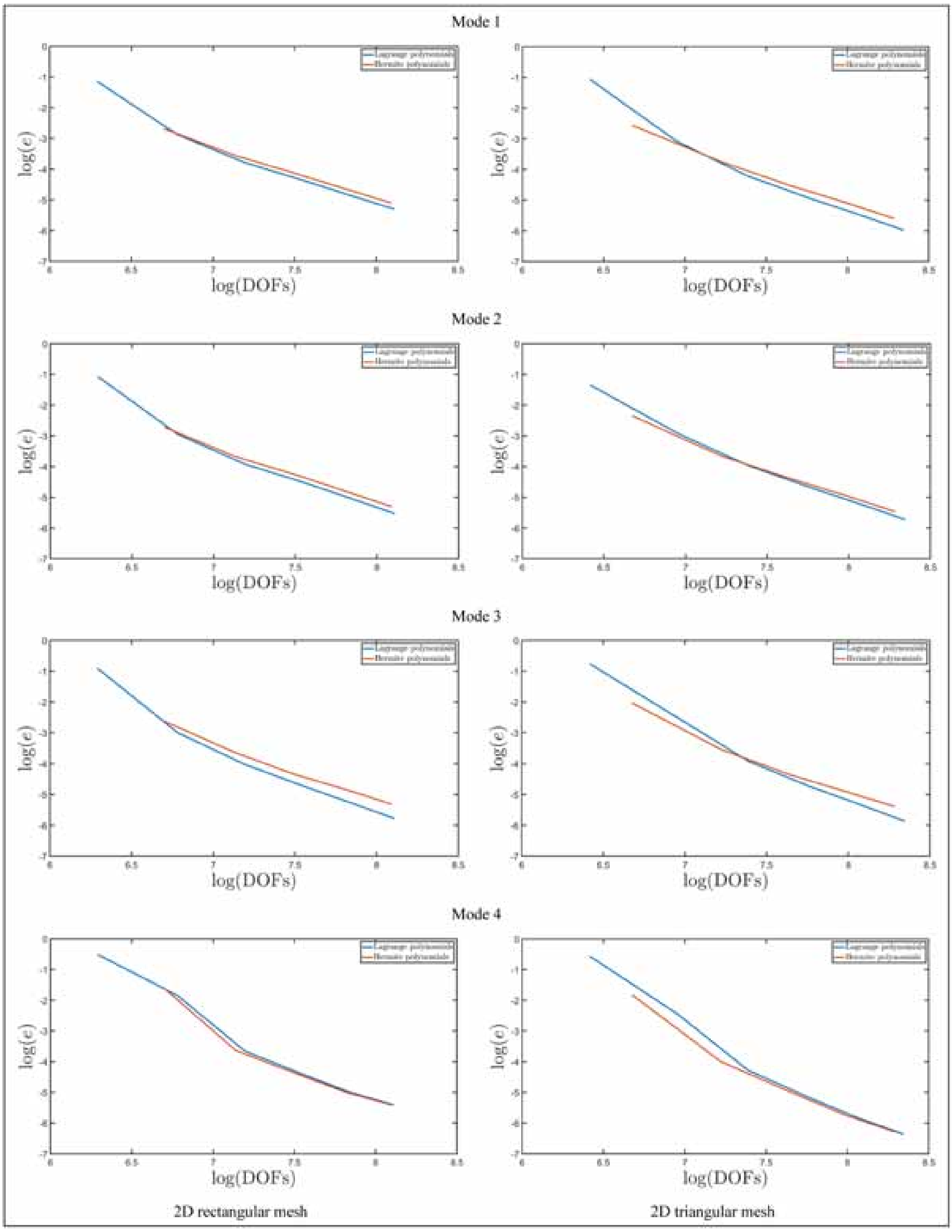

Fig. 7. Convergence rate of the first four mode frequencies of a laminated L-plate derived from the 2D FEM model with respect to the 3D FEM solution. The number of unknown variables is increased by using higher-order polynomials for finite element discretization.

accuracy level is achieved compared to the rectangular mesh simulations, especially when higher-order polynomials are used to discretize the unknown variables. Finally, the first nine mode shapes of the plate, derived from the 3D FEM model, are presented in Fig. 8 for completeness.

At this point, the convergence of the solution is assessed for a laminated circular cylinder with a U-shaped physical domain. The reference surface equation in curvilinear principal coordinates is given below, setting $R_2 = R = 0.5\,\text{m}$ and $L_1 = 1.5\,\text{m}$ the radius and the length of the cylinder, respectively:

$$\mathbf{r}(\alpha_1, \alpha_2) = \mathbf{r}(x, \vartheta) = R_0(x)\cos\vartheta\,\mathbf{e}_1 - R_0(x)\sin\vartheta\,\mathbf{e}_2 + x\sin\varphi\,\mathbf{e}_3 \tag{102}$$

where $R_0(x) = R_b + x\cos\varphi$ with $R_b = R$ and $\varphi = \pi/2$. A rectangular hole is introduced into the original rectangular physical domain $[\alpha_1^0, \alpha_1^1] \times [\alpha_2^0, \alpha_2^1] = [0, L_1] \times [-\pi/3, \pi/3]$, whose origin is located at $(\overline{\alpha}_1, \overline{\alpha}_2) = (0, -\pi/6)$ and dimensions $L_1/2$ and $\pi/3$ along α_1, α_2, respec-

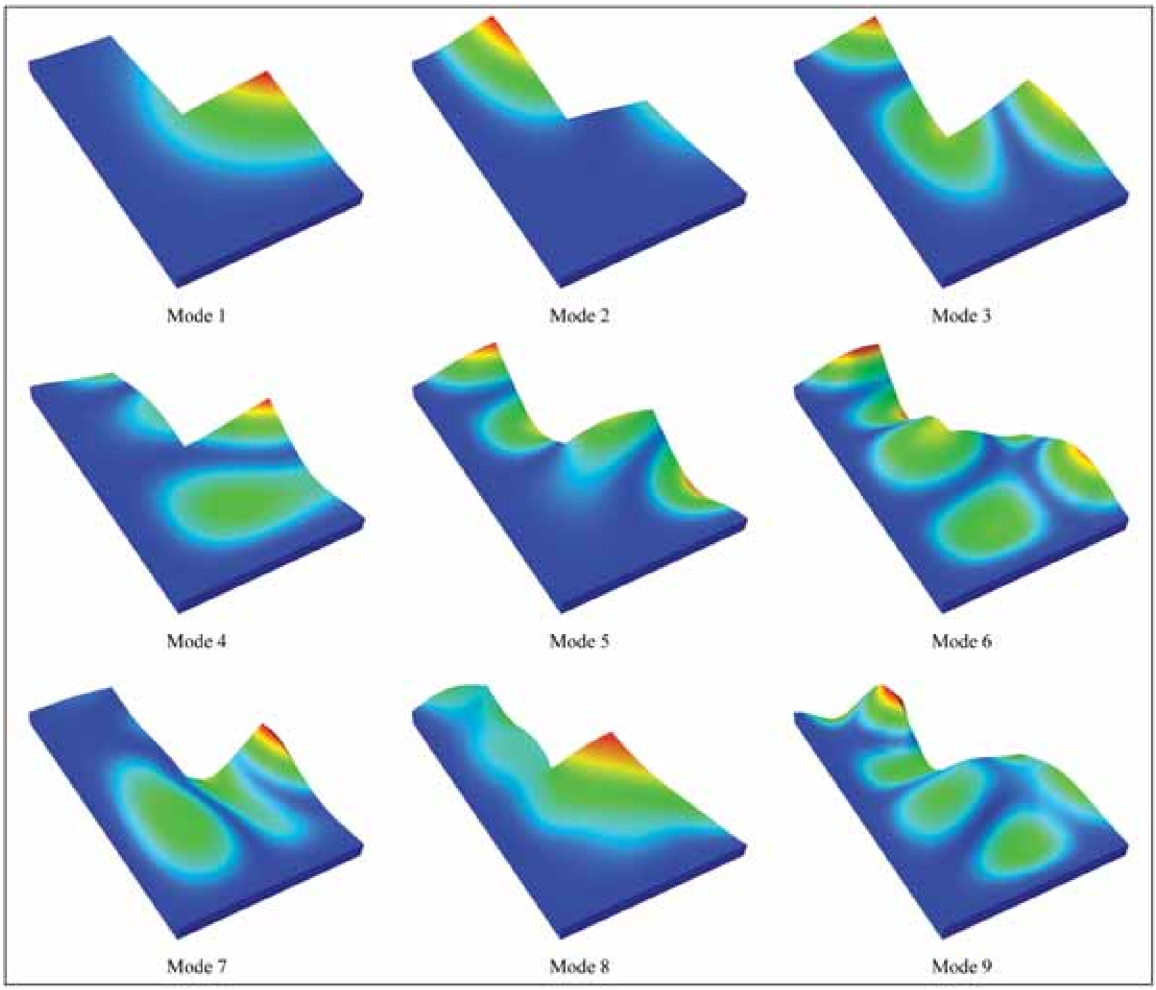

Fig. 8. First nine mode shapes of an L-shaped plate made of orthotropic and anisotropic materials. The 3D representation of the vibration modes is derived from 3D FEM analysis.

tively. The layers and the stacking sequence of the panel are the same as those in the L-shaped plate. As can be seen in Fig. 9, a 3D FEM simulation using parabolic brick elements is performed to derive the reference solution for comparison purposes. The HSDT-based 2D FEM model considers both a rectangular mesh and a triangular discretization, with 20 elements on the edges A, C and F, while edge B contains 40 elements. In addition, 10 elements are placed along edges D, E, G, and H. The first ten natural frequencies of the structure are evaluated under two different boundary conditions sets. In the first configuration, denoted as “Boundary conditions 1”, the curved lateral surfaces of the solid, associated with the edges B, D, and H are clamped. In contrast, for the “boundary conditions 2” configuration, the clamped kinematic constraint is applied to the straight lateral surfaces, which correspond to the edges A and C of the 2D parametric domain. The analysis is performed using both Lagrange and Hermite shape functions of different orders, and the results are reported in Tables 4 and 5. The adoption of higher-order theories provides an excellent agreement with 3D FEM predictions for any mesh discretization in all boundary condition configuration. Moreover, a rapid convergence of results is observed for an increased order of the interpolating polynomials. Looking at results from 3D FEM and 2D FEM simulations, it can be seen that the adoption of higher-order shape functions with the EDZ4 kinematic model ensures perfect alignment with results from the 3D FEM model which adopts parabolic brick elements. However, when 8-node brick elements are used in the 3D analysis, a discrepancy of results is observed. A 3D representation of the first nine mode frequencies is shown in Fig. 10. These mode frequencies are obtained from 3D FEM model and reveal that, even for lower-order modes, the vibration orientations do not follow the principal directions of the structure. This is due to the orthotropic or anisotropic material assumption.

The next numerical investigation focuses on another singly-curved laminated panel. A conical shell made of three layers with thicknesses $h_1 = 0.01\,\mathrm{m}$, $h_2 = 3h_1$, and $h_3 = 2h_1$ is considered. The reference surface equation of this shell is provided in Eq. (102) by assuming the inclination angle as $\varphi = \pi/6$, while the quantity R_b is assumed equal to 0.5 m. The lamination scheme selected in this case is $(10/35/75)$, and consists of graphite-epoxy (84), triclinic material (86), and glass epoxy (85) in the first, second, and third lamina, respectively. The panel is described by the rectangular physical domain $[\alpha_1^0, \alpha_1^1] \times [\alpha_2^0, \alpha_2^1] = [0, L_1] \times [-\pi/3, \pi/3]$ with $L_1 = 1.5\,\mathrm{m}$. In addition, a rectangular hole is located in the center of the physical domain with origin at $(L_1/4, -\pi/6)$, and length along α_1, α_2 equal to $L_1/2$ and $\pi/3$, respectively. The discretization of the 2D physical domain is applied with both rectangular and triangular elements, as shown in Fig. 11, introducing 20 elements along the edges A and C, and 40 elements along edges B and D. On the other hand, the number of elements along E, F, G, and H edges is equal to 10.

The numerical results are reported in Table 6 in terms of the first ten natural frequencies as provided by higher-order theories. Here, the numerical predictions of the present 2D-FEM-based model are compared with results from 3D FEM, using various kinematic models ranging from the EDZ1 to EDZ4 theories. In addition, the sensitivity of the results with

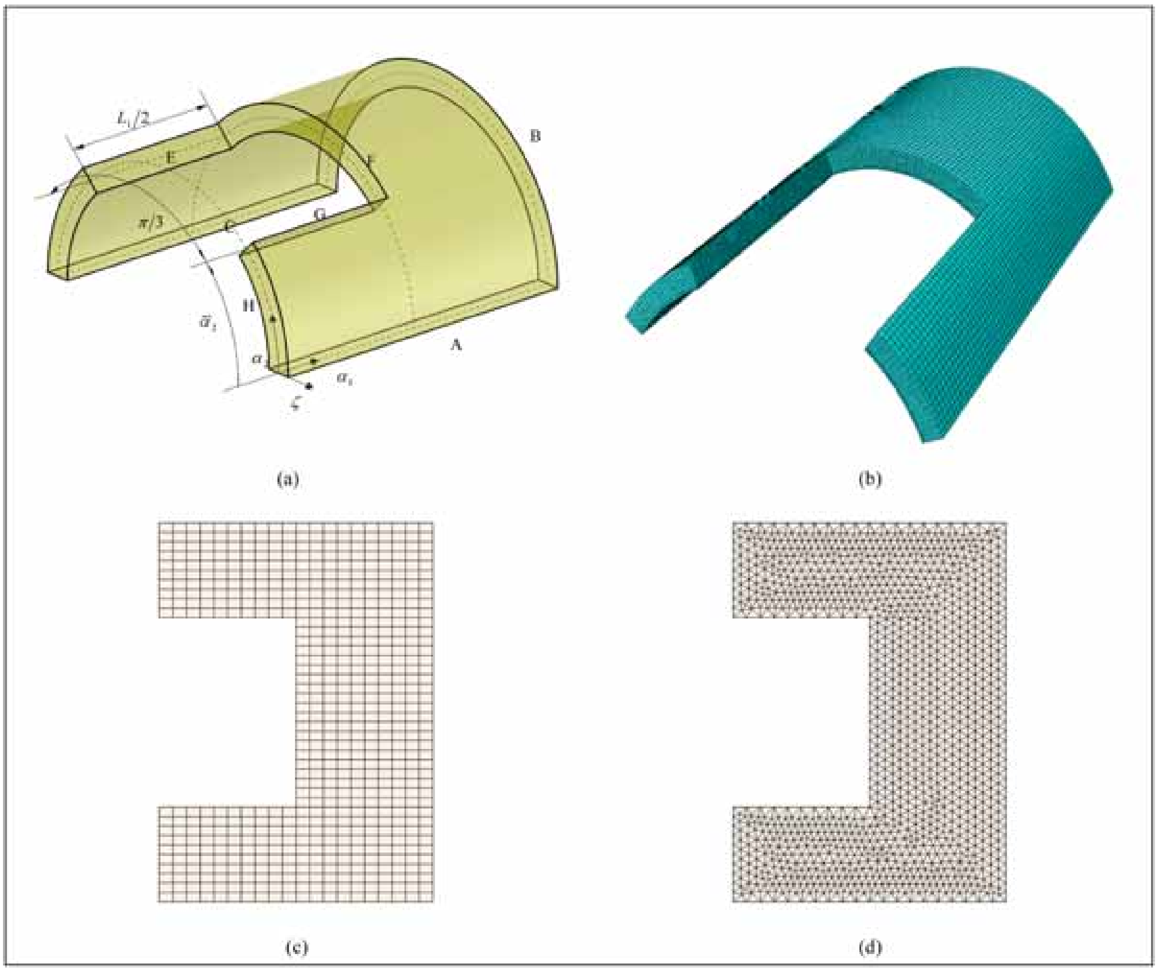

Fig. 9. 3D representation of the geometry of a U-shaped circular cylinder (a). Finite element discretization with brick elements (b) and discretizations with rectangular (c) and triangular (d) elements of the physical domain in 2D FEM analysis.

Table 4
First ten natural frequencies of a laminated anisotropic U-shaped circular cylinder employing different mesh discretizations and Lagrange interpolating polynomials. Numerical investigations are conducted for various boundary conditions sets.

Mode f [Hz]	3D FEM		EDZ4						
FCFCFFFH									
	C3D8	C3D20	2D rectangular mesh						
Element order	1	2	1	2	3	4	5	6	7
DOFs	244140	953433	12078	45738	100998	177858	276318	396378	538038
1	145.73	144.57	161.22	145.14	144.64	144.47	144.39	144.36	144.33
2	180.09	178.64	195.38	178.21	177.66	177.48	177.39	177.35	177.32
3	295.16	293.38	317.51	297.85	296.88	296.58	296.45	296.38	296.35
4	309.93	306.13	358.50	309.27	307.92	307.51	307.32	307.22	307.17
5	325.50	322.35	371.05	326.40	325.18	324.80	324.63	324.54	324.49
6	446.92	445.20	477.64	449.74	448.74	448.44	448.31	448.24	448.20
7	500.54	499.51	514.01	500.79	499.72	499.37	499.21	499.13	499.09
8	530.06	526.85	577.22	529.75	528.11	527.68	527.49	527.39	527.33
9	564.76	558.77	645.20	564.35	562.28	561.73	561.47	561.34	561.26
10	590.37	584.73	676.39	591.82	589.59	589.01	588.76	588.62	588.54
	C3D8	C3D20	Triangular mesh						
Element order	1	2	1	2	3	4	5	6	7
DOFs	244140	953433	22896	89010	198360	350946	546768	785826	1068120
1	145.73	144.57	159.12	144.75	144.47	144.38	144.34	144.32	144.31
2	180.09	178.64	193.01	177.80	177.48	177.38	177.33	177.31	177.30
3	295.16	293.38	313.98	297.11	296.58	296.42	296.36	296.33	296.32
4	309.93	306.13	342.43	308.26	307.52	307.29	307.19	307.14	307.12
5	325.50	322.35	357.65	325.53	324.83	324.61	324.51	324.46	324.44
6	446.92	445.20	481.16	449.27	448.53	448.32	448.24	448.19	448.17
7	500.54	499.51	513.19	499.93	499.36	499.18	499.10	499.07	499.06

(continued on next page)

Table 4 (*continued*)

Mode *f* [Hz]	3D FEM		EDZ4						
FCFCFFFH									
	C3D8	C3D20	2D rectangular mesh						
Element order	1	2	1	2	3	4	5	6	7
DOFs	244140	953433	12078	45738	100998	177858	276318	396378	538038
8	530.06	526.85	583.61	528.66	527.70	527.45	527.35	527.31	527.29
9	564.76	558.77	617.20	562.74	561.70	561.41	561.28	561.22	561.19
10	590.37	584.73	648.41	590.33	589.06	588.72	588.58	588.52	588.48
CFCFFFFF									
	C3D8	C3D20	2D rectangular mesh						
Element order	1	2	1	2	3	4	5	6	7
DOFs	244140	953433	12078	45738	100998	177858	276318	396378	538038
1	425.64	422.13	161.22	145.14	144.64	144.47	144.39	144.36	144.33
2	495.71	492.23	195.38	178.21	177.66	177.48	177.39	177.35	177.32
3	504.17	500.77	317.51	297.85	296.88	296.58	296.45	296.38	296.35
4	640.60	637.99	358.50	309.27	307.92	307.51	307.32	307.22	307.17
5	650.87	648.14	371.05	326.40	325.18	324.80	324.63	324.54	324.49
6	684.74	680.50	477.64	449.74	448.74	448.44	448.31	448.24	448.20
7	738.34	734.88	514.01	500.79	499.72	499.37	499.21	499.13	499.09
8	756.45	753.32	577.22	529.75	528.11	527.68	527.49	527.39	527.33
9	979.84	976.47	645.20	564.35	562.28	561.73	561.47	561.34	561.26
10	1004.76	1004.13	676.39	591.82	589.59	589.01	588.76	588.62	588.54
	C3D8	C3D20	Triangular mesh						
Element order	1	2	1	2	3	4	5	6	7
DOFs	244140	953433	22896	89010	198360	350946	546768	785826	1068120
1	425.64	422.13	434.89	422.05	421.44	421.25	421.18	421.16	421.15
2	495.71	492.23	512.20	492.86	491.81	491.50	491.40	491.36	491.35
3	504.17	500.77	522.60	502.12	501.10	500.80	500.70	500.67	500.66
4	640.60	637.99	655.96	641.08	640.55	640.40	640.35	640.33	640.32
5	650.87	648.14	680.60	651.76	650.98	650.75	650.66	650.62	650.60
6	684.74	680.50	730.19	683.22	681.85	681.48	681.35	681.31	681.28
7	738.34	734.88	778.86	738.30	736.76	736.26	736.04	735.94	735.88
8	756.45	753.32	802.77	757.94	756.68	756.28	756.11	756.03	755.98
9	979.84	976.47	1018.84	980.18	979.07	978.77	978.65	978.60	978.58
10	1004.76	1004.13	1041.00	1012.24	1011.56	1011.35	1011.27	1011.23	1011.20

Table 5

First ten natural frequencies of a laminated anisotropic U-shaped circular cylinder employing different mesh discretizations and Hermite interpolating polynomials. Numerical investigations are conducted for various boundary conditions sets.

Mode *f* [Hz]	3D FEM		2D FEM				
Boundary conditions 1							
	C3D8	C3D20	2D rectangular mesh				
Element order	1	2	3	4	5	6	7
DOFs	244140	953433	79434	156294	254754	37814	516474
1	145.73	144.57	144.75	144.52	144.43	144.38	144.35
2	180.09	178.64	177.84	177.57	177.45	177.39	177.35
3	295.16	293.38	297.08	296.67	296.50	296.41	296.37
4	309.93	306.13	308.24	307.66	307.41	307.28	307.21
5	325.50	322.35	325.75	325.09	324.80	324.66	324.57
6	446.92	445.20	449.37	448.75	448.49	448.36	448.28
7	500.54	499.51	499.81	499.40	499.23	499.14	499.10
8	530.06	526.85	528.53	527.85	527.58	527.44	527.37
9	564.76	558.77	562.48	561.81	561.52	561.37	561.28
10	590.37	584.73	590.29	589.31	588.92	588.72	588.62
	C3D8	C3D20	Triangular mesh				
Element order	1	2	3	4	5	6	7
DOFs	244140	953433	111924	264510	460332	699390	981684
1	145.73	144.57	144.68	144.48	144.40	144.37	144.34
2	180.09	178.64	177.79	177.53	177.43	177.38	177.35
3	295.16	293.38	296.90	296.57	296.44	296.39	296.36
4	309.93	306.13	308.13	307.59	307.37	307.26	307.20
5	325.50	322.35	325.57	324.98	324.74	324.62	324.55
6	446.92	445.20	449.20	448.65	448.43	448.33	448.26
7	500.54	499.51	499.77	499.38	499.22	499.15	499.11
8	530.06	526.85	528.17	527.65	527.46	527.38	527.34
9	564.76	558.77	562.23	561.66	561.43	561.32	561.26
10	590.37	584.73	589.89	589.09	588.79	588.65	588.58

(*continued on next page*)

Table 5 (*continued*)

Mode f [Hz]	3D FEM		2D FEM				
Boundary conditions 1							
	C3D8	C3D20	2D rectangular mesh				
Element order	1	2	3	4	5	6	7
DOFs	244140	953433	79434	156294	254754	37814	516474
Boundary conditions 2							
	C3D8	C3D20	2D rectangular mesh				
Element order	1	2	3	4	5	6	7
DOFs	244140	953433	79434	156294	254754	374814	516474
1	425.64	422.13	421.67	421.36	421.25	421.20	421.18
2	495.71	492.23	492.21	491.68	491.49	491.42	491.39
3	504.17	500.77	501.42	500.93	500.76	500.70	500.68
4	640.60	637.99	640.86	640.55	640.44	640.39	640.36
5	650.87	648.14	651.52	651.01	650.81	650.72	650.67
6	684.74	680.50	682.73	681.85	681.54	681.41	681.36
7	738.34	734.88	738.79	737.35	736.73	736.41	736.23
8	756.45	753.32	758.34	757.13	756.63	756.38	756.24
9	979.84	976.47	979.88	979.18	978.90	978.76	978.69
10	1004.76	1004.13	1012.46	1011.81	1011.54	1011.41	1011.34
	C3D8	C3D20	Triangular mesh				
Element order	1	2	3	4	5	6	7
DOFs	244140	953433	111924	264510	460332	699390	981684
1	425.64	422.13	421.67	421.35	421.24	421.20	421.18
2	495.71	492.23	492.22	491.67	491.49	491.42	491.39
3	504.17	500.77	501.40	500.91	500.75	500.70	500.68
4	640.60	637.99	640.86	640.55	640.44	640.39	640.36
5	650.87	648.14	651.56	651.02	650.82	650.73	650.68
6	684.74	680.50	682.63	681.79	681.52	681.41	681.35
7	738.34	734.88	738.80	737.32	736.72	736.40	736.22
8	756.45	753.32	758.32	757.10	756.61	756.37	756.23
9	979.84	976.47	979.86	979.15	978.88	978.76	978.69
10	1004.76	1004.13	1012.38	1011.77	1011.53	1011.40	1011.33

respect to the adoption of the zigzag function is checked for various boundary conditions. For boundary conditions 1, the structure is clamped along the lateral surface corresponding to the straight edges A and C, while the remaining parts are free. In contrast, boundary conditions 2 account for the clamping of the curved lateral surfaces associated with B and D edges of the physical domain. Finally, in boundary conditions 3, the structure is clamped from the lateral surfaces of the solid that define the rectangular hole, namely E, F, G, and H. It can be shown that the vibration frequencies of the panel under consideration obtained from 3D FEM cannot be predicted with lower-order theories. However, the results from EDZ4 are obtained with a lower number of DOFs compared to the 3D FEM and maintain a high accuracy level for all boundary condition sets. In addition to the previous investigation, in Fig. 12, a convergence analysis against 3D FEM results is presented for the first four modes for a boundary condition set in which the lateral surfaces associated with physical domain edges A, B, and D, are clamped. More specifically, the convergence of the solution is shown for both discretizations with the rectangular and the triangular meshes employing Lagrange and Hermite shape functions. The convergence parameter of Eq. (101) is reported for the first four modes in logarithmic scale with respect to the number of DOFs for each simulation. A rapid convergence of results is observed since a negative value of $\ln(e_i)$ is found even with a limited number of DOFs. However, unlike the previous analysis, in this case the convergence for the first and second modes differs when adopting Lagrange or Hermite polynomials. On the other hand, for the third and fourth modes, very similar curves are obtained with different shape functions. Finally, the first nine mode shapes of the structure are reported in Fig. 13, derived from the 3D FEM simulation for the boundary conditions 3 configuration, showing that the 2D FEM formulation allows to consider also kinematic constraints that are not commonly addressed by classical numerical simulations on doubly-curved laminated shells, which are mainly based on the clamping of the external parts of the structure.

At this point, another free vibration analysis is conducted on the same conical shell by introducing four holes throughout the panel. A 3D geometric representation of the cone under investigation is reported in Fig. 14. Here, the 2D physical domain is discretized with 40 elements along the edges B and D, while the edges of the holes in the 2D domains are discretized with 8 elements each. Each rectangular hole has dimensions $\pi/6$ and $2L_1/7$ along α_1, α_2, respectively, while the origin of the four holes is located at the coordinates $\overline{\alpha}_1^{(d)} = L_1/7, 4L_1/7, 4L_1/7, L_1/7$ and $\overline{\alpha}_2^{(d)} = -\pi/5, -\pi/5, \pi/15, \pi/15$ within the rectangular physical domain. A reference solution is evaluated from 3D FEM analysis with a model developed from commercial software, consisting of 64800 parabolic brick elements with 287865 nodes. Then, the 2D HDST FEM model is adopted with both rectangular and triangular meshes to determine the first ten natural frequencies for various kinematic expansion orders, ranging from the EDZ1 to the EDZ4 theory. The results are reported in Table 7 for triangular and rectangular mesh employing Lagrange and Hermite polynomials of the seventh order. The boundary conditions set accounts for the full clamping of the lateral surface of the 3D cone associated with the edge A of the 2D domain. For both boundary conditions, the natural frequencies obtained from the EDZ4 are very similar to those derived from 3D analysis, meaning that the model requires a higher-order kinematic expansion to correctly investigate the vibrational response of the structure. Furthermore, the same level of accuracy is reached with fewer DOFs when employing the triangular mesh. Similar results are then obtained with triangular discretization, highlighting that when higher-order elements are adopted, very accurate results are obtained regardless of the specific mesh discretization. Finally, a 3D representation of the first nine mode frequencies for boundary conditions 1 is provided in Fig. 15.

At this point, an additional example is introduced which aims at deriving the first ten natural frequencies of an anisotropic laminated

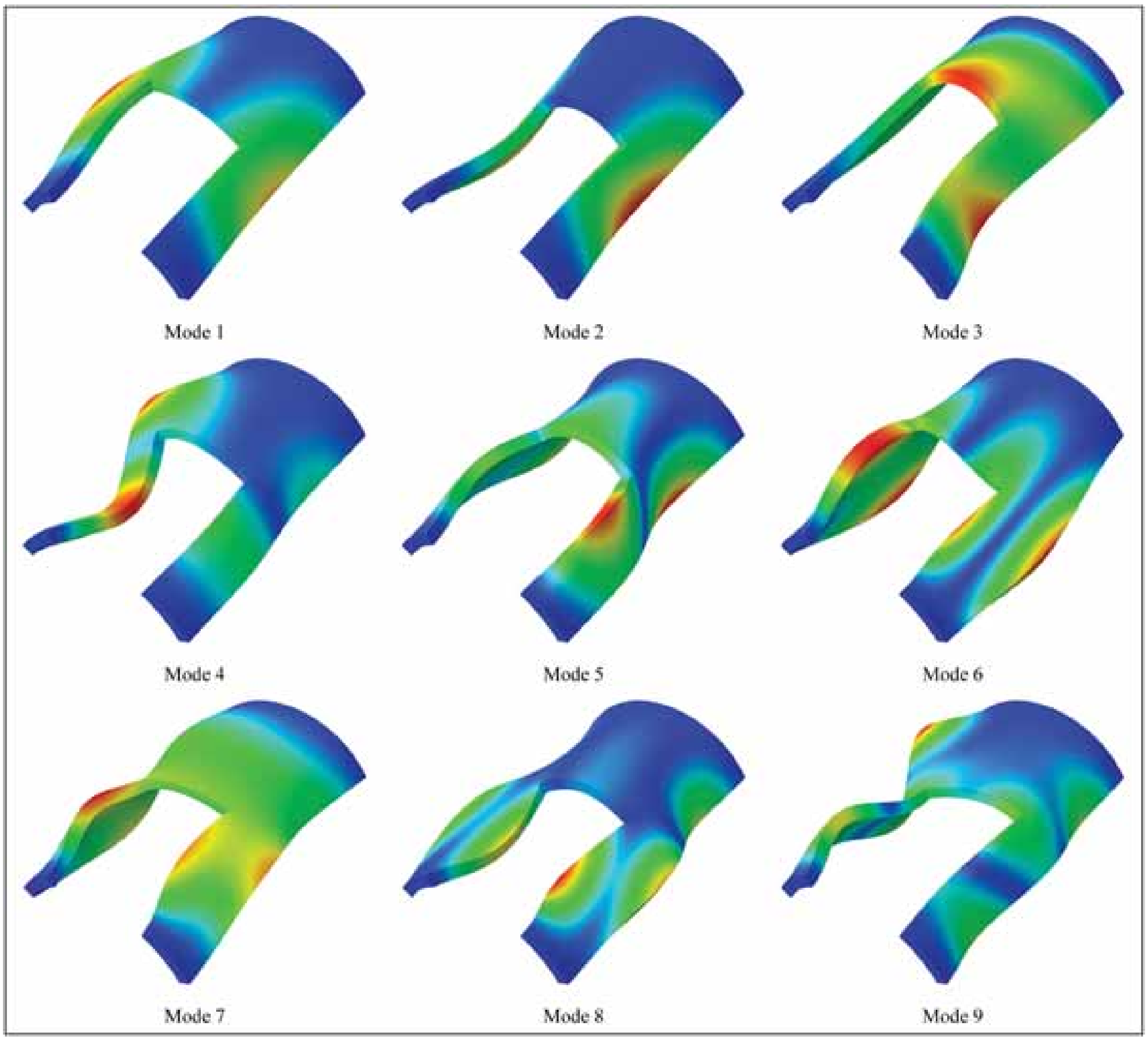

Fig. 10. 3D representation of the first nine mode shapes of a U-shaped circular cylinder made of orthotropic and anisotropic materials clamped along its curved lateral surfaces. These mode shapes are evaluated from 3D FEM numerical analysis.

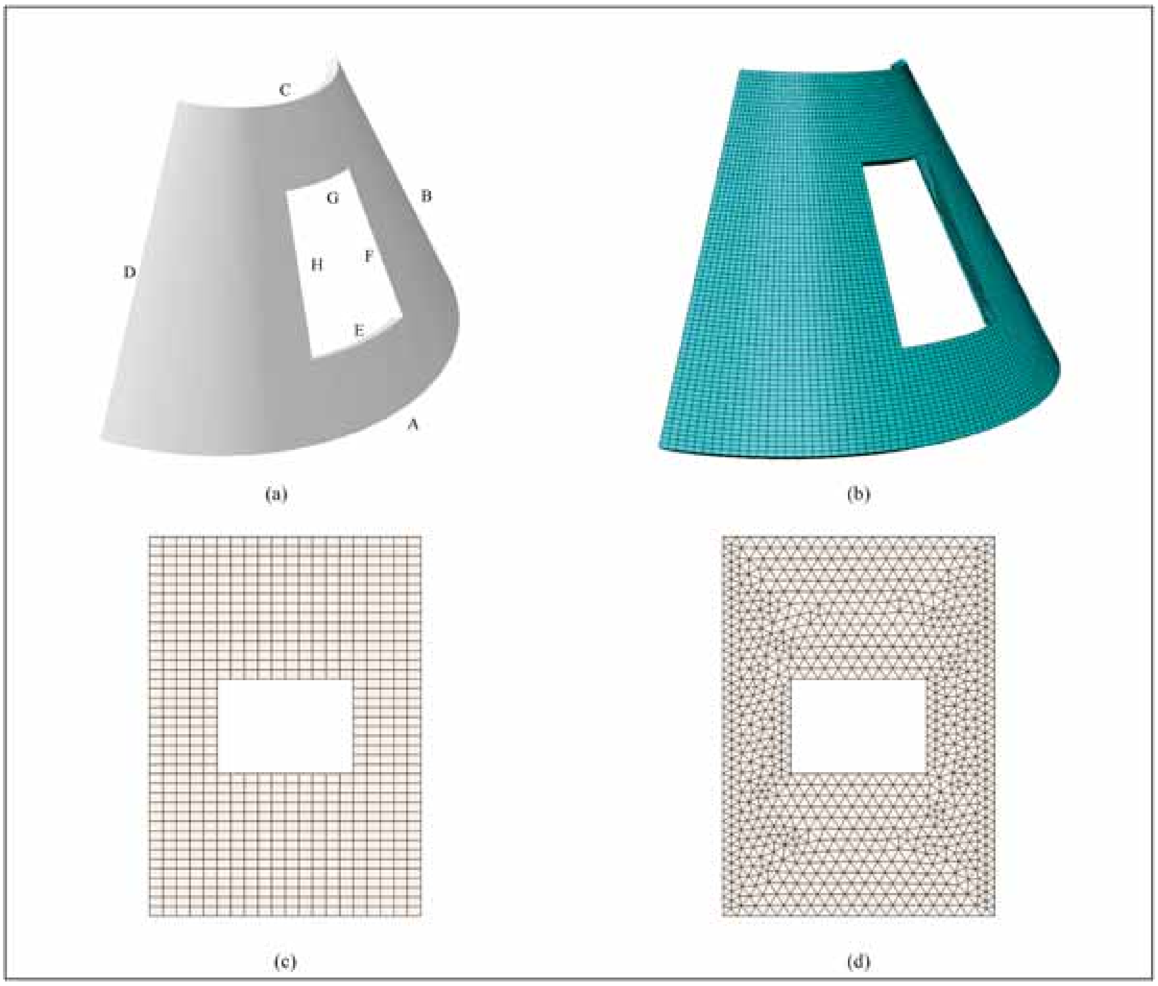

Fig. 11. 3D geometric representation of a truncated cone with a central rectangular hole (a). Discretization with brick elements adopted in 3D FEM analysis (b) and discretizations of the physical domain employing rectangular (c) and triangular (d) elements.

Table 6
Free vibration analysis of a laminated anisotropic truncated cone with a central rectangular hole employing higher-order theories. Comparison with 3D FEM for various boundary conditions. The results are derived from the higher-order 2D FEM model employing Lagrange shape functions of seventh order and with rectangular mesh.

Mode f [Hz] DOFs	3D FEM 1366140	EDZ1 313740	ED2 313740	EDZ2 418320	ED3 418320	EDZ3 522900	ED4 522900	EDZ4 627480
Boundary conditions 1								
1	80.98	85.83	81.30	81.23	81.38	81.29	81.31	81.24
2	140.85	148.66	141.68	141.57	141.85	141.68	141.72	141.62
3	196.20	203.01	196.46	196.25	197.01	196.66	196.86	196.56
4	206.65	211.17	206.66	206.39	207.33	206.95	207.23	206.84
5	248.19	262.78	249.28	249.07	249.79	249.39	249.50	249.27
6	292.49	297.65	292.80	292.59	293.06	292.81	292.94	292.75
7	315.14	328.15	315.86	315.46	316.61	316.08	316.36	315.91
8	347.82	365.82	349.07	348.80	350.02	349.41	349.64	349.25
9	399.09	417.61	400.22	399.84	401.01	400.42	400.67	400.24
10	416.35	431.96	417.56	417.15	418.57	417.88	418.19	417.69
Boundary conditions 2								
1	121.59	124.93	121.82	121.59	121.99	121.84	121.96	121.76
2	122.27	125.31	122.37	122.15	122.53	122.39	122.50	122.31
3	170.68	174.79	171.12	170.85	171.67	171.35	171.60	171.24
4	184.05	188.21	184.35	184.06	184.83	184.53	184.76	184.42
5	284.59	292.87	285.10	284.37	286.09	285.47	285.99	285.17
6	285.72	293.33	286.24	285.51	287.13	286.55	287.04	286.25
7	351.47	365.62	352.84	352.12	353.82	353.16	353.64	352.83
8	378.72	395.08	380.11	379.50	381.06	380.42	380.84	380.11
9	394.96	413.57	396.43	395.93	397.36	396.71	397.07	396.43
10	409.55	428.07	410.59	410.04	411.57	410.91	411.33	410.64

(*continued on next page*)

Table 6 (*continued*)

Mode f [Hz] DOFs	3D FEM 1366140	EDZ1 313740	ED2 313740	EDZ2 418320	ED3 418320	EDZ3 522900	ED4 522900	EDZ4 627480
Boundary conditions 3								
1	40.86	43.88	40.72	40.68	40.72	40.69	40.69	40.67
2	44.92	47.61	44.75	44.72	44.77	44.73	44.73	44.70
3	84.13	89.17	83.50	83.41	83.72	83.60	83.66	83.54
4	93.32	98.11	92.88	92.81	93.08	92.96	93.01	92.90
5	162.49	172.45	163.05	162.84	163.46	163.21	163.33	163.09
6	178.77	185.32	179.54	179.39	180.09	179.79	179.94	179.70
7	185.05	188.13	184.41	184.20	184.68	184.48	184.63	184.42
8	195.78	198.66	195.45	195.25	195.80	195.57	195.73	195.51
9	289.24	297.28	290.03	289.62	290.92	290.45	290.80	290.25
10	318.69	328.97	319.56	319.18	320.57	320.01	320.36	319.82

shell with double non-uniform curvature, characterized by an irregular hole located at the center of the structure. The panel under consideration is an elliptic paraboloid, whose reference surface equation in principal coordinates in the same as in Eq. (99) with $k^{\alpha_1} = 2$ and $k^{\alpha_2} = 3$ as the governing geometric parameters. The rectangular physical domain is defined so that $[\alpha_1^0,\alpha_1^1] \times [\alpha_2^0,\alpha_2^1] = [-0.7,0.7] \times [-0.5,0.5]$. The shape of the hole is described by the NURBS curves adopted to map the structure in the first example, following the knots, weights, and control points vector already presented in Fig. 5, while the position of the hole is defined from the point located at $(-0.5, -0.5)$, in line with conventions shown in Fig. 2. The 2D domain is discretized with rectangular and triangular elements according to Fig. 16, considering 40 elements along the edges A and C. When dealing with the curved edges of the hole, the so-called curvature factor has been adopted to determine the size of finite elements, and, consequently, the corresponding number of elements along the curved boundaries. The size of the element along a curved edge is determined by the product of the curvature factor and the curvature radius of the geometric boundary. In this example, the value 0.3 is adopted for the curvature factor. On the other hand, a maximum growing rate is introduced to limit the variation of dimensions throughout the physical domain. This parameter is considered equal to 1 for the rectangular discretization, while assuming a value of 1.3 for a triangular discretization. The doubly-curved shell solid is assumed to be clamped at its lateral surfaces corresponding to edges A, B, C, and D in the 2D parametric domain. The reference values of the first ten mode frequencies are computed from a 3D FEM simulation developed with commercial software, considering 94400 brick elements. Furthermore, the results derived with the present 2D FEM model are evaluated by employing Lagrange and Hermite polynomials of different orders and collected in Table 8. Three different mesh discretizations are used, namely a triangular mesh, a sparse rectangular mesh named “rectangular mesh 1”, and a refined rectangular mesh named “rectangular mesh 2”. For all the discretizations considered in the analysis, the physical domain is discretized with 50 and 30 elements along A, C and B, D edges, respectively. For the 2D “rectangular mesh 1”, 57 elements are introduced along each curved edge of the hole, while in the “rectangular mesh 2” and in the case of the “triangular mesh”, 19 elements are placed along the curved boundaries. In this case, the accuracy of the numerical discretization for the 2D HSDT analysis is checked by employing the EDZ4 kinematic model with different orders of the interpolating shape functions. The numerical predictions from the ESL model are in line with 3D FEM results when the latter adopts parabolic brick elements, although discrepancies are found when compared to 8-node-based 3D simulations. In addition, the same level of accuracy is observed for both lower and higher modes, indicating that the model can be suitably used to predict the dynamic behavior of these structures. Another important aspect is that the accuracy of the results is not affected by the mesh discretization, for the same number of variables. This means that a sparse mesh can be used if higher-order interpolating functions are adopted for a finite element implementation. On the other hand, meshing technique adopted here considers only linear mapping techniques for rectangular and triangular elements, meaning that the curved edges of the hole are approximated by several straight lines. Finally, the first nine mode shapes of the panel are derived from the 3D FEM analysis and are reported in Fig. 17. Based on results, it is worth observing a consistent deformation of the curved edges for all mode shapes, therefore an accurate geometric description of the structure is required to accurately predict the real vibrational response of the structure.

In the final numerical investigation, the modal response of a doubly-curved shell element exhibiting a line crack parallel to the parametric lines of the reference surface is studied. More specifically, the reference surface of the panel is an elliptic paraboloid, described in curvilinear principal coordinates by Eq. (99), with the main geometric parameters of the parabolic curves along α_1 and α_2, respectively, set as $k^{\alpha_1} = (a_1^2 - d_1^2)/b_1 = 9$ and $k^{\alpha_2} = (a_2^2 - d_2^2)/b_2 = 18$, being $a_1 = a_2 = 3$, $d_1 = d_2 = 0$, $b_1 = 1$ and $b_2 = 0.5$. The rectangular physical domain of the structure is defined as $[\alpha_1^0,\alpha_1^1] \times [\alpha_2^0,\alpha_2^1] = [-0.58800,0.58800] \times [-0.32175,0.32175]$. In line with the geometric representation in Fig. 18, a line crack is introduced within the structure, oriented along the parametric lines of α_1 direction. The crack has a length within the physical domain is $0.5(\alpha_1^1 - \alpha_1^0)$, with its origin located at $(0.5(\alpha_1^1 - \alpha_1^0) + \alpha_1^0, 0.5(\alpha_2^1 - \alpha_2^0) + \alpha_2^0)$. The structure consists of three layers with thickness $h_1 = 0.08\,\text{m}$, $h_2 = 0.12\,\text{m}$ and $h_3 = 0.10\,\text{m}$. More specifically, the two external laminae are made of graphite-epoxy (84), while the second lamina is made of triclinic material (86). The lamination scheme is $(20/35/75)$. The structure is clamped along the uncracked lateral surfaces, while the cracked area is free. A 3D FEM model is developed from commercial software, consisting of 773763 parabolic tetrahedral elements, named C3D10, and 1111899 nodes, for a total number of 3335697 DOFs. The present higher-order 2D formulation for this structure is performed with a finite element model. The numerical discretization of the problem is based on triangular 2D elements. The mesh discretization accounts for a maximum and minimum element dimension equal to 0.14 and 0.05, respectively, with a growth ratio set at 1.2. Furthermore, the edges of the physical domains along α_1 direction are characterized by 40 elements, while those associated with α_2 contain 20 elements. Furthermore, the edges of the domain defining the line crack are characterized by 30 elements. The first ten mode frequencies of the structure are listed in Table 9. Here, a direct comparison is made between the results derived from the EDZ4 theory and those ones from the

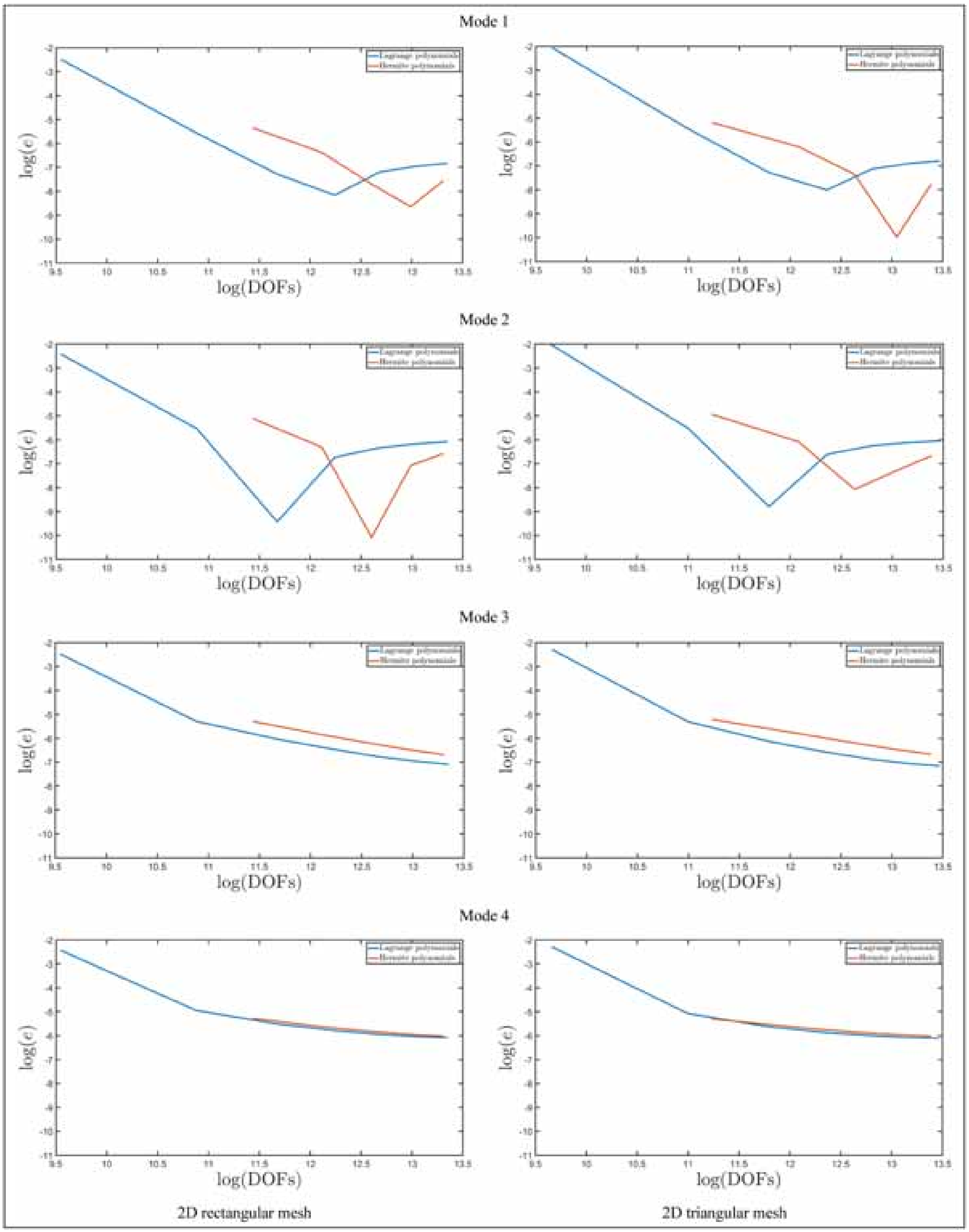

Fig. 12. Convergence rate of the first four mode frequencies of a laminated anisotropic truncated cone derived from the 2D FEM model with respect to the 3D FEM solution. The number of unknown variables is increased by using higher-order polynomials for finite element discretization.

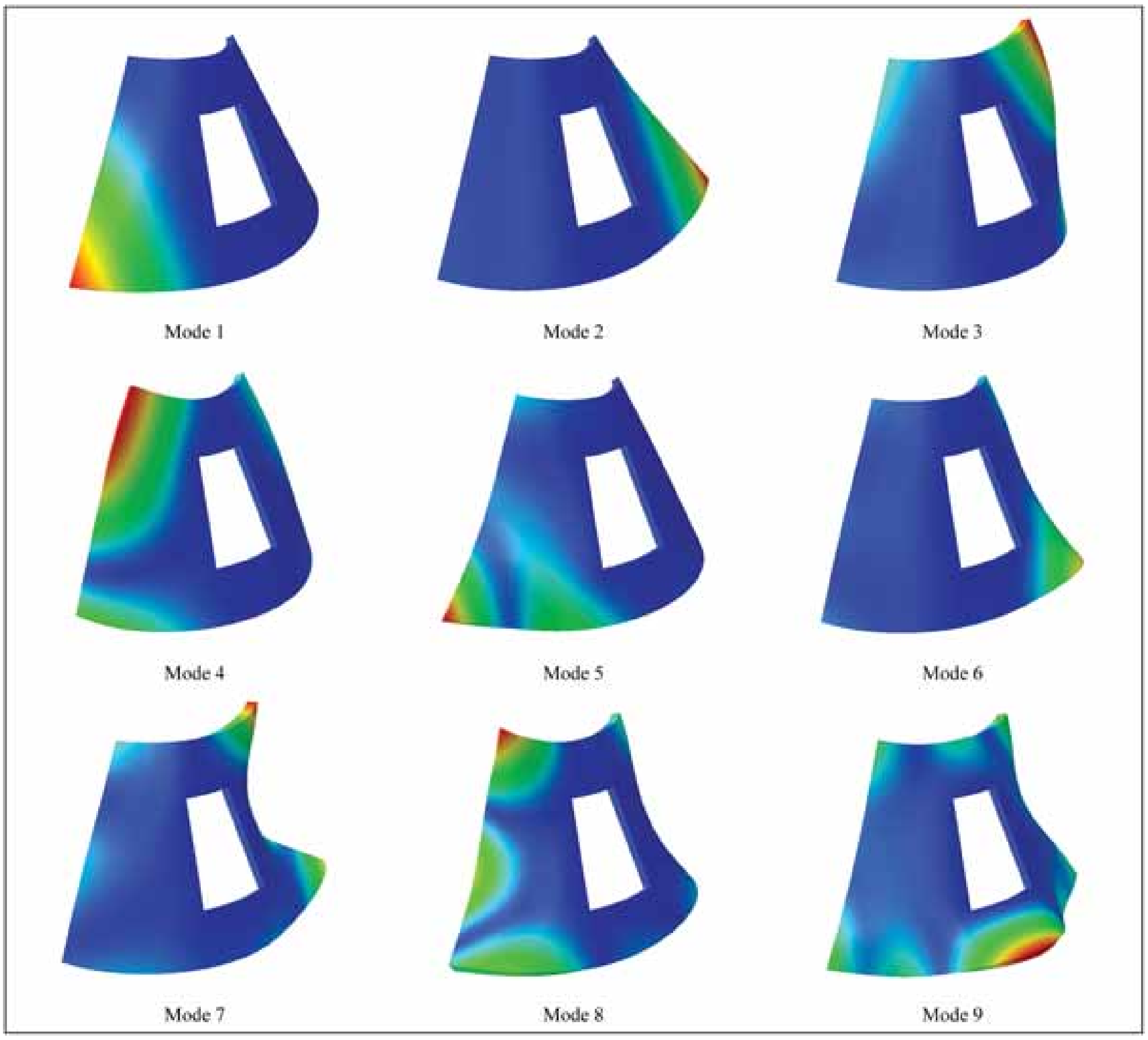

Fig. 13. First nine mode shapes of a laminated anisotropic truncated cone with a single rectangular hole, located in the centre of the structure, whose edges are parallel to the principal parametric lines of the structure. These mode shapes are evaluated from 3D FEM numerical analysis.

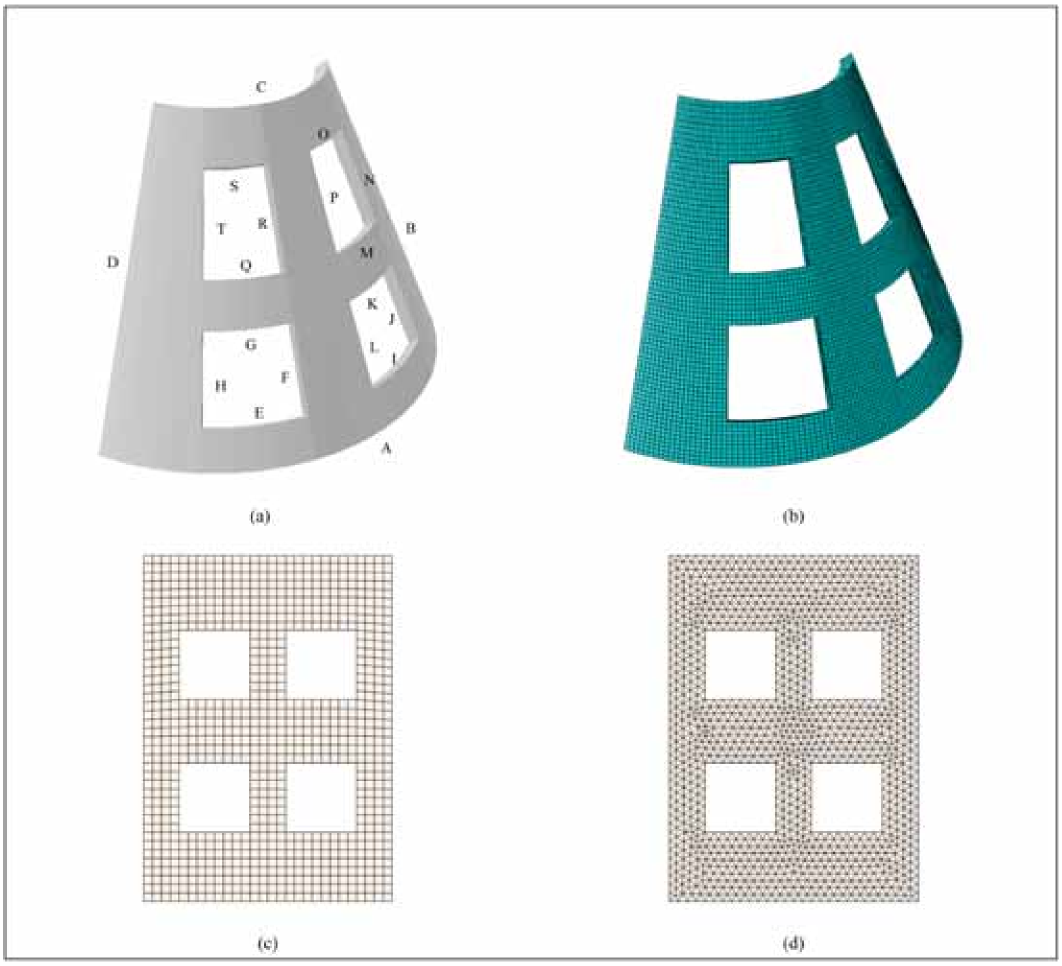

(a) (b)

(c) (d)

Fig. 14. 3D geometric model of singly-curved conical shell with four rectangular hole uniformly distributed throughout the structure (a). Discretization for 3D FEM simulations employing parabolic brick elements (b) and 2D mesh adopted for the solution with higher-order theories. 2D rectangular (c) and 2D triangular (d) mesh.

Table 7
Free vibration analysis of a truncated cone with four rectangular holes clamped along the lateral surface A. Comparison between 3D FEM and 2D FEM with various kinematic models employing both Lagrange and Hermite polynomials. Effect of higher-order theories and zigzag function.

Mode f [Hz] Triangular mesh	3D FEM	EDZ1	ED2	EDZ2	ED3	EDZ3	ED4	EDZ4
Lagrange polynomials								
DOFs	863595	262368	262368	349824	349824	437280	437280	524736
1	48.91	50.93	49.37	49.31	49.47	49.38	49.43	50.00
2	69.45	72.58	69.61	69.53	69.73	69.60	69.64	70.49
3	102.70	106.15	104.75	104.60	104.80	104.66	104.73	104.29
4	133.67	138.40	134.45	134.30	134.79	134.50	134.63	135.36
5	159.27	167.30	160.17	160.04	160.61	160.26	160.37	160.78
6	185.23	193.04	187.63	187.46	188.03	187.70	187.85	186.74
7	213.36	224.52	216.82	216.57	217.49	216.95	217.17	217.69
8	228.00	238.13	237.39	236.99	237.34	237.09	237.24	237.39
9	258.03	265.73	258.22	257.95	258.98	258.42	258.69	258.31
10	267.46	277.03	270.41	270.10	271.45	270.78	271.15	270.36
Hermite polynomials								
DOFs	863595	241380	241380	321840	349824	437280	402300	482760
1	48.91	50.97	49.40	49.34	49.47	49.38	49.47	50.04
2	69.45	72.62	69.64	69.57	69.73	69.60	69.68	70.52
3	102.70	106.32	104.92	104.77	104.80	104.66	104.90	104.47
4	133.67	138.49	134.53	134.38	134.79	134.50	134.71	135.44
5	159.27	167.41	160.28	160.15	160.61	160.26	160.49	160.90
6	185.23	193.23	187.81	187.63	188.03	187.70	188.03	186.91
7	213.36	224.83	217.09	216.85	217.49	216.95	217.45	217.96
8	228.00	238.83	238.08	237.69	237.34	237.09	237.93	238.08
9	258.03	265.95	258.44	258.17	258.98	258.42	258.91	258.54
10	267.46	277.21	270.60	270.29	271.45	270.78	271.32	270.54

(*continued on next page*)

Table 7 (*continued*)

Mode *f* [Hz] Triangular mesh	3D FEM	EDZ1	ED2	EDZ2	ED3	EDZ3	ED4	EDZ4
Lagrange polynomials								
DOFs	863595	262368	262368	349824	349824	437280	437280	524736
Rectangular mesh								
Lagrange polynomials								
DOFs	863595	216315	216315	288420	288420	360525	360525	432630
1	48.91	50.93	49.37	49.31	49.47	49.38	49.43	50.00
2	69.45	72.59	69.61	69.53	69.73	69.60	69.65	70.49
3	102.70	106.15	104.75	104.60	104.80	104.66	104.73	104.29
4	133.67	138.40	134.44	134.30	134.79	134.50	134.63	135.36
5	159.27	167.30	160.17	160.04	160.61	160.26	160.37	160.78
6	185.23	193.05	187.64	187.46	188.03	187.70	187.85	186.74
7	213.36	224.51	216.82	216.57	217.49	216.95	217.17	217.68
8	228.00	238.13	237.39	236.99	237.34	237.09	237.24	237.39
9	258.03	265.74	258.22	257.95	258.98	258.42	258.69	258.31
10	267.46	277.03	270.41	270.10	271.45	270.77	271.14	270.35
Hermite polynomials								
DOFs	863595	207675	207675	276900	276900	346125	346125	415350
1	48.91	50.96	49.40	49.33	49.50	49.40	49.46	50.03
2	69.45	72.62	69.64	69.56	69.76	69.63	69.67	70.51
3	102.70	106.28	104.89	104.73	104.94	104.80	104.87	104.43
4	133.67	138.47	134.51	134.37	134.85	134.57	134.69	135.43
5	159.27	167.39	160.26	160.13	160.70	160.35	160.46	160.87
6	185.23	193.20	187.78	187.60	188.17	187.84	187.99	186.88
7	213.36	224.76	217.04	216.79	217.70	217.17	217.39	217.90
8	228.00	238.68	237.94	237.54	237.89	237.64	237.79	237.94
9	258.03	265.91	258.40	258.13	259.15	258.60	258.87	258.50
10	267.46	277.16	270.55	270.24	271.58	270.91	271.27	270.49

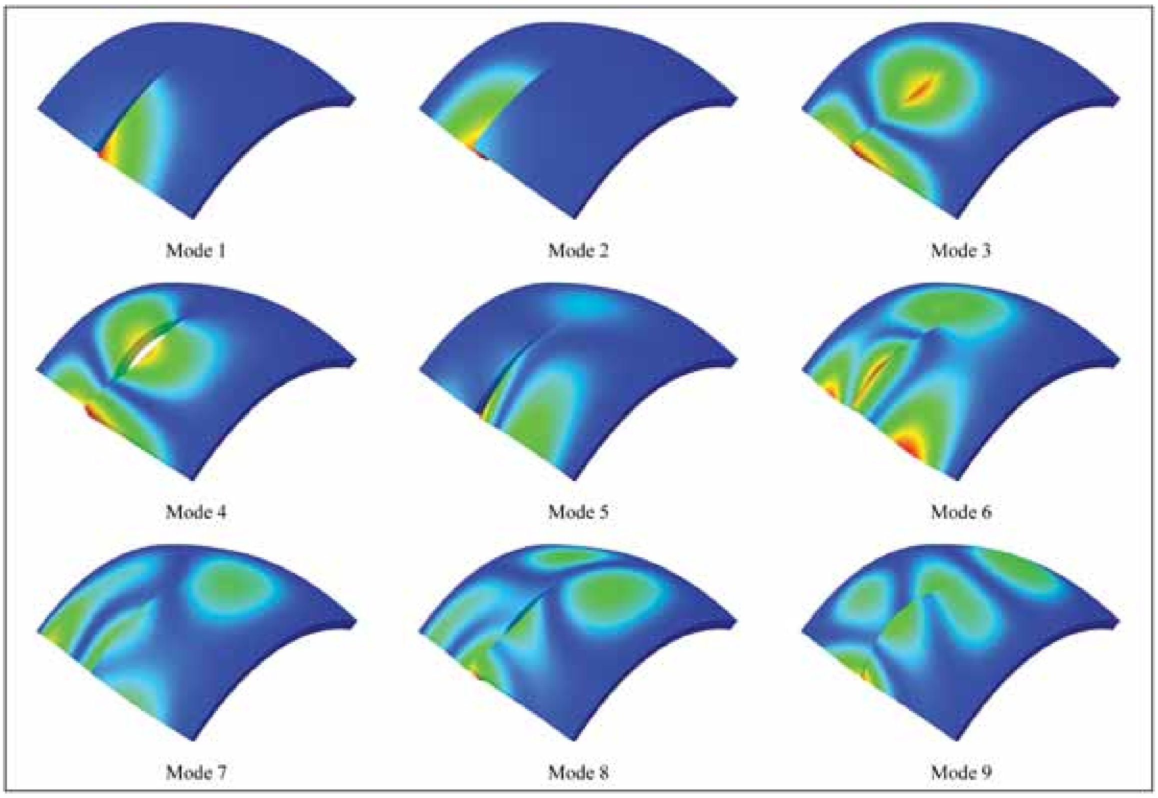

Fig. 19. First nine mode shapes of a laminated elliptic paraboloid made of anisotropic materials characterized by a line crack located in the central part of the structure and oriented along the parametric lines. These mode shapes are evaluated from 3D FEM numerical analysis.

Table 10
Effect of the crack length on the first ten mode frequencies of a cracked elliptic paraboloid made of anisotropic materials. The numerical discretization of the problem is performed by using triangular elements with both Hermite and Lagrange shape functions.

Crack length	$0.5\,L_1$		$0.4\,L_1$	$0.3\,L_1$	$0.2\,L_1$	$0.1\,L_1$	$0.0\,L_1$	
f [Hz]	3D FEM	EDZ4	EDZ4	EDZ4	EDZ4	EDZ4	EDZ4	3D FEM
Hermite shape functions								
DOFs	3335697	747684	782514	818964	853794	916164	357894	3335697
1	29.68	29.70	30.86	33.44	38.02	45.91	63.46	61.23
2	36.27	35.43	36.19	38.49	44.38	58.52	79.79	78.85
3	68.77	68.56	75.62	83.58	89.30	91.81	101.19	100.93
4	76.41	76.33	88.05	98.53	101.11	105.21	111.48	112.91
5	97.38	99.37	99.78	105.18	111.42	114.24	128.94	128.62
6	110.69	111.27	112.78	114.53	119.75	124.04	137.57	136.71
7	115.96	115.63	116.83	118.79	125.03	135.04	145.25	144.24
8	127.68	126.75	131.21	135.66	137.79	139.23	155.39	158.00
9	138.36	136.73	139.38	141.62	149.14	157.73	172.45	172.11
10	156.89	156.27	159.53	161.89	165.35	169.63	174.71	174.62
Lagrange shape functions								
DOFs	3335697	813096	851022	890712	928638	996552	545598	3335697
1	29.68	29.69	30.84	33.33	37.98	45.87	63.46	61.23
2	36.27	35.43	36.17	38.38	44.32	58.45	79.79	78.85
3	68.77	68.50	75.54	83.39	89.28	91.80	101.18	100.93
4	76.41	76.25	87.92	98.42	101.09	105.18	111.48	112.91
5	97.38	99.37	99.77	104.89	111.40	114.22	128.94	128.62
6	110.69	111.25	112.76	114.42	119.72	124.01	137.57	136.71
7	115.96	115.62	116.81	118.71	124.97	135.01	145.25	144.24
8	127.68	126.71	131.15	135.54	137.78	139.22	155.39	158.00
9	138.36	136.70	139.36	141.50	149.09	157.70	172.45	172.11
10	156.89	156.24	159.51	161.81	165.33	169.61	174.71	174.62

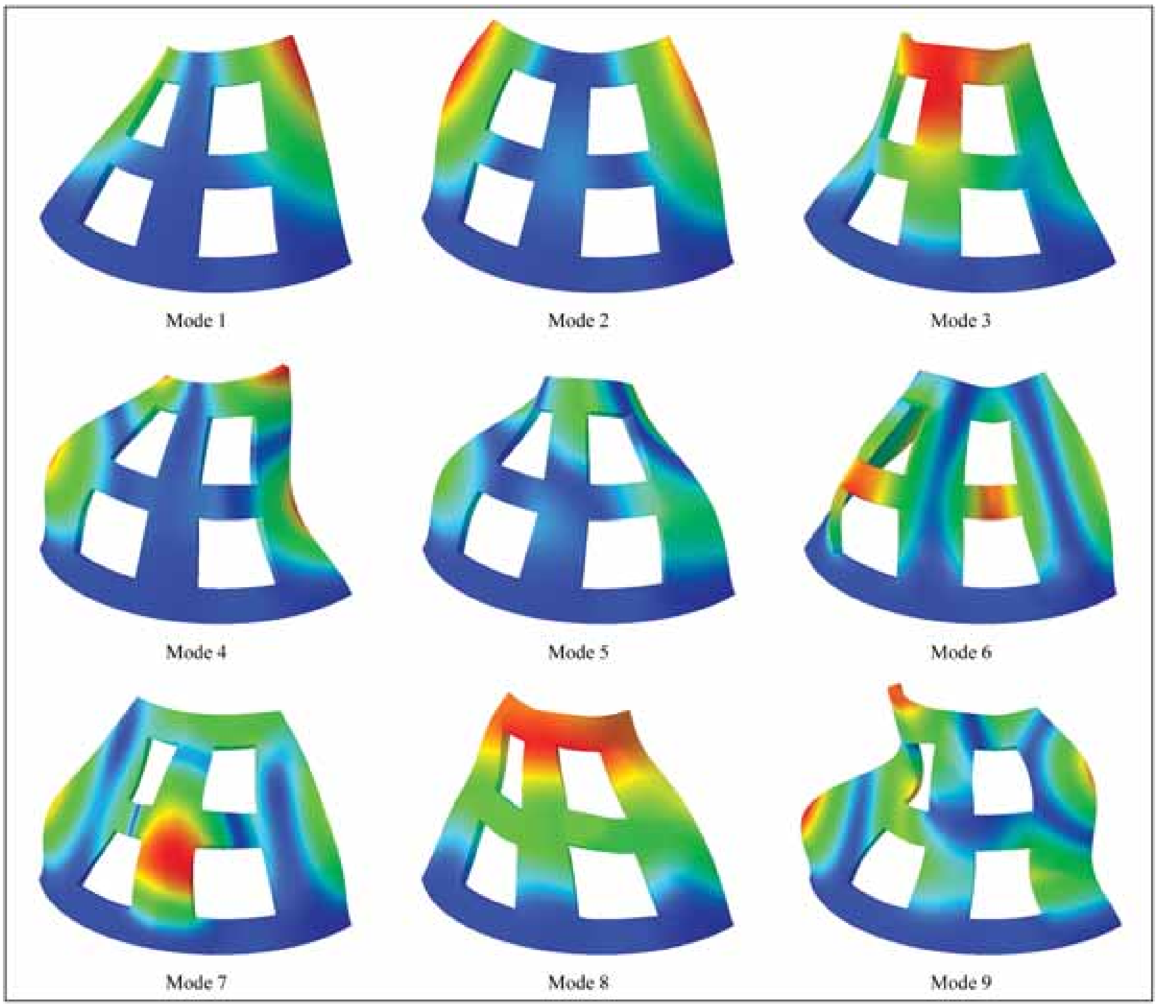

Fig. 15. First nine mode shapes of a laminated anisotropic truncated cone with four rectangular holes, with the edges parallel to the principal parametric lines of the panel. These mode shapes are evaluated from 3D FEM numerical analysis.

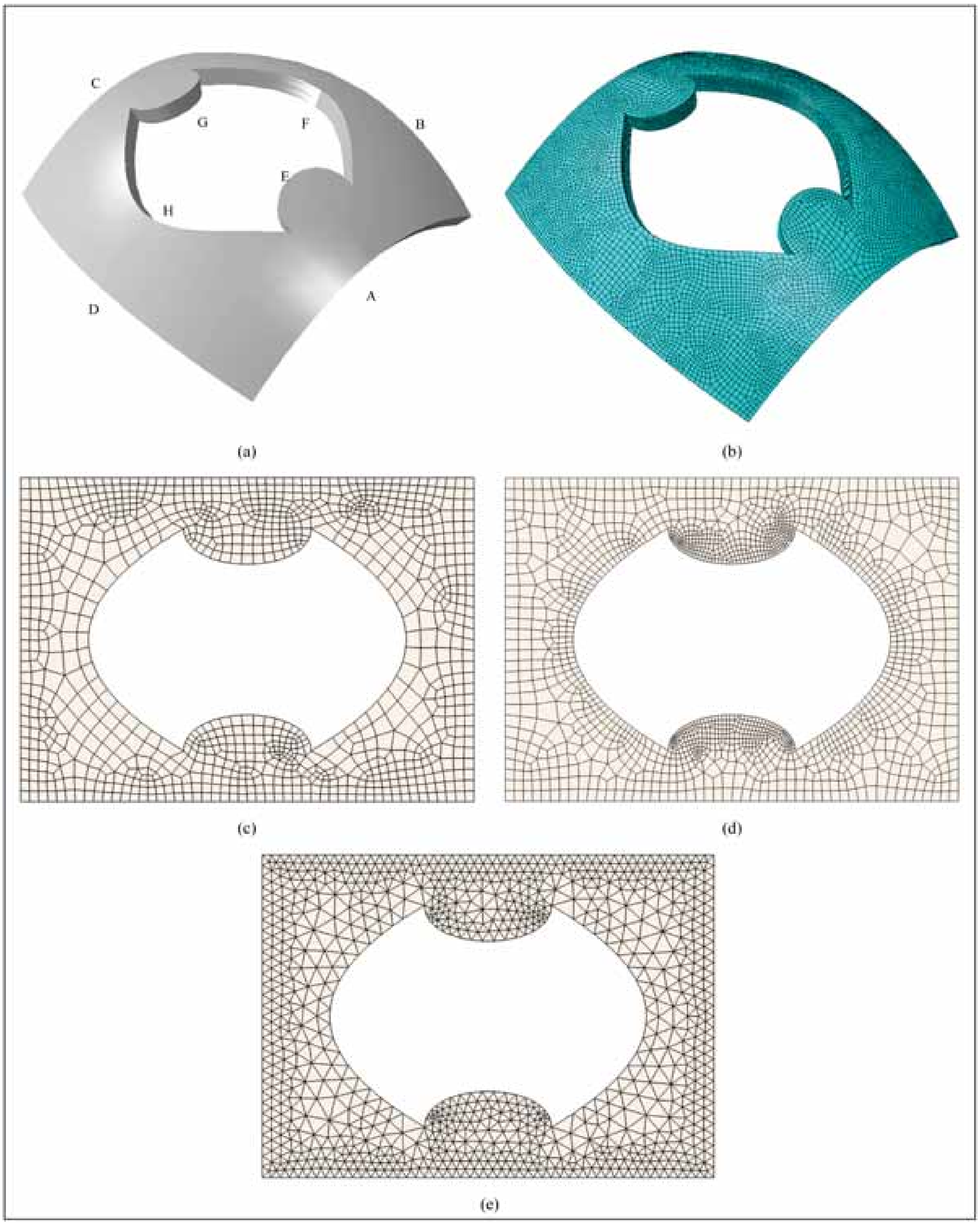

Fig. 16. 3D geometric model of a doubly-curved elliptic paraboloid with a central hole of arbitrary shape (a). Mesh discretization for 3D FEM (b) and discretization of the 2D parametric domain with rectangular elements with sparse (c) and fine (d) discretization, and triangular (e) elements.

Table 8

Free vibration analysis of a fully-clamped elliptic paraboloid with a central hole of arbitrary shape. Comparison with 3D FEM and effect of Hermite and Lagrange shape functions while using rectangular and triangular discretizations.

Element order	1	2	3	4	5	6	7
Mode *f* [Hz]			Hermite polynomials shape functions				
	3D FEM		2D rectangular mesh 1				
DOFs	313446	1222800	143046	276084	446526	654372	899622
1	404.11	399.98	409.89	405.60	403.52	402.35	401.63
2	406.45	402.16	413.49	408.43	406.03	404.70	403.87
3	436.59	433.13	437.72	436.11	435.47	435.14	434.95
4	449.31	445.98	449.59	448.47	448.02	447.78	447.65
5	530.71	528.78	533.23	532.11	531.62	531.35	531.19
6	533.36	530.67	535.93	534.55	533.93	533.60	533.40
7	599.06	594.61	598.88	598.13	597.81	597.64	597.53
8	665.50	659.20	665.03	663.58	662.97	662.65	662.46
9	737.30	730.79	738.73	736.62	735.62	735.06	734.71
10	855.17	847.24	854.41	852.82	852.13	851.76	851.53
	3D FEM		2D rectangular mesh 2				
DOFs	313446	1222800	86832	193536	330120	496584	692928
1	404.11	399.98	411.88	406.61	404.09	402.71	401.86
2	406.45	402.16	415.82	409.51	406.62	405.05	404.10
3	436.59	433.13	438.67	436.48	435.66	435.26	435.03
4	449.31	445.98	450.24	448.76	448.18	447.89	447.72
5	530.71	528.78	533.92	532.43	531.80	531.47	531.27
6	533.36	530.67	536.72	534.92	534.16	533.75	533.50
7	599.06	594.61	599.18	598.25	597.87	597.68	597.56
8	665.50	659.20	665.88	663.99	663.22	662.81	662.57
9	737.30	730.79	739.60	737.04	735.86	735.21	734.81
10	855.17	847.24	855.25	853.22	852.36	851.91	851.63
	3D FEM		2D triangular				
DOFs	313446	1222800	86832	193536	330120	496584	692928
1	404.11	399.98	403.63	401.84	401.01	400.55	400.27
2	406.45	402.16	406.09	404.08	403.15	402.64	402.33
3	436.59	433.13	435.57	435.03	434.81	434.70	434.63
4	449.31	445.98	448.11	447.71	447.55	447.46	447.42
5	530.71	528.78	531.73	531.26	531.07	530.96	530.90
6	533.36	530.67	534.04	533.48	533.24	533.11	533.04
7	599.06	594.61	597.93	597.58	597.45	597.38	597.34
8	665.50	659.20	663.15	662.56	662.32	662.20	662.13
9	737.30	730.79	735.75	734.82	734.41	734.20	734.06
10	855.17	847.24	852.31	851.64	851.36	851.22	851.13

Mode *f* [Hz]			Lagrange shape functions						
	3D FEM		2D rectangular mesh 1						
Element order	1	2	1	2	3	4	5	6	7
DOFs	313446	1222800	22824	69768	146592	253296	389880	556344	752688
1	404.11	399.98	451.51	406.14	402.54	401.26	400.63	400.29	400.07
2	406.45	402.16	454.57	408.95	404.90	403.45	402.75	402.35	402.11
3	436.59	433.13	489.77	437.14	435.38	434.93	434.75	434.66	434.60
4	449.31	445.98	499.14	449.47	448.00	447.65	447.51	447.44	447.40
5	530.71	528.78	571.11	533.14	531.71	531.26	531.07	530.97	530.90
6	533.36	530.67	582.55	535.70	534.02	533.49	533.26	533.13	533.05
7	599.06	594.61	680.64	599.40	597.82	597.51	597.40	597.35	597.31
8	665.50	659.20	758.09	665.48	663.08	662.54	662.32	662.20	662.13
9	737.30	730.79	845.51	738.05	735.31	734.59	734.28	734.10	733.99
10	855.17	847.24	977.97	855.00	852.10	851.53	851.29	851.17	851.09
	3D FEM		2D rectangular mesh 2						
Element order	1	2	1	2	3	4	5	6	7
DOFs	313446	1222800	26586	84816	180450	313488	483930	691776	937026
1	404.11	399.98	428.07	404.98	402.35	401.28	400.72	400.38	400.16
2	406.45	402.16	438.20	408.59	405.03	403.64	402.93	402.52	402.25
3	436.59	433.13	467.68	436.59	435.26	434.90	434.74	434.66	434.61
4	449.31	445.98	481.28	448.96	447.87	447.60	447.49	447.43	447.39
5	530.71	528.78	558.55	532.82	531.60	531.23	531.06	530.96	530.90
6	533.36	530.67	566.97	535.43	533.91	533.45	533.24	533.12	533.05
7	599.06	594.61	655.35	599.17	597.85	597.55	597.43	597.37	597.33
8	665.50	659.20	736.56	664.72	662.88	662.45	662.27	662.17	662.11
9	737.30	730.79	812.84	737.77	735.37	734.68	734.35	734.16	734.05
10	855.17	847.24	946.55	854.26	851.97	851.49	851.29	851.17	851.10
	3D FEM		2D triangular mesh						
Element order	1	2	1	2	3	4	5	6	7
DOFs	313446	1222800	20826	79056	174690	307728	478170	686016	931266
1	404.11	399.98	428.07	404.98	402.35	401.28	400.72	400.38	400.16
2	406.45	402.16	438.20	408.59	405.03	403.64	402.93	402.52	402.25
3	436.59	433.13	467.68	436.59	435.26	434.90	434.74	434.66	434.61
4	449.31	445.98	481.28	448.96	447.87	447.60	447.49	447.43	447.39
5	530.71	528.78	558.55	532.82	531.60	531.23	531.06	530.96	530.90

(*continued on next page*)

Table 8 (*continued*)

Element order	1	2	3	4	5	6		7	
Mode f [Hz]			Hermite polynomials shape functions						
	3D FEM		2D rectangular mesh 1						
DOFs	313446	1222800	143046	276084	446526		654372	899622	
6	533.36	530.67	566.97	535.43	533.91	533.45	533.24	533.12	533.05
7	599.06	594.61	655.35	599.17	597.85	597.55	597.43	597.37	597.33
8	665.50	659.20	736.56	664.72	662.89	662.45	662.27	662.17	662.11
9	737.30	730.79	812.84	737.77	735.37	734.68	734.35	734.16	734.05
10	855.17	847.24	946.55	854.26	851.97	851.49	851.29	851.17	851.10

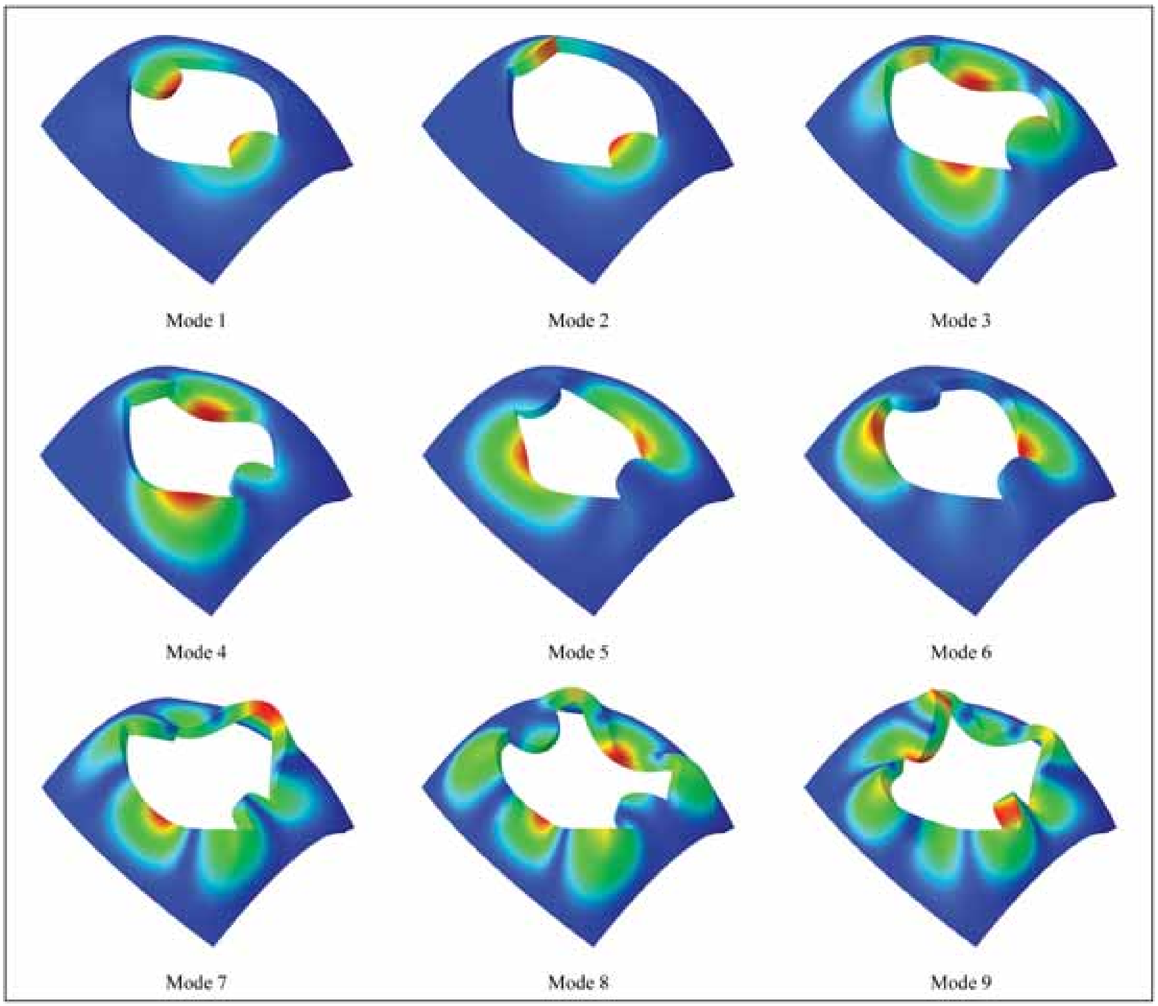

Fig. 17. First nine mode shapes of a laminated anisotropic elliptic paraboloid with a central hole of arbitrary shape. These mode shapes are evaluated from 3D FEM numerical analysis.

3D FEM model. The 2D simulations are performed using triangular elements, and the effects of the order of both Lagrange and Hermite interpolating polynomials are analyzed. The 3D representation of the first nine mode shapes of the cracked structures is shown in Fig. 19. In addition to this preliminary mesh convergence analysis, Table 10 presents a parametric investigation where the crack length is varied continuously, while maintaining the same mesh discretization as in the convergence analysis. The finite element shape functions used are seventh order Hermite polynomials. The results exhibit a smooth transition from the mode frequencies associated with the uncracked configuration of the shell to those of the structure with the maximum crack length. In all cases, the numerical predictions from the EDZ4 solution are successfully validated against those ones from 3D FEM model.

5. Conclusions

In this work, a higher-order 2D formulation based on the ESL approach has been adopted to evaluate the 3D dynamic response of laminated doubly-curved shells made of generally anisotropic materials, described by biconnected domains. A generalized kinematic model has

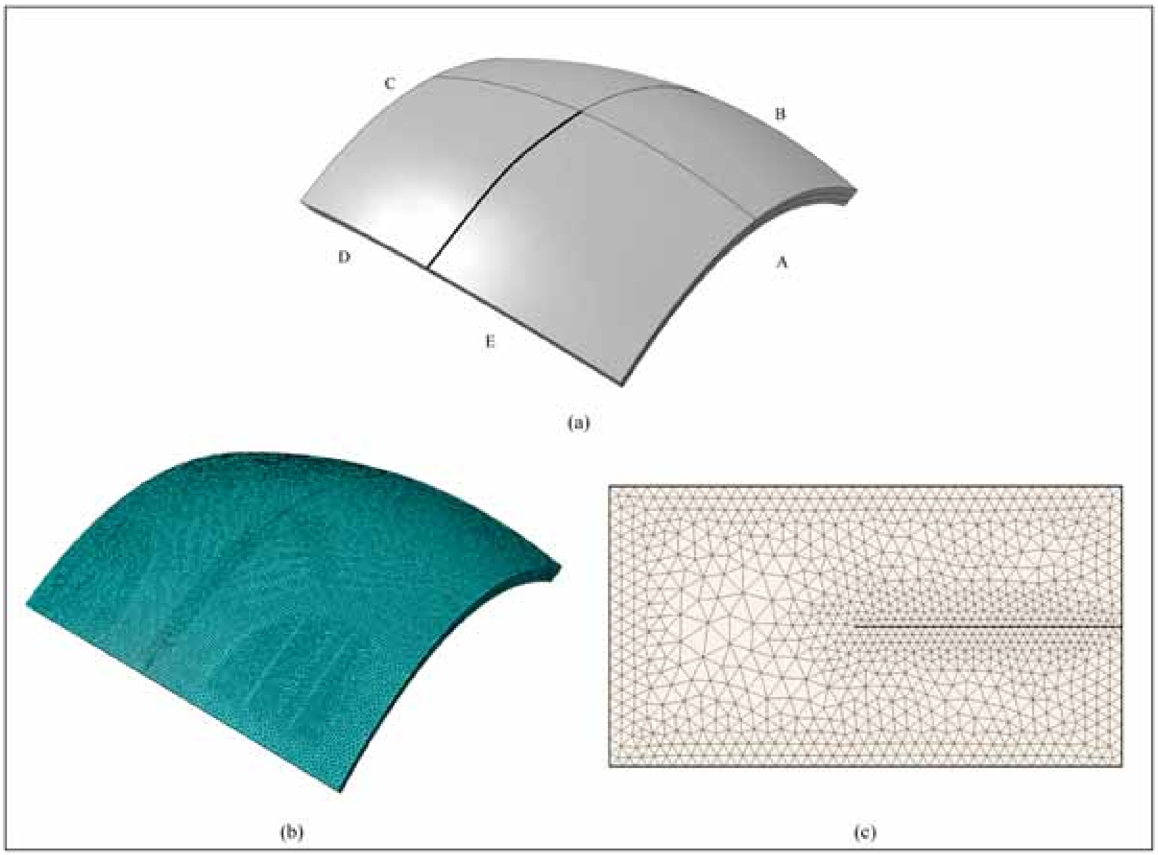

Fig. 18. Laminated anisotropic doubly-curved panel with elliptic paraboloidal shape made of anisotropic material with line crack. (a) geometric representation of the structure in the 3D space and 3D FEM discretization (b). The higher-order 2D FEM model is developed using a triangular 2D discretization (c).

Table 9
First ten mode frequencies of a laminated elliptic paraboloid with a line crack. Comparison with 3D FEM solution and convergence of the higher-order 2D FEM solution based on EDZ4 kinematic model and triangular discretization for various orders of the interpolating shape functions based on Lagrange and Hermite polynomials.

Lagrange shape functions								
Mode *f* [Hz]		Element order						
	3D FEM	1	2	3	4	5	6	7
DOFs	3335697	18000	68706	152136	268290	417168	598770	813096
1	29.68	34.79	29.78	29.72	29.70	29.70	29.69	29.69
2	36.27	39.54	35.50	35.45	35.44	35.43	35.43	35.43
3	68.77	76.51	68.70	68.57	68.54	68.52	68.51	68.50
4	76.41	86.35	76.65	76.40	76.32	76.29	76.27	76.25
5	97.38	108.78	99.54	99.40	99.38	99.37	99.37	99.37
6	110.69	125.75	111.50	111.32	111.28	111.26	111.25	111.25
7	115.96	131.54	115.85	115.67	115.64	115.63	115.63	115.62
8	127.68	141.51	127.10	126.83	126.77	126.74	126.72	126.71
9	138.36	149.95	136.90	136.75	136.72	136.71	136.71	136.70
10	156.89	175.76	156.59	156.32	156.27	156.25	156.24	156.24
Hermite shape functions								
Mode *f* [Hz]		Element order						
	3D FEM	3	4	5	6	7		
DOFs	3335697	86724	202878	351756	533358	747684		
1	29.68	29.77	29.73	29.71	29.70	29.70		
2	36.27	35.48	35.45	35.44	35.44	35.43		
3	68.77	68.85	68.69	68.62	68.58	68.56		
4	76.41	76.78	76.53	76.42	76.36	76.33		
5	97.38	99.44	99.40	99.38	99.38	99.37		
6	110.69	111.46	111.35	111.31	111.28	111.27		
7	115.96	115.74	115.67	115.65	115.64	115.63		
8	127.68	127.04	126.88	126.81	126.77	126.75		
9	138.36	136.90	136.80	136.76	136.74	136.73		
10	156.89	156.50	156.37	156.32	156.29	156.27		

been introduced to characterize the through-the-thickness dispersion of the displacement field components, with the unknown kinematic variables expressed using higher-order Lagrange polynomials on a non-uniform computational grid. In addition, NURBS-based blending functions have been implemented to handle distorted domains. The fundamental equations are derived in curvilinear principal coordinates using the Hamilton principle, computing both the elastic strain energy and the kinetic energy of the system. A numerical solution is found for the weak form of the problem using the GDQ method. The theoretical model has been successfully implemented, allowing to study a wide range of structural problems, in addition to those already investigated with the GDQ-based approach, including panels described by non-rectangular domains such as bi-connected domains and panels with rectangular holes, holes with general shape, and cracks. Different numerical examples demonstrate that the refined 2D FEM solution provides an excellent accuracy compared to classical 3D FEM simulations, considering a variety of curvatures, materials, lamination schemes, and boundary conditions. In addition, a large parametric investigation is carried out to check the sensitivity of the solution. These numerical investigations can be easily performed due to the computational efficiency of the ESL model. Moreover, it has been shown that the higher-order finite element model for shell structures can solve complex structural problems related to mechanical elasticity with a reduced computational effort, such that it could be used for many advanced engineering design applications.

CRediT authorship contribution statement

Francesco Tornabene: Writing – review & editing, Validation, Supervision, Software, Methodology, Investigation, Formal analysis, Data curation, Conceptualization. **Matteo Viscoti:** Writing – original draft, Validation, Software, Investigation, Formal analysis, Data curation. **Rossana Dimitri:** Writing – review & editing, Validation, Supervision, Investigation, Formal analysis, Data curation.

Declaration of competing interest

The authors declare that they have no known competing financial interests or personal relationships that could have appeared to influence the work reported in this paper.

Data availability

No data was used for the research described in the article.

References

[1] Wu W, et al. Mechanostructures: rational mechanical design, fabrication, performance evaluation, and industrial application of advanced structures. Prog Mater Sci 2023;131:101021.
[2] Soboyejo Winston O, Tirumalai SS. Advanced structural materials: properties, design optimization, and applications. Boca Raton: CRC Press; 2006.
[3] Dong Y, Huang N. Multifield and higher-order analysis of sandwich smart curved beams made of graphene origami auxetic metamaterial. Mech Adv Mater Struct 2024;31:12740–58.
[4] Reddy JN. Mechanics of laminated composite plates and shells. Boca Raton: CRC Press; 2003.
[5] Fu F. Advanced modelling techniques in structural design. John Wiley & Sons; 2015.
[6] Liu G, Ji B, Hwang KC, Khoo BC. Analytical solutions of the displacement and stress fields of the nanocomposite structure of biological materials. Compos Sci Technol 2011;71:1190–5.
[7] Pagano NJ. Exact solutions for composite laminates in cylindrical bending. J Compos Mater 1969;3:398–411.
[8] Oden JT, Reddy JN. An introduction to the mathematical theory of finite elements. New York: Dover Publications Inc; 1976.
[9] Gao Z, Chen L. A review of multi-scale numerical modeling of three-dimensional woven fabric. Compos Struct 2021;263:113685.
[10] Zienkiewicz OC, Taylor RL. The Finite Element Method: Solid Mechanics. Oxford: Butterworth Heinemann; 2000.
[11] Liu WK, Li S, Park HS. Eighty years of the finite element method: birth, evolution, and future. Arch Comput Methods Eng 2022;29:4431–53.
[12] Bathe KJ. Finite element method. Wiley; 2007.
[13] Rao SS. The finite element method in engineering. Amsterdam: Elsevier; 2010.
[14] Hughes TJ. The finite element method: linear static and dynamic finite element analysis. North Chelmsford: Courier Corporation; 2003.
[15] Moorthy S, Ghosh S. A model for analysis of arbitrary composite and porous microstructures with Voronoi cell finite elements. Int J Numer Methods Eng 1996;39:2363–98.
[16] Weyer S, et al. Automatic finite element meshing of planar Voronoi tessellations. Eng Fract Mech 2002;69:945–58.
[17] Bathe KJ. On automatic mesh construction and mesh refinement in finite element analysis. Comput Struct 1989;32:911–36.
[18] Johnston BP, Sullivan Jr JM, Kwasnik A. Automatic conversion of triangular finite element meshes to quadrilateral elements. Int J Numer Methods Eng 1991;31:67–84.
[19] Kechriniotis AI, et al. Classical multivariate Hermite coordinate interpolation on n-dimensional grids. J Comput Appl Math 2024;449:115962.
[20] Dell'Accio F, Di Tommaso F, Siar N. On the numerical computation of bivariate Lagrange polynomials. Appl Math Lett 2021;112:106845.
[21] Taylor RL. On completeness of shape functions for finite element analysis. Int J Numer Methods Eng 1972;4:17–22.
[22] Nguyen VP, Anitescu C, Bordas SP, Rabczuk T. Isogeometric analysis: an overview and computer implementation aspects. Math Comput Simul 2015;117:89–116.
[23] Hughes TJR, Cottrell JA, Bazilevs Y. Isogeometric analysis: CAD, finite elements, NURBS, exact geometry and mesh refinement. Comput Methods Appl Mech Eng 2005;194:4135–95.
[24] Piegl L. On NURBS: a survey. IEEE Comput Graph Appl 1991;10:55–71.
[25] Hughes TJ, Akin JE. Techniques for developing special finite element shape functions with particular reference to singularities. Int J Numer Methods Eng 1980;15:733–51.
[26] Dimitri R. Isogeometric treatment of large deformation contact and debonding problems with T-splines: a review. Curved Layer Struct 2015;2:59–90.
[27] Jiang W, Gao X. Review of collocation methods and applications in solving science and engineering problems. Comput Model Eng Sci 2024;140:048313.
[28] Wang F, Zhao Q, Chen Z, Fan CM. Localized Chebyshev collocation method for solving elliptic partial differential equations in arbitrary 2D domains. Appl Math Comput 2021;397:125903.
[29] Shu C, Richards BE. Application of generalized differential quadrature to solve two-dimensional incompressible Navier-Stokes equations. Int J Numer Methods Fluids 1992;15:791–8.
[30] Shu C. Differential quadrature and its application in engineering. London: Springer; 2000.
[31] Chen W, Striz AG, Bert CW. A new approach to the differential quadrature method for fourth-order equations. Int J Numer Methods Eng 1997;40:1941–56.
[32] Wang X, Liu F, Wang X, Gan L. New approaches in application of differential quadrature method to fourth-order differential equations. Commun Numer Methods Eng 2005;21:61–71.
[33] Fung TC. Imposition of boundary conditions by modifying the weighting coefficient matrices in the differential quadrature method. Int J Numer Methods Eng 2003;56:405–32.
[34] Du H, Lim MK, Lin R. Application of generalized differential quadrature method to structural problems. Int J Numer Methods Eng 1994;37:1881–96.
[35] Al-Furjan MSH, Fereidouni M, Habibi M, Abd Ali R, Ni J, Safarpour M. Influence of in-plane loading on the vibrations of the fully symmetric mechanical systems via dynamic simulation and generalized differential quadrature framework. Eng Comput 2022:1–23.
[36] Tornabene F, Viscoti M, Dimitri R. Static analysis of doubly-curved shell structures of smart materials and arbitrary shape subjected to general loads employing higher order theories and generalized differential quadrature method. Comput Model Eng Sci 2022;133(3):719–98.
[37] Tornabene F, Viscoti M, Dimitri R, Reddy JN. Higher order theories for the vibration study of doubly curved anisotropic shells with a variable thickness and isogeometric mapped geometry. Compos Struct 2021;267:113829.
[38] Javani M, Kiani Y, Eslami MR. Application of generalized differential quadrature element method to free vibration of FG-GPLRC T-shaped plates. Eng Struct 2021;242:112510.
[39] Li H, et al. Vibration analysis of the porous metal cylindrical curved panel by using the differential quadrature method. Thin-Walled Struct 2023;186:110694.
[40] Chinthala VK, et al. A novel strong-form random differential quadrature method to compute the stress intensity factor in fracture mechanics. Theor Appl Fract Mech 2022;121:103416.
[41] Chen Z, Liu D, Liao M. Computations of J-integral and T*-integral in elastic–plastic fracture by the quadrature element method. Theor Appl Fract Mech 2024;130:104252.
[42] Zghal S, et al. Time-dependent deflection responses of FG porous structures subjected to different external pulse loads. J Vib Eng Technol 2024;12:857–76.
[43] Tornabene F, Dimitri R, Viola E. Transient dynamic response of generally-shaped arches based on a GDQ-time-stepping method. Int J Mech Sci 2016;114:277–314.
[44] Tornabene F, Dimitri R. A numerical study of the seismic response of arched and vaulted structures made of isotropic or composite materials. Eng Struct 2018;159:332–66.
[45] Moradi Z, Ebrahimi F, Davoudi M. Coupled Newmark beta technique and GDQ method for energy harvesting and vibration control of the piezoelectric MEMS/NEMS subjected to a blast load. Eng Anal Bound Elem 2022;144:492–506.
[46] Hong CC. Computational approach of piezoelectric shells by the GDQ method. Compos Struct 2010;92:811–6.
[47] Hong CC, Jane KC. Shear deformation in thermal vibration analysis of laminated plates by the GDQ method. Int J Mech Sci 2003;45:21–36.

[48] Shu C, Wang L, Chew YT. Comparative studies of three approaches for GDQ computation of incompressible Navier–Stokes equations in primitive variable form. Int J Comut Fluid Dyn 2004;18:401–12.

[49] Wang T, Cao S, Ge Y. Generation of inflow turbulence using the local differential quadrature method. J Wind Eng Ind Aerodyn 2013;122:96–104.

[50] Xiao Y, et al. Radial basis function-differential quadrature-based physics-informed neural network for steady incompressible flows. Phys Fluids 2023;35:073607.

[51] Tornabene F. Generalized Differential and Integral Quadrature. Bologna: Esculapio; 2023.

[52] Sharma P. Numerical study of grid distribution effect on accuracy of GDQ method of FGPM actuator. Mater Today: Proc 2021;45:5706–8.

[53] Shu C, Chew YT, Richards BE. Generalized differential and integral quadrature and their application to solve boundary layer equations. Int J Numer Methods Fluids 1995;21:723–33.

[54] Shu C, et al. Solutions of three-dimensional boundary layer equations by global methods of generalized differential-integral quadrature. Int J Numer Methods Heat Fluid Flow 1996;6:61–75.

[55] Love AEH. A treatise on the mathematical theory of elasticity. Cambridge: Cambridge University Press; 2013.

[56] Mindlin R. Influence of rotatory inertia and shear on flexural motions of isotropic, elastic plates. J Appl Mech 1951;18:31–8.

[57] Reddy JN, Liu C. A higher-order shear deformation theory of laminated elastic shells. Int J Eng Sci 1985;23:319–30.

[58] Kreja I, Sabik A. Equivalent single-layer models in deformation analysis of laminated multilayered plates. Acta Mech 2019;230:2827–51.

[59] Reddy JN. An evaluation of equivalent-single-layer and layerwise theories of composite laminates. Compos Struct 1993;25:21–35.

[60] Hu H, et al. Review and assessment of various theories for modeling sandwich composites. Compos Struct 2008;84:282–92.

[61] Do Carmo MP. Differential geometry of curves and surfaces: revised and updated second edition. New York: Courier Dover Publications; 2016.

[62] Reddy JN. An evaluation of equivalent-single-layer and layerwise theories of composite laminates. Compos Struct 1993;25:21–35.

[63] Liew KM, Pan ZZ, Zhang LW. An overview of layerwise theories for composite laminates and structures: development, numerical implementation and application. Compos Struct 2019;216:240–59.

[64] Tornabene F. General higher-order layer-wise theory for free vibrations of doubly-curved laminated composite shells and panels. Mech Adv Mater Struct 2016;23:1046–67.

[65] Robbins Jr DH, Reddy JN. Modelling of thick composites using a layerwise laminate theory. Int J Numer Methods Eng 1993;36:655–77.

[66] Tornabene F, Fantuzzi N, Bacciocchi M, Reddy JN. An equivalent layer-wise approach for the free vibration analysis of thick and thin laminated and sandwich shells. Appl Sci 2016;7:17.

[67] Tornabene F, Viscoti M, Dimitri R. Equivalent layer-wise theory for the hygro-thermo-magneto-electro-elastic analysis of laminated curved shells. Thin-Walled Struct 2024;198:111751.

[68] Tornabene F, Viscoti M, Dimitri R. Thermo-mechanical analysis of laminated doubly-curved shells: higher order equivalent layer-wise formulation. Compos Struct 2024;335:117995.

[69] Tornabene F. Hygro-thermo-magneto-electro-elastic theory of anisotropic doubly-curved shells. Bologna: Esculapio; 2023.

[70] Mantari JL, Oktem AS, Soares CG. A new trigonometric shear deformation theory for isotropic, laminated composite and sandwich plates. Int J Solids Struct 2012;49:43–53.

[71] Laureano RW, Mantari JL. Non-polynomial zig-zag unified shear deformation formulation solved via boundary discontinuous method for laminated sandwich plates. Mech Adv Mater Struct 2024;32:1610–27.

[72] Neves AMA, et al. A quasi-3D hyperbolic shear deformation theory for the static and free vibration analysis of functionally graded plates. Compos Struct 2012;94:1814–25.

[73] Toledano A, Murakami H. A high-order laminated plate theory with improved in-plane responses. Int J Solids Struct 1987;23:111–31.

[74] Murakami H. Laminated composite plate theory with improved in-plane responses. J Appl Mech 1986;53:661–6.

[75] Tessler A, Di Sciuva M, Gherlone M. A refined zigzag beam theory for composite and sandwich beams. J Compos Mater 2009;43:1051–81.

[76] Iurlaro L, et al. Assessment of the refined zigzag theory for bending, vibration, and buckling of sandwich plates: a comparative study of different theories. Compos Struct 2013;106:777–92.

[77] Iurlaro L, et al. Refined Zigzag Theory for laminated composite and sandwich plates derived from Reissner's Mixed Variational Theorem. Compos Struct 2015;133:809–17.

[78] Tornabene F, Viscoti M, Dimitri R. Generalized higher order layerwise theory for the dynamic study of anisotropic doubly-curved shells with a mapped geometry. Eng Anal Bound Elem 2022;134:147–83.

[79] Tornabene F. Free vibration analysis of functionally graded conical, cylindrical shell and annular plate structures with a four-parameter power-law distribution. Comput Methods Appl Mech Eng 2009;198:2911–35.

[80] Washizu K. Variational methods in elasticity and plasticity. Oxford: Pergamon Press; 1975.

[81] Reddy JN. A generalization of two-dimensional theories of laminated composite plates. Commun Appl Numer Methods 1987;3:173–80.

[82] Reddy JN, Wang CM, Lee KH. Relationships between bending solutions of classical and shear deformation beam theories. Int J Solids Struct 1997;34:3373–84.

[83] Reddy JN, Wang CM. An overview of the relationships between solutions of the classical and shear deformation plate theories. Compos Sci Technol 2000;60:2327–35.

[84] Phan ND, Reddy JN. Analysis of laminated composite plates using a higher-order shear deformation theory. Int J Numer Methods Eng 1985;21:2201–19.

[85] Tornabene F, Viscoti M, Dimitri R, Rabczuk T. Thermo-magneto-mechanical analysis of curved laminated structures with arbitrary variation of the material properties and novel recovery procedure. Eng Anal Bound Elem 2025;176:106232.

[86] Tornabene F, Viscoti M, Dimitri R. Effect of thermal and electric coupling on the multifield response of laminated shell structures employing higher-order theories. Compos Struct 2025;354:118801.

[87] Tornabene F, Viscoti M, Dimitri R. Magneto-electro-elastic analysis of doubly-curved shells: higher-order equivalent layer-wise formulation. Comput Model Eng Sci 2025;142:1767.

[88] Mahinzare M, Rastgoo A, Ebrahimi F. On nonlinear vibration of piezo-electrically multiscale hybrid nanocomposite sandwich plate including an auxetic core based on HSDT. Int J Struct Stab Dyn 2024;24:2450069.

[89] Dat ND, Quan TQ, Duc ND. Vibration analysis of auxetic laminated plate with magneto-electro-elastic face sheets subjected to blast loading. Compos Struct 2022;280:114925.

[90] Brischetto S, Cesare D. Three-dimensional vibration analysis of multilayered composite and functionally graded piezoelectric plates and shells. Compos Struct 2024;346:118413.

[91] Tran TT, Le PB. Nonlocal dynamic response analysis of functionally graded porous L-shape nanoplates resting on elastic foundation using finite element formulation. Eng Comput 2023;39:809–25.

[92] Javani M, Kiani Y, Eslami MR. Free vibration analysis of FG-GPLRC L-shaped plates implementing GDQE approach. Thin-Walled Struct 2021;162:107600.

[93] Shi CZ, Zheng H, Wen PH, Hon YC. The local radial basis function collocation method for elastic wave propagation analysis in 2D composite plate. Eng Anal Bound Elem 2023;150:571–82.

[94] Ramezani M, Rezaiee-Pajand M, Tornabene F. Linear and nonlinear mechanical responses of FG-GPLRC plates using a novel strain-based formulation of modified FSDT theory. Int J Non Linear Mech 2022;140:103923.

[95] Viola E, Dilena M, Tornabene F. Analytical and numerical results for vibration analysis of multi-stepped and multi-damaged circular arches. J Sound Vib 2007;299:143–63.

[96] Kubair DV, Bhanu-Chandar B. Stress concentration factor due to a circular hole in functionally graded panels under uniaxial tension. Int J Mech Sci 2008;50:732–42.

[97] Tornabene F, Fantuzzi N, Bacciocchi M. A new doubly-curved shell element for the free vibrations of arbitrarily shaped laminated structures based on weak formulation IsoGeometric analysis. Compos Struct 2017;171:429–61.

[98] Wang FF, Dai HH, Giorgio I. A numerical comparison of the uniformly valid asymptotic plate equations with a 3D model: clamped rectangular incompressible elastic plates. Math Mech Solids 2022;27:1370–96.

[99] Zhu C, Fang X, Liu J. A new approach for smart control of size-dependent nonlinear free vibration of viscoelastic orthotropic piezoelectric doubly-curved nanoshells. Appl Math Model 2020;77:137–68.

[100] Zhu C, Fang X, Nie G. Nonlinear free and forced vibration of porous piezoelectric doubly-curved shells based on NUEF model. Thin-Walled Struct 2021;163:107678.